EXPERIMENTAL AND NUMERICAL INVESTIGATION OF A COUNTER-ROTATING BOUNDARY LAYER INGESTING PROPULSION SYSTEM

A THESIS SUBMITTED TO
THE GRADUATE SCHOOL OF NATURAL AND APPLIED SCIENCES
OF
MIDDLE EAST TECHNICAL UNIVERSITY

BY

IBRAHIM SONER BILYAZ

IN PARTIAL FULFILLMENT OF THE REQUIREMENTS
FOR
THE DEGREE OF MASTER OF SCIENCE
IN
AEROSPACE ENGINEERING

JANUARY 2023

Approval of the thesis:

EXPERIMENTAL AND NUMERICAL INVESTIGATION OF A COUNTER-ROTATING BOUNDARY LAYER INGESTING PROPULSION SYSTEM

submitted by **IBRAHIM SONER BILYAZ** in partial fulfillment of the requirements for the degree of **Master of Science in Aerospace Engineering Department, Middle East Technical University** by,

Prof. Dr. Halil Kalıpçılar
Dean, Graduate School of **Natural and Applied Sciences** _____

Prof. Dr. Serkan Özgen
Head of Department, **Aerospace Engineering** _____

Assist. Prof. Dr. Özge Başkan Perçin
Supervisor, **Aerospace Engineering, METU** _____

Examining Committee Members:

Prof. Dr. Serkan Özgen
Aerospace Engineering, METU _____

Assist. Prof. Dr. Özge Başkan Perçin
Aerospace Engineering, METU _____

Prof. Dr. Oğuz Uzol
Aerospace Engineering, METU _____

Prof. Dr. Mehmet Metin Yavuz
Mechanical Engineering, METU _____

Assist. Prof. Dr. Human Amiri
Aeronautical Engineering, Sivas Science and Tech. University _____

Date:23.01.2023

I hereby declare that all information in this document has been obtained and presented in accordance with academic rules and ethical conduct. I also declare that, as required by these rules and conduct, I have fully cited and referenced all material and results that are not original to this work.

Name, Surname: Ibrahim Soner Bilyaz

Signature :

ABSTRACT

EXPERIMENTAL AND NUMERICAL INVESTIGATION OF A COUNTER-ROTATING BOUNDARY LAYER INGESTING PROPULSION SYSTEM

Bilyaz, Ibrahim Soner
M.S., Department of Aerospace Engineering
Supervisor: Assist. Prof. Dr. Özge Başkan Perçin

January 2023, 102 pages

This study investigates the performance of a boundary layer ingesting (BLI) propulsion system with a counter-rotating propulsor numerically and experimentally. The main benefit driver for a BLI propulsion system is that the propulsor ingests the boundary layer of the aircraft's fuselage, which is slower than the free stream velocity and consumes less power to generate the required thrust. The power-saving coefficient (PSC), the amount of power saved to obtain the same net streamwise force compared to the traditional podded configurations, is used to quantify the amount of power saved in this configuration. For the calculation of the PSC, two different configurations are considered: isolated propulsor-isolated fuselage configuration (i.e., non-BLI configuration) and combined propulsor-fuselage configuration (i.e., BLI configuration). The relationship between the power input and the net streamwise force is obtained for each configuration, and the PSC values are calculated. A numerical analysis is performed to assess the benefit of using a counter-rotating propulsor over a single-fan propulsor in the BLI environment. The results show that 3% power saving is obtained for the cruise condition (i.e., zero net streamwise force) in the counter-rotating concept compared to the single

propulsor case, in addition to the 16% power saving obtained for the counter-rotating BLI concept compared to the non-BLI counter-rotating configuration. It is found that the main benefit driver for the counter-rotating concept stems from the recovery of the swirl. The variation of the axial distance between the propulsors in the counter-rotating concept is also investigated, and no relation is found between the axial distance and the PSC values. An experimental setup is designed and produced to analyze the performance of the counter-rotating BLI concept. PSC values are calculated by considering the electrical power input of the fan and the load cell data. The results reveal that approximately 15% of the power is saved in the BLI configuration for the cruise condition.

Keywords: boundary layer ingestion, counter-rotating, propulsion, aerodynamics

ÖZ

ZIT YÖNLÜ DÖNEN VE SINIR TABAKA EMİŞLİ İTKİ SİSTEMİNİN DENEYSEL OLARAK VE HESAPLAMALI AKIŞKANLAR DİNAMİĞİ İLE İNCELENMESİ

Bilyaz, Ibrahim Soner
Yüksek Lisans, Havacılık ve Uzay Mühendisliği Bölümü
Tez Yöneticisi: Dr. Öğr. Üyesi. Özge Başkan Perçin

Ocak 2023 , 102 sayfa

Bu çalışmada, sınır tabaka emişli (STE) itki sistemi konfigürasyonu, hem deneysel olarak, hem de sayısal yöntemlerle incelenmiştir. Genel olarak sınır tabaka emişli itki sistemlerinin verimi, düşük hızdaki akışa sahip olan uçak gövdesi sınır tabaka profilinin motor tarafından emilmesinden kaynaklanır. Bu düşük hızdaki akışı emen motor, aynı itkiyi üretmek için daha az bir enerji sarfeder. Genel olarak da bu verimlilik yüzdesi, güç tasarrufu katsayısı (GTK) parametresi ile hesaplanmaktadır. Bu katsayı, uçak motorunun herhangi bir uçuş koşulunda iken aynı net eksenel kuvvette yüzdesel olarak geleneksel konfigürasyonlara göre ne kadar daha az enerji tükettiği belirlenerek hesaplanır. Bunun için ise, hem sınır tabaka emişli, hem de geleneksel konfigürasyonu temsil eden iki farklı konfigürasyon karşılaştırılmıştır. Verimi hesaplamak için, normal bir veter etrafında döndürülerek elde edilmiş ve uçak gövdesini temsil eden bir yapı arkasına itki sistemi yerleştirilerek güç değerleri incelenmiş ve güç tasarrufu katsayısı değerleri hesaplanmıştır. Bunun için ilk olarak zıt yönlü dönen itki sistemi içeren STE konfigürasyon, yine aynı itki sistemini içeren fakat STE olmayan konfigürasyon ile

karşılaştırılmış, ve net kuvvetin sıfır olduğu durumda STE sistemde yaklaşık 16% güç tasarrufu elde edilmiştir. Ek olarak,tek pervane ile zıt yönlü dönen pervane içeren iki konsept STE konfigürasyonda karşılaştırılmıştır. Sonuçlara göre zıt yönlü dönen pervane konfigürasyonu, tek olana göre net kuvvetin sıfır olduğu durumda 3% daha az güç harcadığı görülmüştür. Bunun da nedeninin pervane arkasında oluşan girdapların sönümlenmesi olduğu sonucuna varılmıştır. Ayrıca, aralıklı olarak pervaneler arasındaki mesafe kademeli olarak artırılmış, fakat tek pervaneli sisteme göre hemen hemen aynı miktarda güçten tasarruf edildiği görülmüştür. Dolayısıyla, pervaneler arasındaki mesafe ile GTK değeri arasında bir ilişki bulunamamıştır. Daha sonra, veter etrafında döndürülerek elde edilen bir gövde benzer bir gövde, yazar tarafından tasarlanarak üretimi yapılmıştır, ve STE konfigürasyon deneysel olarak incelenmiştir. Deneyde sadece yük hücresiyle kuvvet ölçümü ve fana verilen elektrik gücü ölçümleri yapılmıştır, ve net eksenel kuvvetin sıfır olduğu durumda STE olan konfigürasyonda yaklaşık 15% güç tasarrufu elde edildiği görülmüştür.

Anahtar Kelimeler: sınır tabaka emilimi, zıt yönlü dönen, itki, aerodinamik

To my family

ACKNOWLEDGMENTS

During the hard times to prepare my thesis, I would like to thank my family for providing continuous emotional support. Importantly, I want to thank my supervisor Dr. Özge Başkan Perçin for guiding and helping me. I also want to thank Dr. Mustafa Perçin for his support during the experiments. I would also like to thank Umut Altuntaş, who is an unofficially responsible person for the 3D printer in RÜZGEM, to manufacture and print my setup. Also, I want to thank Hüseyin Özdemir and Batuhan Doğan, who are the staff in the RÜZGEM aero lab, for constructing and building my experimental setup.

And also, I would like to thank my brother Serhat for his helpful pieces of advice about the thesis writing process.

In addition, I want to thank Umut Can Küçük for the small discussions and exchange of some useful ideas.

TABLE OF CONTENTS

ABSTRACT v

ÖZ vii

ACKNOWLEDGMENTS x

TABLE OF CONTENTS xi

LIST OF TABLES xiv

LIST OF FIGURES xv

LIST OF ABBREVIATIONS xxi

CHAPTERS

1 INTRODUCTION 1

1.1 Boundary Layer Ingested Propulsion Systems 1

1.2 Motivation 5

1.3 Objective 5

1.4 Literature review 6

1.4.1 BLI Propulsion Studies Between 1947-2009 6

1.4.2 BLI Propulsion Studies from 2009 to the Current Time Being 8

2 THEORY 13

2.1 Power Balance Method 13

2.2 Power Balance Equation 14

2.3 Power Balance Method Applied to a BLI Propulsor 18
2.3.1 Classical Propulsive Efficiency Calculation 18
2.3.2 Alternative Method for the BLI Benefit Calculation 21
3 NUMERICAL INVESTIGATION OF BLI 23
3.1 Validation of the Numerical Setup 23
3.1.1 CFD Mesh and Flow Domain for the Validation Setup 24
3.1.2 Boundary Conditions 28
3.2 Application of the Counter-Rotating Propulsor Concept 29
3.3 Results 33
3.3.1 Validation Setup CFD Results 33
3.3.2 The Counter-Rotating Propulsor Application CFD Results . . 39
4 EXPERIMENTAL INVESTIGATION OF BLI 49
4.1 Overview of the Experimental Setup 49
4.2 Experimantal and Wind Tunnel Facilities 50
4.3 Production of the Experimental Setup 51
4.3.1 Fuselage Body 52
4.3.2 Fan and Casing 58
4.3.3 Additional Structural Parts 61
4.3.3.1 Load Cell Plate 61
4.3.3.2 Airfoil Struts 61
4.4 Results 63
4.4.1 Isolated Body Configuration 64
4.4.2 Isolated Propulsor Configuration 71

4.4.3 BLI Configuration 77

5 CONCLUSION AND FUTURE WORKS 83

5.1 Conclusion 83

5.2 Future Works 84

APPENDICES

A DEFINITIONS FOR THE OTHER POWER COMPONENTS OF THE POWER BALANCE EQUATION 87

A.1 Illustrative Examples 90

A.1.1 Isolated Body 90

A.1.2 Free Stream Propulsor 93

REFERENCES 97

LIST OF TABLES

TABLES

Table 3.1 Properties of the generated mesh 28

Table 3.2 3D Fan Zone properties for the BLI configuration at different net streamwise forces 31

Table 3.3 3D Fan Zone properties for the isolated counter-rotating propulsor configuration at different net streamwise forces 32

Table 3.4 Drag force of the isolated body with different turbulence models in CFD 35

Table 3.5 3D Fan Zone properties for the single propulsor concept at different net streamwise forces 43

Table 4.1 Final dimension of the fuselage 55

LIST OF FIGURES

FIGURES

Figure 1.1 BLI benefit mechanism for a flying aircraft [1] 2

Figure 1.2 Douglas XB-42 Mixmaster aircraft [2] 3

Figure 1.3 CENTRELINE[3] (left) and STARC-ABL [4] (right) projects configurations 4

Figure 1.4 D8 Double Bubble passenger aircraft [5] 4

Figure 1.5 Stern-mounted propeller and airship model [6] 7

Figure 2.1 The problem with the thrust-drag bookkeeping for highly integrated systems [7] 14

Figure 2.2 Control volume around an aircraft for the power balance analysis [8] 15

Figure 2.3 Control volume around a BLI propulsor [7] 18

Figure 3.1 Experimental setup [9] 24

Figure 3.2 Side view of the fuselage and propeller cross section in the CFD domain 25

Figure 3.3 CFD domain 25

Figure 3.4 Overall look for the CFD mesh 26

Figure 3.5 High density of mesh around the body and propeller 26

Figure 3.6 Boundary layer mesh around the body 27

Figure 3.7 Velocity profiles for the mesh independence study 27

Figure 3.8 Boundary conditions for the numerical setup 28

Figure 3.9 Counter-rotating propulsor configuration with the modified axisymmetric body 30

Figure 3.10 Velocity contours for the counter-rotating propulsors concept in BLI configuration 30

Figure 3.11 Upstream and downstream lines shown in yellow at which the velocity profiles are taken 33

Figure 3.12 Velocity profiles at 100 mm upstream (left) and 100 mm downstream (right) from the nose of the propeller hub 34

Figure 3.13 The residuals for the k-ω SST solution 34

Figure 3.14 Pressure coefficient contours obtained by CFD (left) and experiment (right) [9] 35

Figure 3.15 Boundaries of the control volume around the propulsor 36

Figure 3.16 Radial locations at which the data are taken 38

Figure 3.17 Angular variation of axial velocity (left) and total pressure (right) 38

Figure 3.18 Velocity contours around the body wake 39

Figure 3.19 Control volume boundaries for the counter-rotating concept . 40

Figure 3.20 Mechanical flow power coefficient vs net streamwise force coefficient plot for both configurations (Adapted from [10]) 40

Figure 3.21 Net wake power outflow and propulsor mechanical flow power input changes with respect to the net streamwise force 42

Figure 3.22 Single propulsor concept applied for the same fuselage geometry and setup 43

Figure 3.23 Mechanical flow power coefficient vs net streamwise force coefficient plot for counter-rotating propulsors and single propulsor concepts with the swirling motion 44

Figure 3.24 Mechanical flow power coefficient vs net streamwise force coefficient plot for counter-rotating propulsors and single propulsor concepts **without** the swirling motion 45

Figure 3.25 Axial distance between two propulsors vs power saving coefficient for the cruise condition relative to the single propulsor 46

Figure 4.1 Isolated fuselage (left) and free stream propulsor (right) configurations used in the experiment 49

Figure 4.2 BLI configuration used in the experiment 50

Figure 4.3 METU RUZGEM C3 wind tunnel which is used in the experiment 52

Figure 4.4 Design diagram for determining the fuselage body dimensions 53

Figure 4.5 Overall look for the 2D CFD setup of the isolated body configuration 53

Figure 4.6 2D mesh around the isolated body 54

Figure 4.7 The line on which the boundary layer data are taken 54

Figure 4.8 Boundary layer velocity profile around the fuselage body . . . 55

Figure 4.9 Designed fuselage in a CAD environment 56

Figure 4.10 Fuselage body in a disassembled form 57

Figure 4.11 Female (left) and male (right) interfaces of the fuselage body 57

Figure 4.12 Connection of the fuselage body to the threaded rod by the contra operation 58

Figure 4.13 San Ace 172 counter-rotating fan and its fan curve [11] 59

Figure 4.14 Designed metal holder in a CAD environment 59

Figure 4.15 Attached metal holder and the fan in front (left) and side (right) view 60

Figure 4.16 Casing in a CAD environment 60

Figure 4.17 Casing in a disassembled form (left) and the casing with add-on pieces (right) 61

Figure 4.18 Manufactured load cell plate 62

Figure 4.19 Airfoil struts 63

Figure 4.20 Aft strut as one piece (left), and parts separated (right) 63

Figure 4.21 Axis definitions of the load cell in the experiment 64

Figure 4.22 The isolated body configuration in the experiment 65

Figure 4.23 The isolated body configuration in experiment without the airfoil struts 66

Figure 4.24 Laser alignment of the load cell plate with respect to the wind tunnel center 67

Figure 4.25 The x-component (top) and z-component (bottom) of the net force vs the Reynolds number for the isolated body configuration . . . 68

Figure 4.26 The y-component (drag) of the net force vs the Reynolds number for the isolated body configuration 69

Figure 4.27 The drag coefficient vs the Reynolds number for the isolated body configuration 70

Figure 4.28 CFD domain for the isolated body configuration in the wind tunnel 71

Figure 4.29 The mesh around the body in the wind tunnel model 71

Figure 4.30 The static pressure contours and the low-pressure regions around the strut on the isolated body in CFD 72

Figure 4.31 2D and 3D CFD results of the boundary layer profiles of the isolated body configuration around the fan inlet location 73

Figure 4.32 The overall look of the isolated propulsor configuration 74

Figure 4.33 The front view of the isolated propulsor configuration 75

Figure 4.34 The x-component (top) and z-component (bottom) of the net force vs the electrical power input for the isolated propulsor configuration 76

Figure 4.35 The y-component of the net force vs the electrical power input for the isolated propulsor configuration 77

Figure 4.36 The overall look of the BLI configuration 78

Figure 4.37 The front view of the BLI configuration 79

Figure 4.38 The x-component (top) and z-component (bottom) of the net force vs the electrical power input for the BLI configuration 80

Figure 4.39 The y-component of the net force vs the electrical power input for the BLI configuration 81

Figure 4.40 C_{PE} vs C_{FN} plots for the BLI and non-BLI configurations in the experiment 82

Figure A.1 Control volume around an aircraft for the power balance analysis [8] 87

Figure A.2 Power dissipation components inside the control volume for a BLI configuration [12] 88

Figure A.3 Surface and wake dissipation components for an isolated body [12] 89

Figure A.4 Control volume around an isolated body [7] 90

Figure A.5 Change of the power components inside the flow field for an isolated body [7] 92

Figure A.6 Control volume around an isolated propulsor [7] 93

Figure A.7 Change of power components inside the flow field the downstream of an isolated propulsor [7] 95

LIST OF ABBREVIATIONS

BLI	Boundary Layer Ingestion
WI	Wake Ingesiton
CFD	Computational Fluid Dynamics
PSC	Power Saving Coefficient
TP	Transverse Plane
SP	Survey Plane
TE	Trailing Edge
KE	Kinetic Energy Deposition Rate
e	Exit
CV	Control Volume
CENTRELINE	Concept Validation Study for Fuselage Wake-Filling Propulsion Integration
STARC-ABL	Single-aisle Turboelectric Aircraft with Aft Boundary-Layer Propulsion

LIST OF SYMBOLS

$\bar{\bar{\tau}}$	Shear Stress Tensor
$\dot{E}_a$	Axial Kinetic Energy Deposition Rate
$\dot{E}_p$	Pressure Work Outflow Rate
$\dot{E}_v$	Transverse Kinetic Energy Deposition Rate
$\dot{E}_{wave}$	Wave Energy Outflow Rate
$\dot{E}_w$	Wake Energy Deposition Rate
η_P	Propulsive Efficiency
Φ	Power Dissipation
ρ	Density
C_{FN}	Net Streamwise Force Coefficient
C_{PE}	Electrical Power Coefficient
C_{PK}	Mechanical Flow Power Coefficient
D	Drag
D_i	Induced Drag
F_N	Net Axial Force
P	Power
p	Pressure
P_E	Electrical Power
P_K	Mechanical Flow Power
P_S	Net Propulsor Shaft Power

P_V	Pressure-Volume Power
q_∞	Free Stream Dynamic Pressure
Re	Reynolds Number
S	Area
T	Thrust
u	Perturbation Velocity in x-direction
V	Velocity
v	Perturbation Velocity in y-direction
V_∞	Free Stream Velocity
V_{TP}	Velocity at Transverse Plane
w	Perturbation Velocity in z-direction

CHAPTER 1

INTRODUCTION

In this chapter, the boundary layer ingestion concept is introduced, and the relevant studies in the literature are presented. The studies are categorized into two groups based on the era that they were performed: the studies performed before 2009 and from 2009 to the current time.

1.1 Boundary Layer Ingested Propulsion Systems

In today's world, energy-efficient systems with less fuel consumption have become more and more important. The increase in fuel prices and the effect of carbon emissions on climate change increase the need for more energy-efficient systems. The aviation industry especially leads these carbon emissions and has an important contribution overall. There are some research fields in aviation for developing zero-emission sustainable fuel systems. It is still an active research area but requires more and more validation cases to become an applicable method. But for now, reducing the current fuel consumption in aviation is of first priority to reduce the emissions and make the systems more energy efficient, even for the zero carbon emission fuels. So, some novel concepts in aviation are being investigated to increase efficiency. Boundary layer ingested (BLI) propulsion systems are among these novel concepts.

In BLI propulsion systems, the benefit results from ingesting the airframe boundary layer by the aircraft propulsion system. With the ingestion of the aircraft boundary layer by the propulsor, lower magnitudes of the flow velocity are going through the engine because of the lower velocity of the boundary layer. By the energy conserva-

tion principle, propelling the lower velocity of air by the engine requires less power, and the same thrust can be generated with a lower amount of fuel (or power) consumption. And because the incoming air velocity to the propulsor is smaller, the outflow jet air which exits the propulsor has a smaller velocity magnitude, which prevents the amount of wasting kinetic energy [13]. This smaller outflow velocity also reduces the dissipations inside the jet exit and increases propulsive efficiency [8].

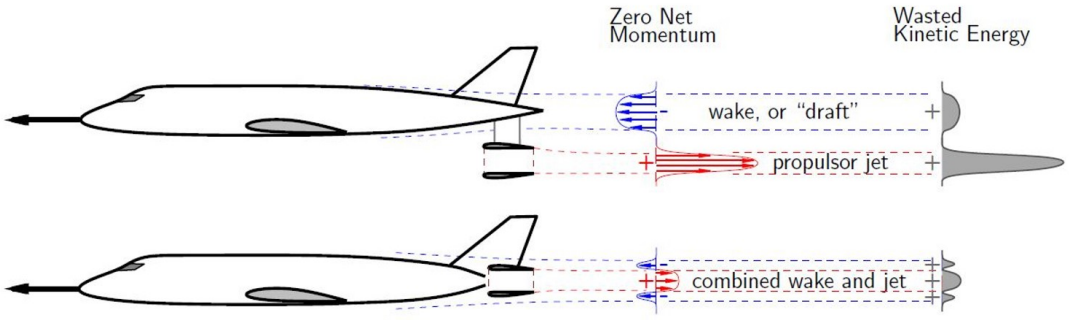

Figure 1.1: BLI benefit mechanism for a flying aircraft [1]

Boundary layer ingested (BLI) propulsion, which was first applied for marine propulsion, is not a new concept. In the early 1900s, only marine propulsion research was focused on this configuration; but after the second world war, rapid enhancements in the aviation industry made it possible to apply this concept to aircraft. Later, the performance of this concept for the airships was also investigated [14].

Towards the end of the second world war, Douglas XB-42 Mixmaster aircraft [2] appeared to be one of the first novel aircraft utilizing the BLI propulsion concept. This aircraft has a pusher propulsor configuration and two counter-rotating propellers behind the airframe. The aircraft showed a significant increase in aerodynamic performance, both by reducing the jet dissipation and eliminating the swirling motion behind the propellers through the presence of counter-rotating propeller pairs. In 1945, it flew from Long Beach, California to Washington in a time of 5 hours and 17 minutes and broke the speed record of 433.6 km/hour. However, due to some stability and vibrational problems, and having excessive yawing moments, the production of the aircraft was canceled. Nevertheless, it

showed quite well aerodynamic performance compared to its counterparts in its era.

Figure 1.2: Douglas XB-42 Mixmaster aircraft [2]

There are several ongoing research projects, such as CENTRELINE [15], DisPURSAL [16], STARC-ABL [4], which are focusing on the design of aircraft with BLI propulsion systems. The CENTRELINE project, for example, funded by European Union, aims to produce more energy-efficient aircraft configurations, especially for civil aviation. For further information, the reader can refer to Refs. [17, 18, 3].

Another famous research project which is funded by NASA is STARC-ABL project. The same purpose as in the CENTRELINE project is present, and for further information, the reader can refer to Refs. [19, 20, 21, 22].

Figure 1.3: CENTRELINE[3] (left) and STARC-ABL [4] (right) projects configurations

One other important project conducted by NASA and the Massachusetts Institute of Technology is the D8 Double Bubble Aircraft. It is a 180-passenger capacity civil transport aircraft that uses the BLI approach and is designed to enter the service around 2035 [23]. Compared to Boeing 737-800, it is estimated that the D8 family aircraft supply 60 dB lower engine noise and 70% reductions of fuel consumption [23].

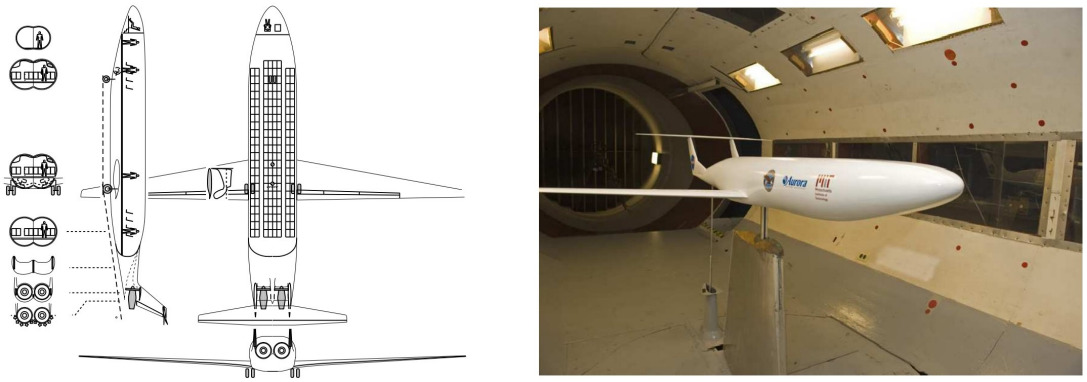

Figure 1.4: D8 Double Bubble passenger aircraft [5]

In BLI configurations, although the power consumption reduction can be high, one drawback of this concept may be the requirement of distortion-tolerant propulsors. Since the airframe boundary layer is ingested by the propulsor, a significant amount of inlet distortion occurs around the inlets of the fans-propellers, and lower total pressure recovery values are obtained at the engine faces. This requires distortion-tolerant fans or propellers. This is also another research topic that requires a solid understanding of turbomachinery and fan mechanisms. Some studies have contributed to this field [24, 25, 17, 26, 27], and many others are

being published these days. If the type of distortion for the engine is radial (which is highly suitable for the BLI applications) rather than circumferential, the limitations can be mitigated by changing the local radial blade angles in fan or propeller blades (because the low-velocity regions change radially rather than circumferentially, and the type of the distortion is steady). Despite these challenges, the benefit is quite high, and the difficulties can be overcome by producing suitable fans or propellers with improving technology.

1.2 Motivation

Since the energy crisis is a big problem in our today's world, the importance of efficient systems is increasing. Because BLI propulsion provides less energy consumption to generate the thrust in aircraft, utilizing the wake energy of the airframe is also an option to reduce the consumed power. In BLI systems, the energy-saving amounts can be as high as 20%, depending on the wake profile of the airframe. So, the main motivation for this study is to obtain more energy-efficient propulsion systems.

1.3 Objective

The objective of this study is to show that if the wake energy of the fuselage can be utilized, more energy-efficient propulsion systems may occur, which may be possible for the next-generation propulsion systems. Also different than conventional propulsors, another aim is to demonstrate that counter-rotating fan or propeller configurations can further increase the propulsive performance and reduce energy consumption by recovering the swirl behind the propulsor. This is also shown in the BLI configuration.

1.4 Literature review

1.4.1 BLI Propulsion Studies Between 1947-2009

Boundary layer ingested (BLI) propulsion, which was first applied for marine propulsion, is not a new concept. In the early 1900s, only marine propulsion research is focused on this configuration; but after the second world war, rapid enhancements in the aviation industry led to apply this concept to aircraft.

The very first investigations are done by Smith et al. [28]. It is stated that ingesting the aircraft's boundary layer by the engines can increase the performance and range of the aircraft, which should be investigated deeply in the future.

After this study, the first trials and experiments are done on an airship model in 1962 by McLemore [6]. In this study, a 1/20 scaled airship model is experimentally tested at NASA Langley Research Center. The stern-mounted and conventional-mounted propeller configurations are tested separately and the propulsive efficiencies of these configurations are compared to each other. In the stern-mounted configuration, the maximum propulsive efficiency can be as high as 122% which was considered unusual and erroneous compared to the conventional-mounted one. For the zero net streamwise force, the stern-mounted propeller showed about 103% propulsive efficiency which is different from the conventional-mounted one whose value is 59%.

After that, a second remarkable research study was performed by L.Smith [13] in 1993. He did an integral momentum analysis for the wake and boundary layer ingestion propulsion and introduced a power saving coefficient (PSC), which was found to be generally more useful than the propulsive efficiency when quantifying the BLI benefit. It is defined as:

$$PSC = \frac{P_{non-BLI} - P_{BLI}}{P_{non-BLI}} \tag{1.1}$$

which P refers to the consumed power for the thrust generation.

As in the case in the McLemore [6] study, classical Froude propulsive efficiency

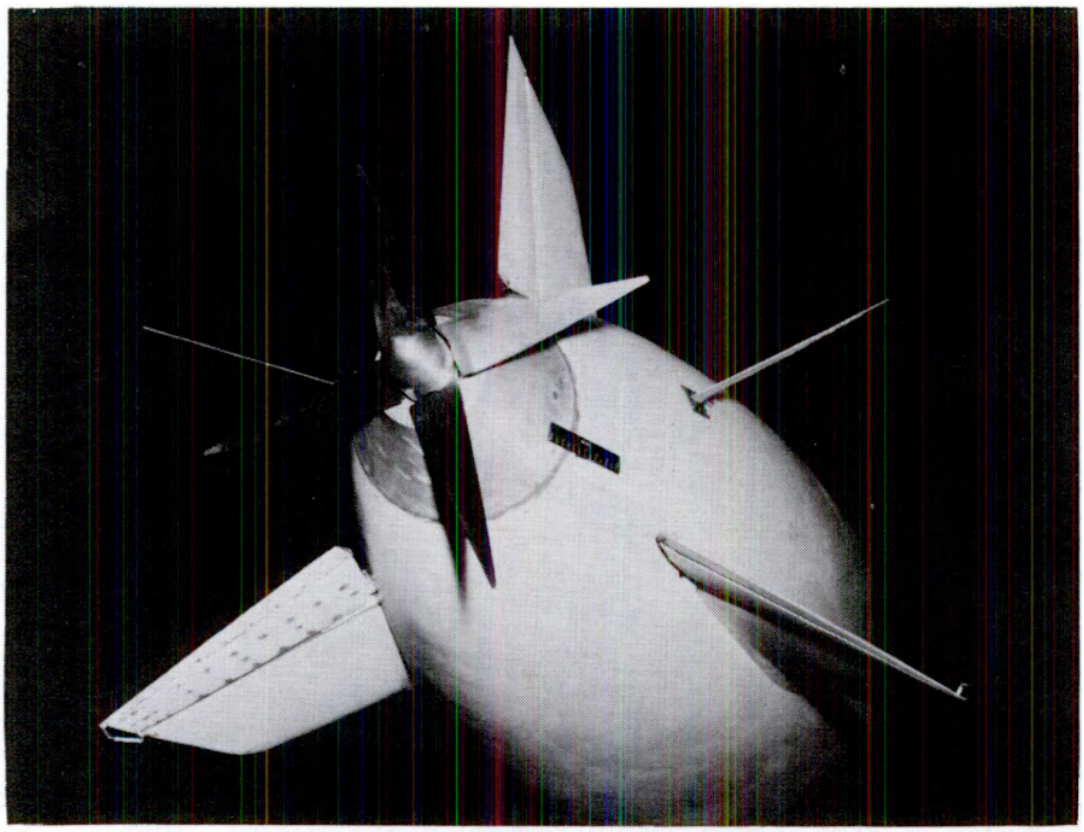

Figure 1.5: Stern-mounted propeller and airship model [6]

tends to become greater than unity, which requires an alternative definition for the quantification of the benefit. Rather than propulsive efficiency, he stated that this quantity may be defined as a coefficient. Smith [13] introduced this definition with his study, and with some numerical studies; he found that the power saving coefficient can be as high as 20% in some cases depending on the amount and of the wake recovery.

After that in 2007, Plas et al. [29] performed one of the very first evaluations for the BLI ingesting ducted propulsors. They found that an intake embedded in the aircraft airframe which generates some amount of distortion at the aerodynamic interface plane (AIP) may decrease the power consumption required for the propulsion by an amount of 3% - 4%. They also stated that although there are some power savings (quantified as a PSC), there are also considerable amounts of risks and challenges for the fan and compressor of the engines due to the higher levels of inlet distortions.

1.4.2 BLI Propulsion Studies from 2009 to the Current Time Being

It is worth mentioning that the BLI propulsion approach and benefit metric are quantified differently after Drela and Kohler [8] published their work in 2009. In their study, they used power conservation equations rather than momentum conservation in a control volume, which is called the power balance method. This method is introduced and explained in the theory part of this work (Chapter 3). With this method, they introduced the power source, sink and outflow terms, and quantified the benefit metric as PSC. After this paper was published, many studies used this power balance method to calculate the PSC of the BLI systems.

One of the early experimental studies using the power balance method was conducted in 2013 by Atinault et al. [30]. In this study, a combined numerical and experimental work was performed to investigate the flow and pressure field around an axisymmetric fuselage that is propelled by a ducted fan without any stator. Since they modeled the ducted fan with an actuator disc by adding a swirl in their numerical setup, they removed the stator vanes in their experiment to make a better comparison. In CFD, the actuator disk model includes radial variations of total pressure and temperature (results in swirling velocity at the propulsor outlet) which is constructed by the Glauert theory. In the experiment, the propulsor is traversed both axially and vertically and PSC is obtained for four different BLI and non-BLI cases. With the vertical traverse of the fan, partial ingestion of the fuselage boundary layer has occurred. They calculated the PSC for the cruise, deceleration, and acceleration conditions. For the cruise condition, approximately 24% PSC is obtained for the closest BLI location (5cm axial distance from the trailing edge of the fuselage) and 20% PSC is obtained for the 20cm axial distance. Less ingested boundary layer gave lower PSC results. With the increasing net axial force (towards acceleration), PSC is decreased, but their results were not detailed so much and required further investigation.

With the study of Sabo and Drela [31] which is made in 2015, a small-scale fuselage and a commercial ducted fan were used to assess the BLI benefit. The axisymmetric fuselage was obtained by the revolution of the NACA 0040 profile, and a small commercial ducted fan was placed behind the body. The relative position of

the fan with respect to the fuselage was altered (both in longitudinal and transverse directions) to find the position at which the electrical power consumption of the fan is minimum, which means PSC is maximum. The experiment was performed both with and without the trip wire, which is placed at the 15% length of the body at the rear. The reason for putting the trip wire was to make the flow turbulent and keep it attached to the surface of the body. At the body wake, the transition to turbulence is determined by noise levels with the help of a stethoscope.

In the study, 2 sets of experiments are done and there were no flow measurements. So, the PSC is calculated based on only electrical power consumption. In the first case, the body both with and without the trip wire was investigated. In the second case, only a body with a trip wire was investigated. The results showed that tripped body has more drag and drag coefficient but has more PSC value. In the first part, the body without the trip wire configuration had 26% PSC, but with the trip wire, this value was measured as 29%. For the second part and measurements, tripped body configuration showed 25% PSC. The author stated that this second part had a higher confidence interval and had more reliable results. One important result of this study is that the higher the ingested boundary layer of the wake, the more power saving benefit from the configuration. The maximum PSC was obtained when the fan was placed at the closest axial distance from the fuselage and ingested the whole boundary layer of the fuselage.

After that in 2017, Lv et al. [9] experimentally quantified the BLI and wake ingestion (WI) propulsion benefit for cruise conditions. They used a commercial small-scale open-type APC 9x10 propeller which was placed aft of the axisymmetric fuselage. This study is also used for the validation of the CFD setup in this thesis in Chapter 3. In the experiment; velocity, torque, total, and static pressure measurements were performed to quantify the resultant forces and power components upstream and downstream of the propulsor. To obtain the static pressure field, they used PIV data with the pressure field reconstruction technique. However, these measurements were done only for WI configuration. In BLI configuration, instead of using any flow measurement technique, they quantified PSC by means of reduced shaft power which was obtained with the torque sensor placed

at the propellers shaft. Also around the propulsor in the WI configuration, power components are measured and quantified with the available data. They found that PSC can be as high as 8% - 10% in the WI configuration and 18% for the BLI configuration.

In another study, the pusher propeller configuration which represents the BLI configuration is compared with the one whose propeller is placed in front of the fuselage [32]. To represent the fuselage, an axisymmetric NACA 0024 profile body of revolution is used. The CFD analyses are performed, and it is found that for the cruise condition (constant velocity), the backward (pusher) propeller cause 28.5% less drag than the forward one. The reason for this is found as flow acceleration and deceleration because of the fuselage chamber and flow separation. Also, the backward one ingests more mass flow and applies less pressure ratio than the forward one. In addition, the backward one consumes less power which has a power saving coefficient of 21.7% compared to the forward one.

Later in 2020, Voogd [33] performed a similar experiment in his masters thesis. He used an axisymmetric fuselage and a commercial ducted fan to investigate the BLI and WI benefit. He used a five-hole probe to obtain whole velocity, total and static pressure fields. He calculated the PSC in two ways: one is based on the mechanical flow power saving in BLI and WI configurations which are obtained by five-hole probe measurements, and the other is based on the electrical power saving of the ducted fan. His results differed from each other, but approximately he calculated 32% PSC based on the electrical power and 47% PSC based on the mechanical flow power. In his study, he pointed out that the misalignment of the five-hole probe might be the reason for the difference in PSC values.

Not so much later, in 2021, Della Corte et al. [18] performed an experimental study around an axisymmetric type fuselage in the scope of the CENTRELINE (Concept Validation Study for Fuselage Wake-filling Propulsion Integration) project. This project is funded by European Union and aims to use an electrical ducted fan-type propulsor aft of the typical passenger aircrafts fuselage, which ingests the boundary layer of the airframe. In this configuration, the main thrust comes from the two underwing turbofan engines, but the remaining portion comes from

the aft fan. The electricity produced by the underwing turbofans derives the BLI fan. In the experiment, this type of ducted fan was produced by the researchers, and an axisymmetric fuselage is used according to the CENTRELINE specifications. The fuselage and propulsor are merged into one piece and the resultant axial force component is measured as a whole with the one force sensor. PIV and pressure field reconstruction methods are applied. The boundary layer characteristics, flow field properties, and power components were shown by PIV and pressure field measurements. PSC was not calculated, but the possible max benefit drivers and flow characteristics were investigated. For example, boundary layer thickness, and power components before and after the BLI propulsor for the case with different net axial forces (acceleration or deceleration) are investigated. The flow field around the fan and fuselage is investigated both axially and radially with PIV measurement planes. In this study, it is found that the boundary layer is thinner before and after the propulsor due to the suction and increased momentum effect. When measurements of the boundary layer and power dissipation components are obtained for varying net axial force; as axial force increases, BLI benefit decreases due to the increased exit kinetic energy flux and jet dissipation. So, they found that the most ideal and beneficial case in terms of power consumption is the one whose exit axial kinetic energy flux is closer to the free stream value (which means zero axial perturbation velocity).

CHAPTER 2

THEORY

In this section, a common method for investigating the BLI benefit, which is called the power balance method, is explained. The origin and the derivations of this method are introduced.

2.1 Power Balance Method

In highly integrated propulsion systems, such as BLI propulsion, the thrust-drag bookkeeping cannot be considered the traditional way. The traditional approach uses the advantage of the separation of the propulsion system and airframe, which simplifies the analysis. In this bookkeeping, momentum equations are used. Since the pressure and wake fields of the airframe and propulsor are not affected by each other, momentum conservation equations are feasible and sufficient. The thrust and drag of the propulsor and airframe are investigated separately by the application of momentum equations; and at the end, the two systems are brought together to form the overall system integration. However, for highly integrated systems, this approach brings some problems since the pressure and wake fields of the airframe and propulsor are highly affected by each other. The thrust generated by the propulsor directly affects the airframe drag, and the wake field of the airframe again directly affects the generated thrust and required energy consumption of the propulsor. So, some ambiguities arise for the analysis.

Due to these difficulties, in 2009, Drela et al. [8] proposed the power balance method. Rather than momentum balance, this method uses the rate of energy (power) balance across the control volume and quantifies power sources & sinks

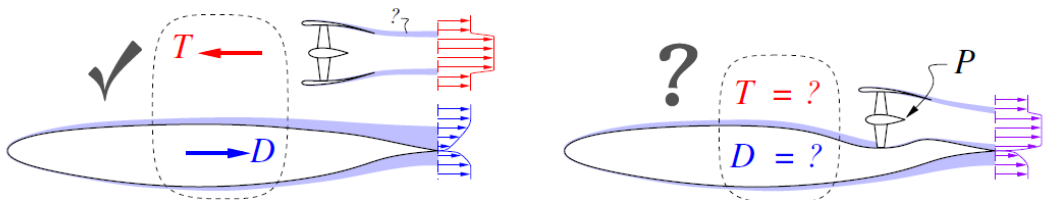

Figure 2.1: The problem with the thrust-drag bookkeeping for highly integrated systems [7]

inside the control volume. This method is more powerful and is used for highly integrated systems because energy deposition rates are independent of the wake or pressure fields, which brings a more solid approach, as Hall et al. [12] explained in their study.

In addition to writing power balance, in some studies, another energy balance method which is exergy balance is used for the BLI analyses [34, 35]. This is another method to quantify the benefit, but since the power balance analysis is performed in this study, it is beyond the scope.

2.2 Power Balance Equation

The power balance equation in fact comes from the Navier-Stokes momentum equation but simply appears in a modified form. Consider the differential Navier-Stokes equation with the absence of body forces [8]:

$$\rho \vec{V} \cdot \nabla \vec{V} = -\nabla p + \nabla \cdot \bar{\bar{\tau}} \tag{2.1}$$

Multiplying this equation with the $\vec{V}$ (velocity) gives the mechanical energy equation in a differential form, which can be written as:

$$\rho \vec{V} \cdot \nabla (\frac{1}{2} V^2) = -\nabla p \cdot \vec{V} + (\nabla \cdot \bar{\bar{\tau}}) \cdot \vec{V} \tag{2.2}$$

Now we need to take the integral of this differential mechanical energy equation.

For this, first, we can define a control volume around the aircraft which is flying at an altitude with zero net streamwise force (constant speed). Consider the following system in Figure 2.2, which is a view of a 3D control volume around an aerodynamic body. The S_B surface covers the moving elements (like the upper propulsor) or just makes an enclosure around some of them (like the bottom propulsor) [8].

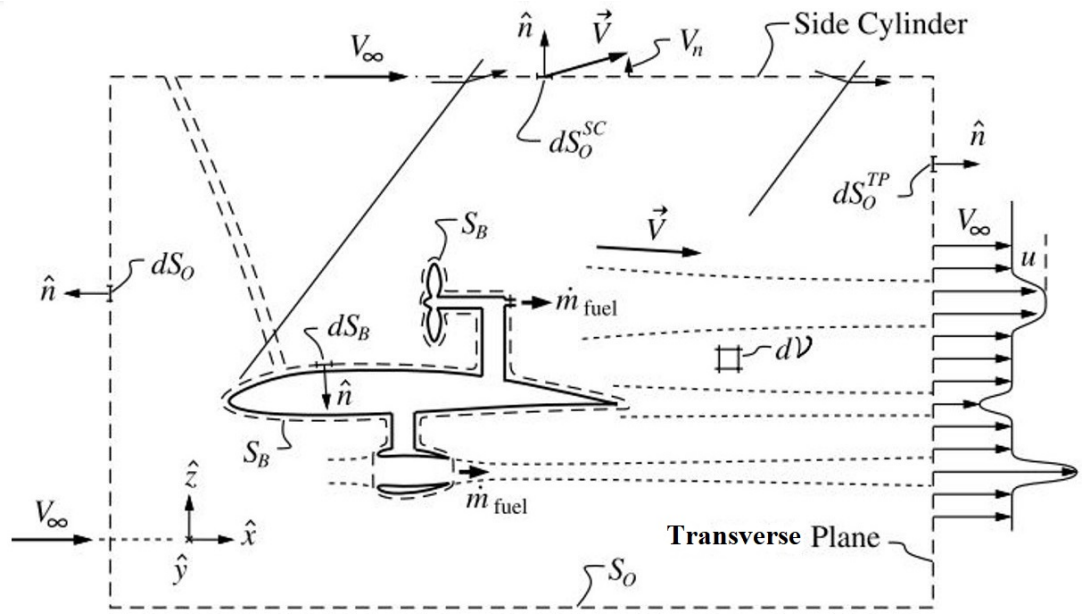

Figure 2.2: Control volume around an aircraft for the power balance analysis [8]

Note that the velocity at the Transverse Plane ($\vec{V}_{TP}$) is:

$$\vec{V}_{TP} = (V_\infty + u) \cdot \hat{i} + v \cdot \hat{j} + w \cdot \hat{k} \tag{2.3}$$

If we take the volume integral of equation 2.3 and perform Gausss divergence theorem, we can obtain the power balance equation for the control volume in a simplified manner in Equation 2.4 [8]:

$$\underbrace{P_S + P_V + P_K}_{\Sigma P_{input}} = \underbrace{\dot{W}h + \dot{E}_a + \dot{E}_v + \dot{E}_p + \dot{E}_{wave}}_{\Sigma P_{outflow}} + \underbrace{\Phi_{total}}_{\Sigma P_{dissipation}} \tag{2.4}$$

In this equation, all terms on the left-hand side represent the power input into the control volume; whereas the first 5 terms on the right-hand side represent

total power outflow leaving the control volume. Finally, the last term on the right-hand side indicates the power dissipation inside the control volume, which can be considered power sinks.

$$\Sigma P_{input} = P_S + P_V + P_K \tag{2.5}$$

$$\Sigma P_{outflow} = \dot{Wh} + \dot{E}_a + \dot{E}_v + \dot{E}_p + \dot{E}_{wave} \tag{2.6}$$

$$\Sigma P_{dissipation} = \Phi_{total} \tag{2.7}$$

If we investigate the power input terms, P_K represents the net mechanical flow power imparted to the flow:

$$P_K = \oiint -[p - p_\infty + \frac{1}{2}\rho(V^2 - V_\infty^2)]\vec{V} \cdot \hat{n} dS_B = \oiint -[p_t - p_{t,\infty}]\vec{V} \cdot \hat{n} dS_B \tag{2.8}$$

This covers the mechanical power (both kinetic and potential) done to the control volume and equals the surface integration of the total pressure difference times the local flow velocity. It is non-zero only at propulsor inlet and exit surfaces. Note that $\hat{n}$ points into the propulsor such that the propulsor exit has a negative $\vec{V} \cdot \hat{n}$, and the inlet has a positive $\vec{V} \cdot \hat{n}$ value.

If we consider the power outflow terms, $\dot{Wh}$ represents the potential energy outflow rate of the control volume. If there are either altitude or weight changes in the control volume, this term is non-zero

$\dot{E}_a$ is the axial kinetic energy deposition rate at the control volume outlet, and can be written as:

$$\dot{E}_a = \iint \frac{1}{2}\rho u^2 (V_\infty + u) dS_O^{TP} \tag{2.9}$$

This represents how much axial kinetic energy rate (power) outflows the Transverse plane. Its kinetic energy rate is relative to the stationary ground, which is

a stationary reference frame. So, perturbation velocity components are used for the calculation. Its magnitude becomes high when there is a high velocity at the Transverse plane.

$\dot{E}_v$ is the kinetic energy outflow rate of the other perturbation velocity components in y and z directions, and can be written as:

$$\dot{E}_v = \iint \frac{1}{2}\rho(v^2 + w^2)(V_\infty + u)dS_O^{TP} \tag{2.10}$$

It is non-zero when there is a swirl in the flow. In the end, the kinetic energy outflow rate equals:

$$KE_{TP} = \dot{E}_a + \dot{E}_v \tag{2.11}$$

Another term, $\dot{E}_p$, is the pressure-work outflow rate, and can be expressed as:

$$\dot{E}_p = \iint (p - p_\infty)udS_O^{TP} \tag{2.12}$$

It is the rate of flow work outflows from the Trefttz plane, and non-zero when the static pressure is different from the ambient pressure.

The addition of the exit kinetic energy rate with the pressure work rate gives the total wake energy flow rate, $\dot{E}_w$, which is:

$$\dot{E}_w = \dot{E}_a + \dot{E}_v + \dot{E}_p = KE_{TP} + \dot{E}_p \tag{2.13}$$

$\dot{E}_{wave}$ is the wave energy outflow rate:

$$\dot{E}_{wave} = \iint [p - p_\infty + \frac{1}{2}\rho(u^2 + v^2 + w^2)]\vec{V} \cdot \hat{n}dS_O^{SC} \tag{2.14}$$

It is non-zero when there are shock waves in the flow.

The power dissipation, Φ_{total}, can be expressed as:

$$\Phi_{total} = \iiint (p - p_\infty) \nabla \cdot \vec{V} d\forall \tag{2.15}$$

It normally breaks into subcomponents according to where and how the dissipation occurs. The details of the other power terms and dissipation components are explained in Appendix A. Also in that part, some illustrative examples are shown in terms of how and which power components change inside the flow field. In the next section, the ways of quantifying the propulsion benefit are shown, and the possible problem with using the classical propulsive efficiency as a benefit metric is exemplified.

2.3 Power Balance Method Applied to a BLI Propulsor

2.3.1 Classical Propulsive Efficiency Calculation

To quantify the benefit of the BLI configuration with the classical propulsive efficiency, assume that the propulsor is located just downstream of the trailing edge of the airframe.

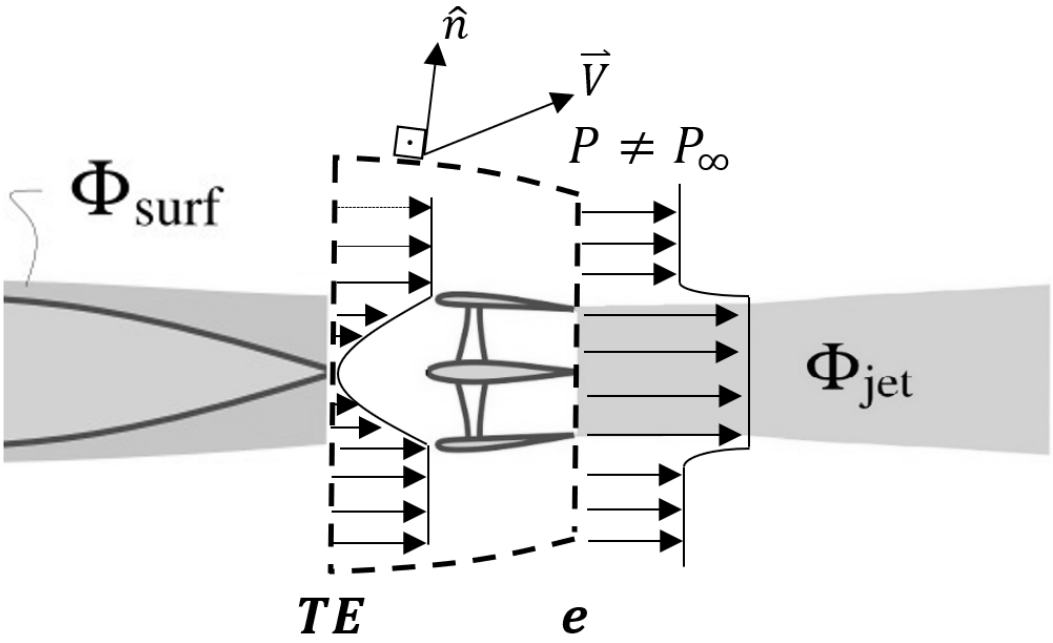

Figure 2.3: Control volume around a BLI propulsor [7]

Around the control volume which is shown by dashed lines in Figure 2.3, the power input and output terms can be decomposed as:

$$\Sigma P_{input} = P_K + \dot{E}_{a,TE} + \dot{E}_{v,TE} + \dot{E}_{p,TE} = P_K + KE_{TE} + \dot{E}_{p,TE} \tag{2.16}$$

$$\Sigma P_{output} = TV_\infty + \dot{E}_{a,e} + \dot{E}_{v,e} + \dot{E}_{p,e} = TV_\infty + KE_e + \dot{E}_{p,e} + \Phi_{CV} \tag{2.17}$$

For the power input terms, because the propulsor adds energy to the flow, there is a mechanical flow power imparted to the flow. The other power input terms are the kinetic energy deposition rate and pressure work power. These are considered as power input terms because the flow conditions at the inlet of the propulsor (or at the inlet of the control volume) are different relative to the free stream conditions.

Among the power output terms, thrust power is a useful power output term due to thrust generation. At the control volume exit, the flow conditions are different from the free stream. It is assumed that static pressure is not recovered to the free stream value, which makes $\dot{E}_{p,e}$ term non-zero. In this configuration, the control volume exit plane is located just after the propulsor such that there are no dissipation components due to the jet formation inside the control volume up to the exit plane. When we go further downstream of the control volume exit, whole power outflow terms should be dissipated and converted to Φ_{jet}.

From Equations 2.16 and 2.17, if we equate the power input and output terms (which is writing the power balance) for the BLI configuration, the following equation is obtained:

$$P_K + \underbrace{KE_{TE} + \dot{E}_{p,TE}}_{\dot{E}_{w,in}} = TV_\infty + \underbrace{KE_e + \dot{E}_{p,e}}_{\dot{E}_{w,out}} + \Phi_{CV} \tag{2.18}$$

Which can be simplified as:

$$P_K = TV_\infty + \dot{E}_{w,out} - \dot{E}_{w,in} + \Phi_{CV} \tag{2.19}$$

Equation 2.19 is the power balance equation that is written for a control volume around a BLI propulsor. By this equation, we can formulate propulsive efficiency. If we neglect Φ_{CV} due to the small control volume size around the propulsor, the classical Froude propulsor efficiency, η_p, can be defined as:

$$\eta_{p,BLI} = \frac{TV_\infty}{P_K} = \frac{P_K + KE_{TE} + \dot{E}_{p,TE} - (KE_e + \dot{E}_{p,e})}{P_K} = \frac{P_K - (\dot{E}_{w,out} - \dot{E}_{w,in})}{P_K} \quad (2.20)$$

$$\eta_{p,BLI} = 1 - \frac{(\dot{E}_{w,out} - \dot{E}_{w,in})}{P_K} \quad (2.21)$$

For the traditional configurations, which represent the free stream propulsor configurations, this equality is always smaller than unity (in the most ideal case, it is hypothetically unity). It is because the inlet velocity of the control volume is equal to the free stream velocity, which makes $KE_{TE} + \dot{E}_{p,TE}$ term zero, and as a result, makes $\dot{E}_{w,in}$ zero (see section A.1.2 in Appendix A). Different than the conventional configurations, however, in BLI, the above equation may not be always smaller than unity [36]. For the BLI case, $\dot{E}_{w,in}$ term is always positive due to the ingestion of the boundary layer. So, it is a power input term. In addition, in BLI systems, there may be some cases in which the propulsor almost ideally fills the airframe wake such that the velocity at the propulsor exit is almost equal to the free stream conditions ($KE_e \approx 0$). Also, $\dot{E}_{p,e}$ term is generally smaller than the $KE_{TE} + \dot{E}_{p,TE}$ summation. This results in:

$$KE_{TE} + \dot{E}_{p,TE} > (KE_e + \dot{E}_{p,e}) \quad (2.22)$$

And makes:

$$\dot{E}_{w,in} > \dot{E}_{w,out} \quad (2.23)$$

So, for these conditions, $\eta_{p,BLI}$ may be greater than unity.

$$\eta_{p,BLI} = 1 - \frac{(\dot{E}_{w,out} - \dot{E}_{w,in})}{P_K} > 1 \quad (2.24)$$

For this reason, there should be another quantification method for the BLI benefit metric rather than propulsive efficiency. The next section describes an alternative method.

2.3.2 Alternative Method for the BLI Benefit Calculation

Due to the possibility of the propulsive efficiency becoming greater than unity, the benefit of the BLI configuration is quantified as a Power Saving Coefficient (PSC), which can be expressed as:

$$PSC = \frac{P_{K,non-BLI} - P_{K,BLI}}{P_{K,non-BLI}} \tag{2.25}$$

This parameter can also be expressed with non-dimensional terms as in the following equation:

$$PSC = \frac{C_{PK,non-BLI} - C_{PK,BLI}}{C_{PK,non-BLI}} \approx \frac{C_{PE,non-BLI} - C_{PE,BLI}}{C_{PE,non-BLI}} \tag{2.26}$$

The non-dimensional C_{PK} term can be obtained as:

$$C_{PK} = \frac{P_K}{q_\infty S_{ref} V_\infty} \tag{2.27}$$

$$C_{PE} = \frac{P_E}{q_\infty S_{ref} V_\infty} \tag{2.28}$$

This power saving coefficient actually represents the amount of power that is reduced, to obtain the **same amount of net axial force** (acceleration or deceleration) in the BLI configuration compared to the non-BLI case. It is always smaller than unity. In some cases, rather than the mechanical flow power saving, sometimes the electrical power saving is used to quantify this coefficient (Equation 2.26). The energy transformation starts from the electrical power (P_E, if the fan works with electricity) to the shaft power by mechanical efficiency, and from shaft power to the flow by the fan efficiency. Since for a fixed system, these efficiency values are more or less constant, electrical power saving is approximately equivalent to mechanical flow power saving.

CHAPTER 3

NUMERICAL INVESTIGATION OF BLI

In this chapter, a numerical investigation of the BLI concept is performed. Firstly, one experimental study which is performed by Lv et al. [9] is taken as a reference to validate the numerical setup. After the validation, experimental geometry is modified, and the counter-rotating propulsor concept is applied to the BLI configuration. PSC values are calculated and some comparisons are made between single and counter-rotating propulsor concepts.

3.1 Validation of the Numerical Setup

In this section, to validate the CFD analyses which will be performed in the next section, an experimental study by Lv et al. [9] is taken as a reference. In this experimental work, a small propeller (APC 9x10) is placed behind a 1.35 m long axisymmetric fuselage to mimic a BLI configuration. The experimental setup is shown in Figure 3.1. Flow measurements, such as stereoscopic PIV and pressure field reconstruction, are done. Both BLI (Boundary Layer Ingestion) and WI (Wake Ingestion) configurations are investigated, but the focus was mostly on the WI configuration, and whole flow measurements are done on the WI configuration. Different than BLI, in WI configurations, the propulsor is put further away from the body so that the static pressure at the inlet of the propulsor is recovered to the free stream pressure. That is the only difference. Because the flow measurements are done on WI configuration, this is modeled as a validation study.

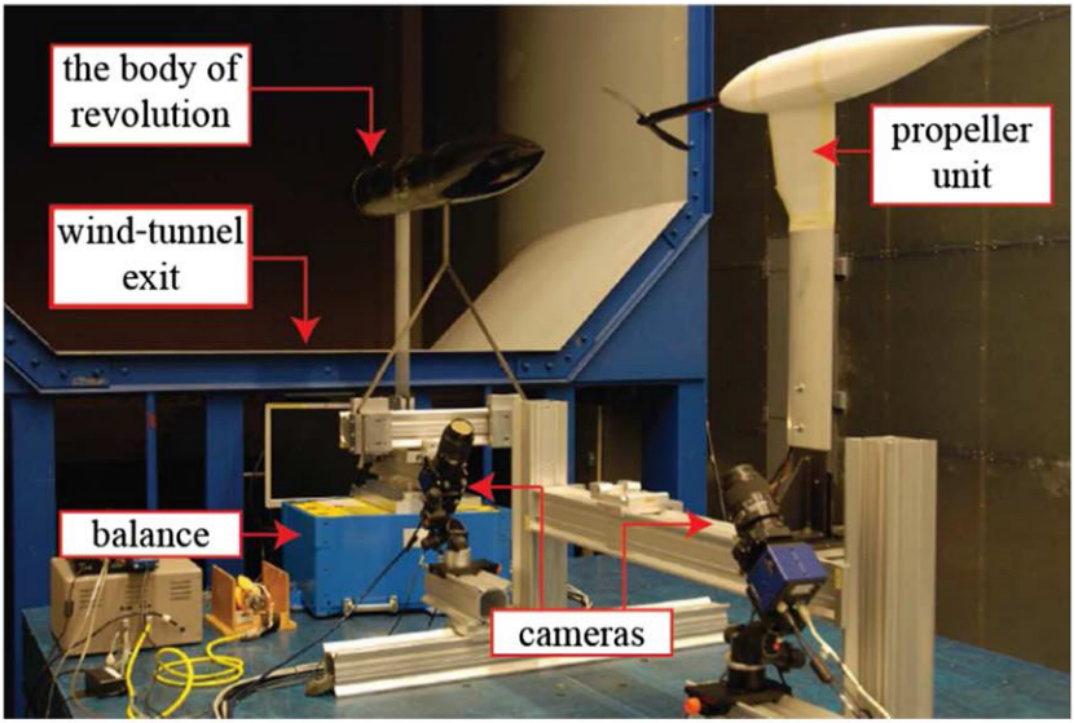

Figure 3.1: Experimental setup [9]

3.1.1 CFD Mesh and Flow Domain for the Validation Setup

CFD simulations are performed with ANSYS Fluent 18.2 version. Since the fuselage has an axisymmetric shape, rather than creating a 360° CFD domain, only 45° was modeled. With this feature, computational load is considerably reduced. The domain consists of a 45° section of a 5m radius cylinder. In Figures 3.2 and 3.3, the CFD geometry and flow domain are shown.

In the experimental setup, a trip wire is located at 1/5 of the length of the axisymmetric body (0.27 m from the nose) to make the flow turbulent after this region. The purpose of making the flow turbulent in the experiment is to prevent flow separation along the fuselage surface. So, to model this effect on CFD, the domain is divided into two cell zones. Before the trip wire location, the laminar cell zone condition is assigned in Fluent to mimic this effect. After this zone, turbulent flow begins. There are some studies that use the same approach [37, 38].

For this geometry, unstructured tetrahedral cells are used. Also, prismatic cells

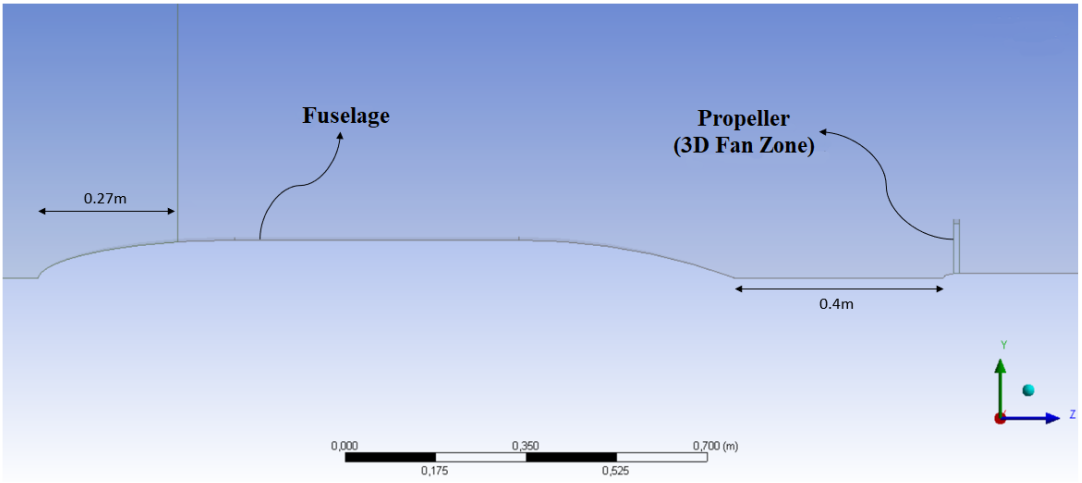

Figure 3.2: Side view of the fuselage and propeller cross section in the CFD domain

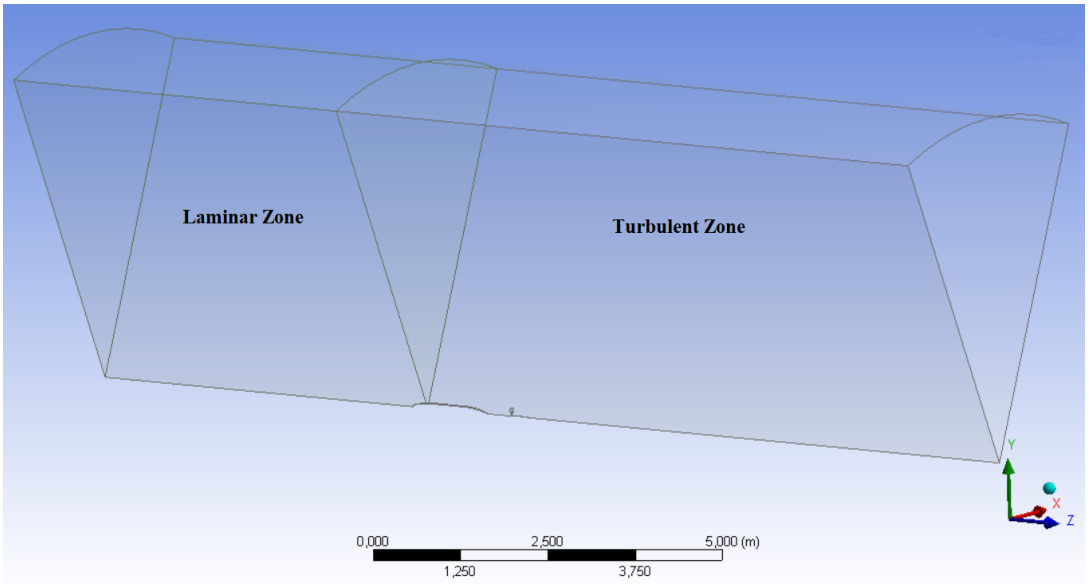

Figure 3.3: CFD domain

with a first layer thickness of $1x10^{-5}$ m are constructed to capture the boundary layer. In addition, a higher density of mesh is constructed around the body to resolve the flow and wake around the fuselage. The overall look of the CFD mesh is shown in Figures 3.4 and 3.5:

A mesh independence study is performed by investigating the wake profile after the body, which lies 100 mm upstream of the propulsor hub in Figure 3.11, to gen-

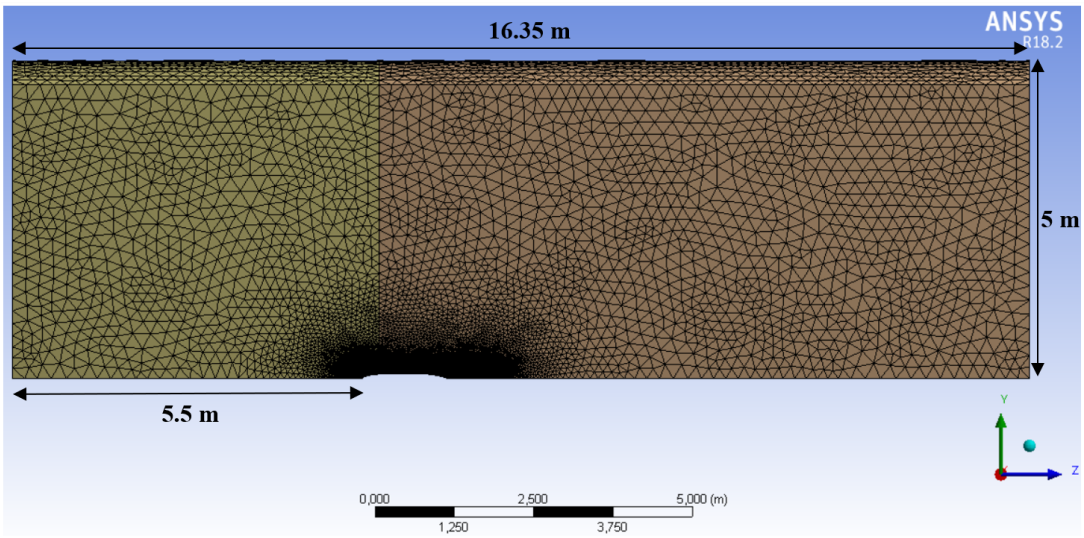

Figure 3.4: Overall look for the CFD mesh

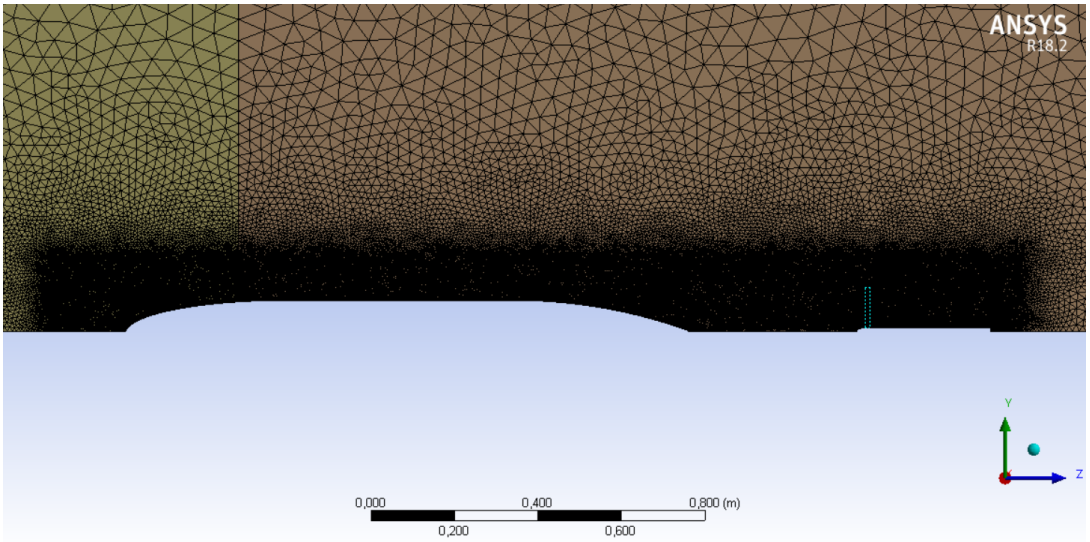

Figure 3.5: High density of mesh around the body and propeller

erate a reasonable mesh size. 2.45 million, 4.9 million, and 9.8 million elements are generated; after the 4.9 million cells, the velocity profile did not change considerably, especially around 0mm distance (near center). The percent difference between the 4.9 million mesh with respect to the 9.8 million mesh is less than 0.1%, which is also less than 2.07% with respect to the 2.45 million mesh size. The velocity profiles are shown in Figure 3.7. So, the mesh with 4.9 million elements is used for the solution. The properties of the generated mesh are given in Table 3.1.

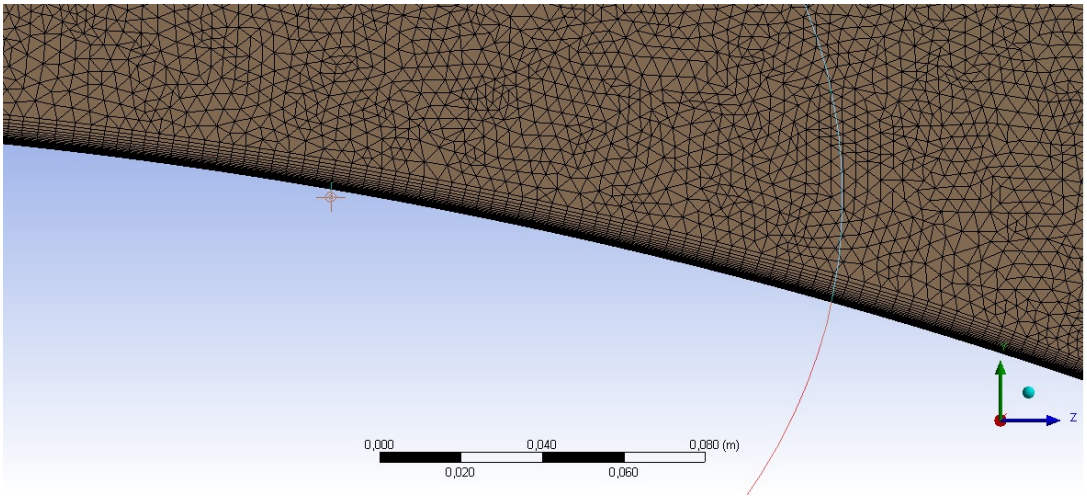

Figure 3.6: Boundary layer mesh around the body

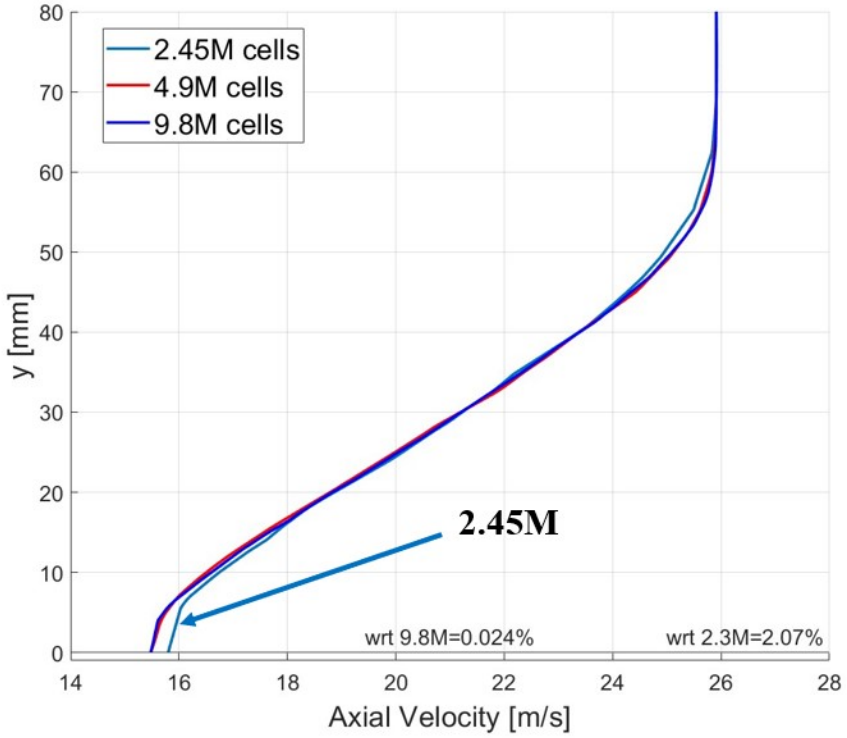

Figure 3.7: Velocity profiles for the mesh independence study

Table 3.1: Properties of the generated mesh

Mesh Size	Maximum Cell Skewness	Average Orthogonal Quality	Maximum y^+ Value on Walls
4.9 million	0.86	≈ 0.8	0.43

3.1.2 Boundary Conditions

The boundary conditions for the numerical setup are shown in Figure 3.8. The velocity inlet with 26m/s free stream velocity and zero-gauge pressure outlet boundary conditions are assigned for the inlet and outlet, respectively. The interface boundary condition is given between the laminar and turbulent cell zones. Also, the symmetry boundary condition is assigned for the upper surfaces of the domain. Normally, the flow is not symmetric after these surfaces, but to avoid viscous effects around these faces, this boundary condition is assigned. For the viscous walls such as the fuselage surface and propeller hub, the wall boundary condition is used. Periodic boundary conditions are assigned on side surfaces to obtain 360° periodicity. For the propeller modeling, rather than using a fan boundary condition (like an

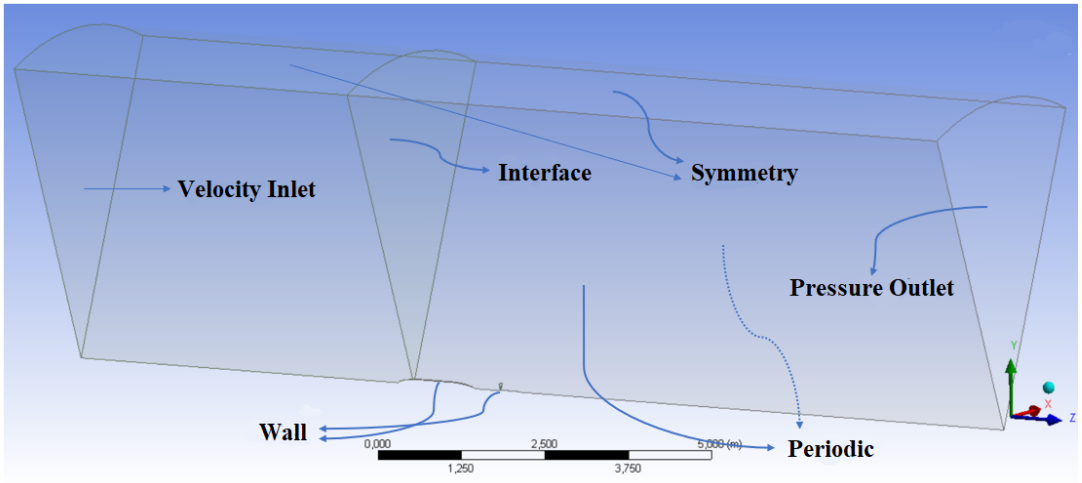

Figure 3.8: Boundary conditions for the numerical setup

actuator disc model), a cell zone condition 3D Fan Zone is assigned in Fluent. Due to the simplicity and more comparable results with the multiple reference frame

approaches, this cell zone condition is chosen. With this condition, radial and tangential momentum source terms can also be given to the flow in addition to the axial ones (pressure jump). So, the flow can be 3-dimensionally modeled. In the reference experiment, the propeller rpm was chosen around 6200 rpm. Also, the propeller generated approximately 1.40 ∓ 0.04 N thrust. Considering these thrust and rpm values, 6200 rpm and 33.5 Pa constant pressure jump with tangential momentum source terms are assigned to the 3D fan zone. To determine the pressure jump, the thrust value is divided by the propeller frontal swept area, which is around 0.041 m^2.

To mention the solver settings, the incompressible constant density setting, which is set as 1.225 kg/m^3, is assigned to the Fluent. The coupled solver with the 2^{nd} order discretization schemes is applied. The solution is iterated until the wake profile is sufficiently converged to constant velocities.

3.2 Application of the Counter-Rotating Propulsor Concept

After the validation, the counter-rotating propulsor concept is investigated for a similar axisymmetric body. Different than the validation case, the cross-section and length of the body are increased to have a thicker wake, which should match the propulsors' radii. This is more apparent in Figure 3.10. The propulsor dimensions are kept the same.

The same domain dimensions and boundary conditions in the validation setup are applied for the counter-rotating concept. The mesh with approximately 5 million elements is created. The distance between the two counter-rotating propulsors is kept at 40 mm. Also, free stream velocity is decreased to 11 m/s.

In the experiment, APC 9x10 propeller was used. For the counter-rotating concept, when assigning the corresponding pressure jump and rpm values to the 3D Fan Zone region in Fluent, the performance data for the APC 9x10 propeller are used [39]. First, no pressure jumps are given to the 3D Fan zone regions. On that condition, at the incoming low-velocity wake in front of the propulsor, an average velocity is taken. According to this lower average flow velocity, the rpm

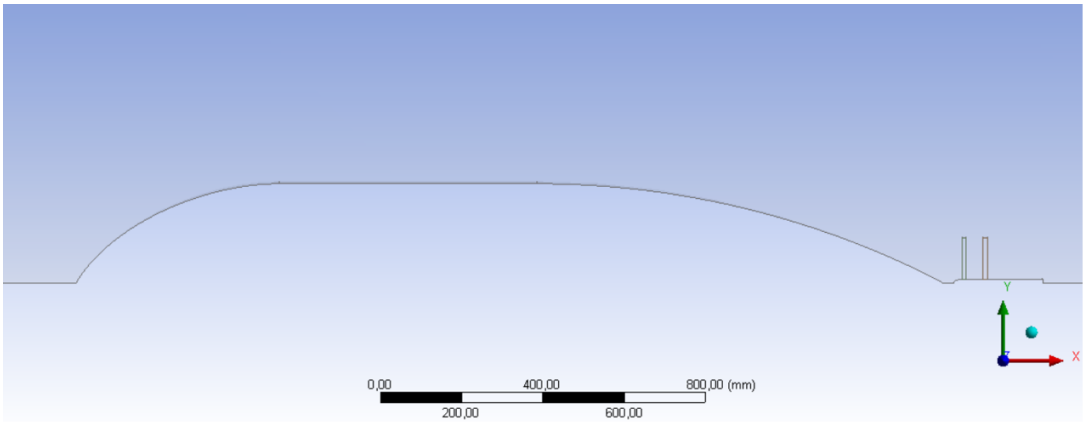

Figure 3.9: Counter-rotating propulsor configuration with the modified axisymmetric body

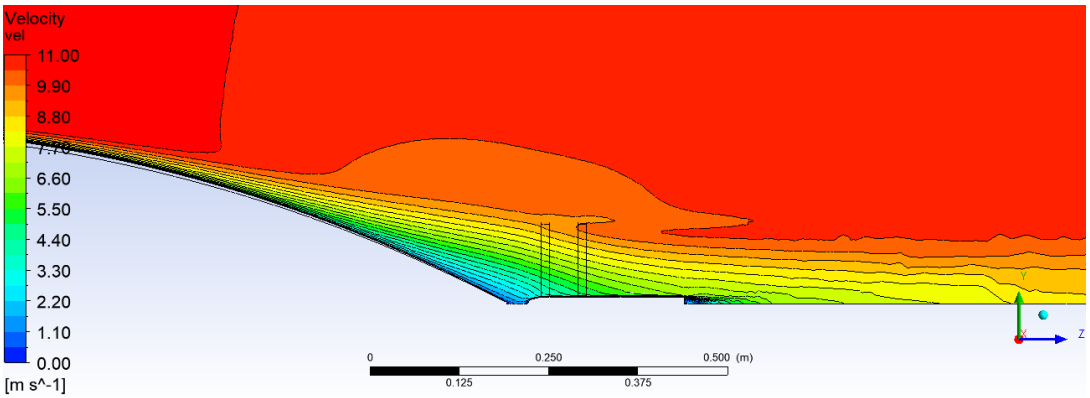

Figure 3.10: Velocity contours for the counter-rotating propulsors concept in BLI configuration

values are selected which correspond to the specified pressure jump values. The values are approximate, but within the rpm ranges based on the performance data. In addition, rather than calculating the PSC only for cruise conditions (constant velocity), it is calculated for different net axial forces, such as acceleration and deceleration scenarios. So, different pressure jumps and rpm values are assigned to 3D Fan Zones. 5 different net axial force conditions are simulated. The propulsor conditions for these 5 different cases in BLI configuration are shown in Table 3.2.

Table 3.2: 3D Fan Zone properties for the BLI configuration at different net streamwise forces

Case	Net streamwise force [N] (Drag-Thrust)	Pressure jump [Pa] (Front propeller)	Rotational speed [rpm] (Front propeller)	Pressure jump [Pa] (Aft propeller)	Rotational speed [rpm] (Aft propeller)
1	0.6012	5	2000	5	2050
2	0.4244	7.5	2100	7.5	2150
3	0.1378	11.5	2400	11.5	2450
4	-0.2985	17.5	2800	17.5	2900
5	-0.8513	25	3200	25	3300

For the front and aft propellers, the same pressure jump values are assigned, but the rpm value for the aft propeller is slightly higher than the front one. The reason for this assumption stems from the fact that the aft propeller exposes higher inlet velocities due to the small jet formation of the front one. These rpm values are interpolated based on the performance data for APC 9x10 propeller, so they are approximate values. The performance data of the propeller are available on the product's website [39].

The same simulation and methodology are applied for the isolated propulsors configuration to compute the PSC. The 3D Fan Zone properties for this configuration are given in Table 3.3.

Table 3.3: 3D Fan Zone properties for the isolated counter-rotating propulsor configuration at different net streamwise forces

Case	**Net streamwise force [N] (Drag-Thrust)**	**Pressure jump [Pa] (Front propeller)**	**Rotational speed [rpm] (Front propeller)**	**Pressure jump [Pa] (Aft propeller)**	**Rotational speed [rpm] (Aft propeller)**
1	0.5446	5	2200	5	2250
2	0.3421	7.5	2300	7.5	2350
3	0.0180	11.5	2600	11.5	2700
4	-0.4682	17.5	3100	17.5	3200
5	-1.0759	25	3500	25	3600

In the isolated propulsors case, higher rpm values are assigned compared to the BLI configuration with the same pressure jump values. The reason for this is that the propulsors are exposed to higher flow velocities compared to the BLI configuration to generate the same amount of thrust.

For these different flow conditions, the mechanical flow power, P_K, and the net streamwise forces, F_N, can be nondimensionalized as:

$$C_{PK} = \frac{P_K}{q_\infty S_{ref} V_\infty} \tag{3.1}$$

$$C_{FN} = \frac{F_N}{q_\infty S_{ref}} \tag{3.2}$$

$$F_N = D - T \tag{3.3}$$

Also, S_{ref} is taken as 0.196 m^2, which is the frontal cross-sectional area of the modified body. V_∞ is taken as 11 m/s. The density is taken as 1.225 kg/m^3, and the incompressible constant density condition is applied.

3.3 Results

3.3.1 Validation Setup CFD Results

To compare the numerical and experimental values and determine the proper turbulence model, velocity profiles are investigated at 100 mm upstream and downstream of the propeller. In the reference experiment, the flow is assumed as axisymmetric. Also, even though there are some small transient operations in the experiment, the problem is assumed as a steady state. So, steady-state CFD analyses are performed in the numerical setup. In Figure 3.11, the velocity profiles of the two lines that are at 100 mm upstream and downstream of the propeller hub nose are shown.

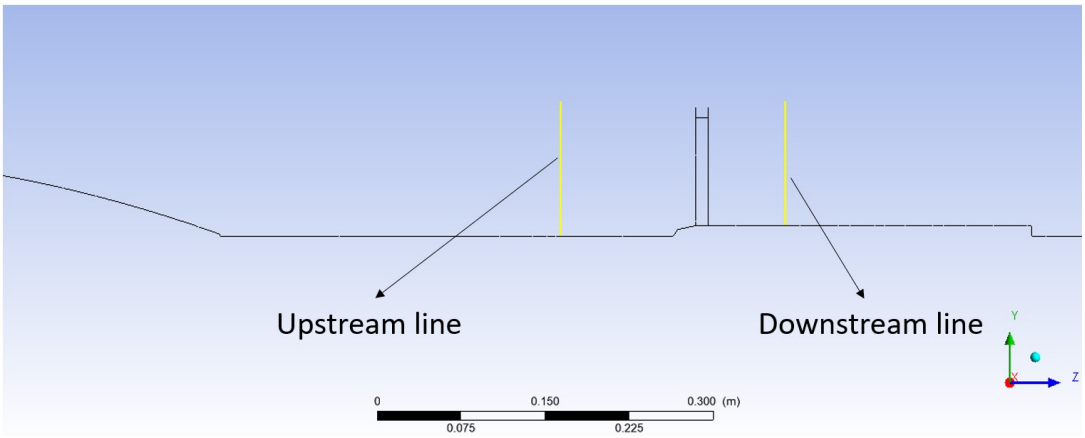

Figure 3.11: Upstream and downstream lines shown in yellow at which the velocity profiles are taken

The velocity profiles which are obtained with different turbulence models across these two lines are shown in Figure 3.12. The closest turbulence model results to the experimental profile are shown.

If we look at the velocity profiles, the k-ω SST turbulence model has the closest profile to the experiment. The CFD problem was also solved by standard k-epsilon, k-epsilon realizable, RNG k-epsilon, and Reynolds Stress turbulence models. Among these and other closer turbulence models in Figure 3.12, k-ω SST is chosen for the solution. For this setup, the solution is converged in 800 iterations

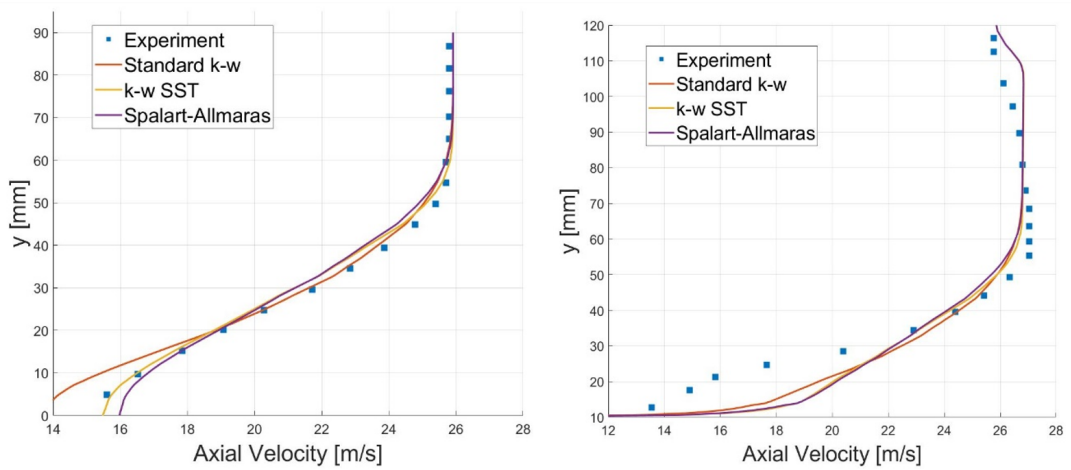

Figure 3.12: Velocity profiles at 100 mm upstream (left) and 100 mm downstream (right) from the nose of the propeller hub

with a maximum residual of $1x10^{-5}$, which is shown in Figure 3.13.

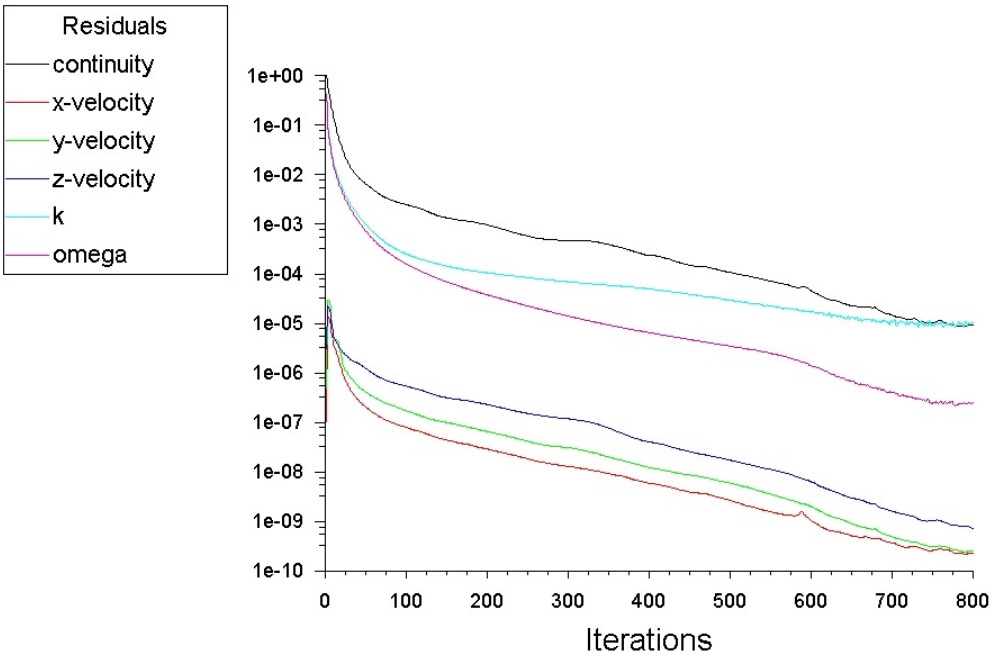

Figure 3.13: The residuals for the k-ω SST solution

Also, nondimensional pressure coefficient values for both CFD and experimental results are shown in Figure 3.14.

Among these results, when we look at the upstream velocity profile, it can be said that it is quite consistent with the experimental values. However, the downstream

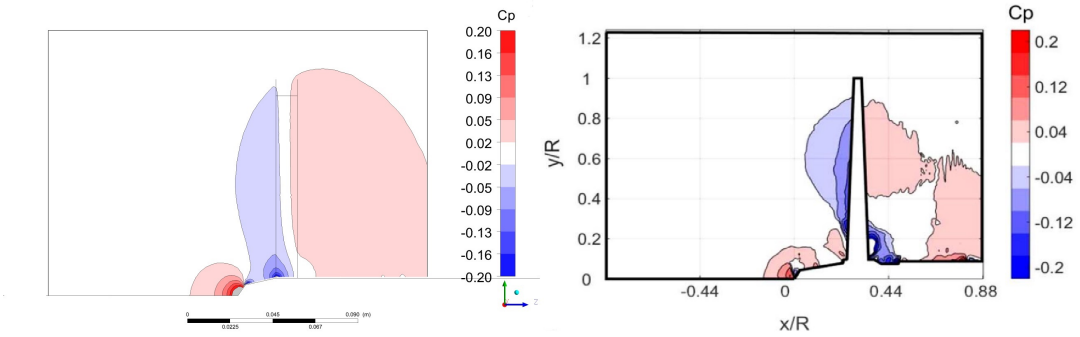

Figure 3.14: Pressure coefficient contours obtained by CFD (left) and experiment (right) [9]

profile has some minor differences. Near the hub, the CFD solution predicted higher velocities compared to the experiment. This can be caused by the higher pressure jumps in the CFD solution near the hub. Also if we look at the pressure coefficient contours, it can be confirmed that a lower pressure rise near the hub occurred in the experiment compared to CFD. This higher pressure rise in CFD may be the cause for the little difference between the CFD and experimentally determined downstream velocity profiles. Also, pressure rise across the propeller is quite nonhomogeneous in the experiment, but this effect is not modeled in CFD. In fact, a constant (33.5 Pa) homogeneous pressure jump is assigned in the numerical solution. So, the differences are mostly caused by this fact. In addition, near the tip of the blades, CFD predicted a higher velocity profile. This can be caused by the tip vortices that occurred in real life, which are present in the experiment. Because propeller blades are not present in CFD, this effect could not be modeled as well.

In addition, in the reference experiment, the drag force of the body was estimated as 1.20 N; but the drag of the body strut was included in this value. When we look at the original study, which is from Hartuçs experiment [40], the drag of the body alone is estimated at approximately 0.81 N. The drag of the isolated body with and without assigning the laminar zone option in Fluent for different turbulence models are given in Table 3.4.

Table 3.4: Drag force of the isolated body with different turbulence models in CFD

Turbulence Model	**Drag with Laminar Zone Option [N]**	**Drag without Laminar Zone Option [N]**
standard k-ω	0.8339	0.9018
k-ω SST	**0.8262**	0.9240
k-ϵ realizable	1.1821	1.3317
RNG k-ϵ	1.2645	1.4215
standard k-ϵ	1.3266	1.5041
Spalart Allmaras	0.8545	0.9547
Reynolds Stress Model	1.2154	1.3345

With the current turbulence model, the drag force is consistent with the experimental value, which is around 0.81 N. So, k-ω SST model with a laminar zone option has a good agreement, which has a 0.8262 N drag value.

Another performance value that is compared with the experiment is Power Saving Coefficient (PSC). In order to obtain the mechanical flow power imparted to the flow, a control volume around the propulsor needs to be generated and the mechanical flow power,P_K, should be calculated using Equation 2.8. In Figure 3.15, the boundaries of the control volume are shown.

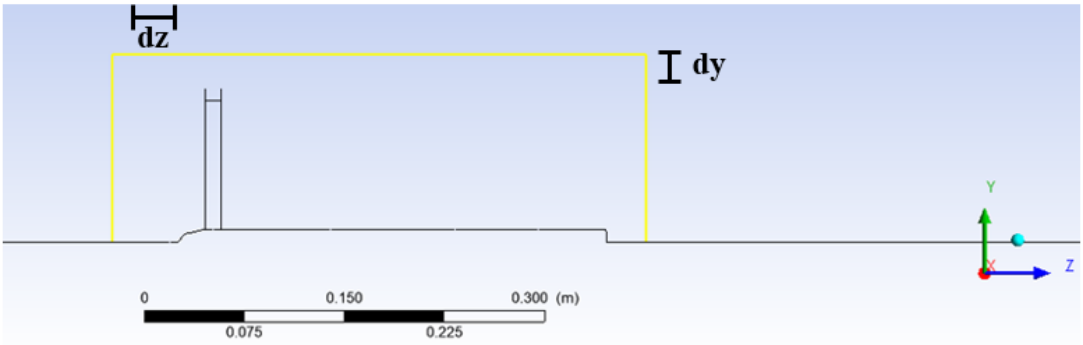

Figure 3.15: Boundaries of the control volume around the propulsor

For the analysis, 2D lines are created for the control volume boundaries. The reason for taking lines to construct the control volume boundaries rather than

surfaces stems from the assumption of axisymmetry. In the CFD-Post software, the lines are divided into equal nodes and the data are taken from these nodes. After taking the required data at each node and the interpolation between node values on the line, surface integral was taken by revolving the boundaries by 360°. For the vertical inlet and outlet lines, which lie on the y-axis in the radial direction in Figure 3.15, the surface integral was taken as[9]:

$$\iint \Phi dS = \int_0^R \Phi 2\pi y \, dy \tag{3.4}$$

And for the side surface, which can be constructed by revolving the horizontal line in Figure 3.15 on the central axis and has a constant radius R, the integral can be written as:

$$\iint \Phi dS = \int_{z_{inlet}}^{z_{outlet}} \Phi 2\pi R \, dz \tag{3.5}$$

And the variable Φ in Equations 3.4 and 3.5 represents the integrand, which is $\Phi = (p_t - p_{t,\infty})\vec{V} \cdot \hat{n}$ to calculate the P_K.

As another approach, the actual node values which are determined by the mesh intensity and require no interpolation are taken and the results are compared to each other. For these line data, the flow axisymmetry should be checked by obtaining the velocity and total pressure variation along one radial location. In Figure 3.16, this variation is shown. In addition to this, the control volume is also constructed by creating user-defined surfaces at the control volume boundaries and taking the area integral in Fluent.

Because control volume boundaries are lines, which requires the assumption of axisymmetry for the flow, this property should be checked. To check this condition, axial velocity and total pressure data are taken near the hub and tip from the radii of 0.025 m and 0.1 m downstream of the propulsor. The variations are shown in Figure 3.17. From the angular variation of velocities and total pressures, it can be said that the flow is mostly axisymmetric. Even if the values change slightly, it corresponds to less than 1/1000 of the mean values. So, the axisymmetry assumption

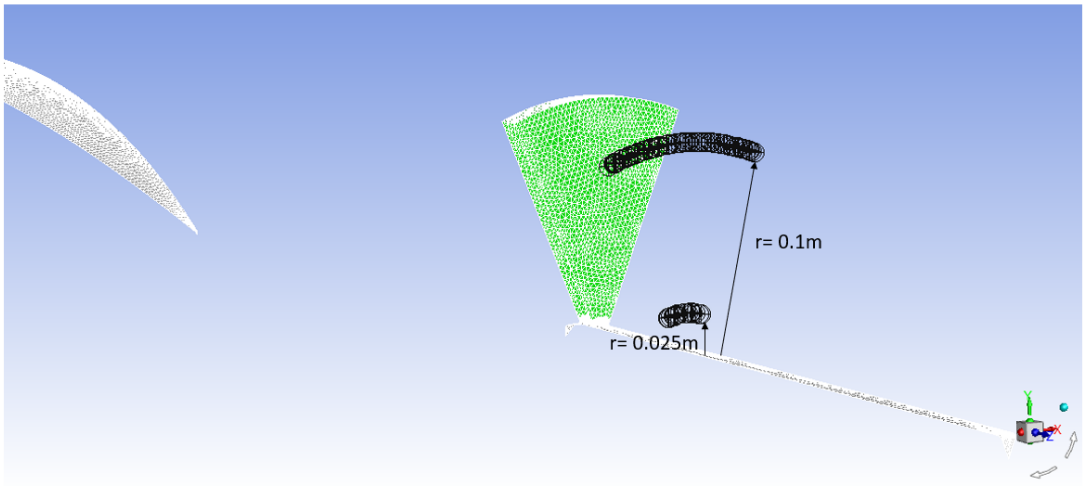

Figure 3.16: Radial locations at which the data are taken

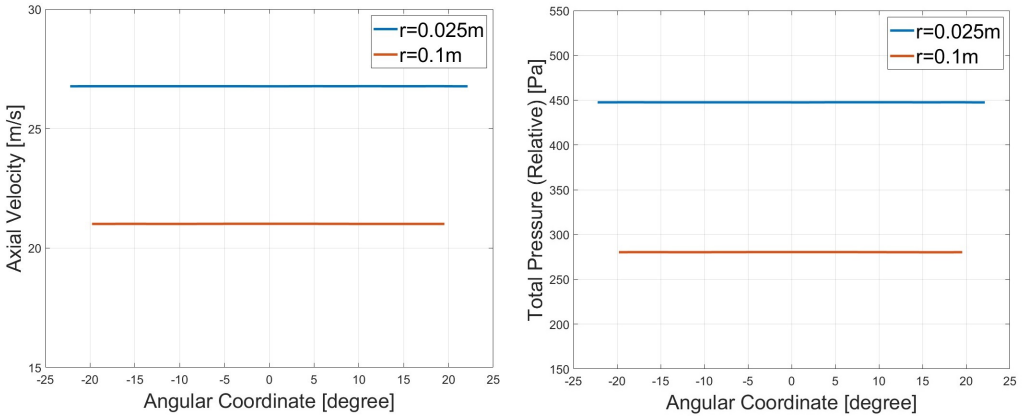

Figure 3.17: Angular variation of axial velocity (left) and total pressure (right)

is valid.

The same control volume is taken, and the same calculations are done for the isolated propulsor configuration. With the total pressure and axial velocity data on the control volume boundaries, using Equation 2.25, the PSC value is calculated as 6.7% for the interpolated data and 6.6% for the actual node values which require no interpolation. Also, with creating the user-defined surfaces, PSC is calculated as 7.1%. Because there is no considerable difference between them, the interpolated data was taken. In the reference experiment by PIV measurements, this value was found as 8.3% $\mp$ 1.7. The CFD finding is in the uncertainty range of the

experimental one, which means that the simulation value is consistent.

In addition, in Figure 3.18, the velocity contour for the wake of the body is shown. It can be said that the thickness of the wake that is generated by the presence of the body is about half of the propeller radius. This situation has a significant role in the PSC value, depending on the amount of the body wake ingested by the propulsor.

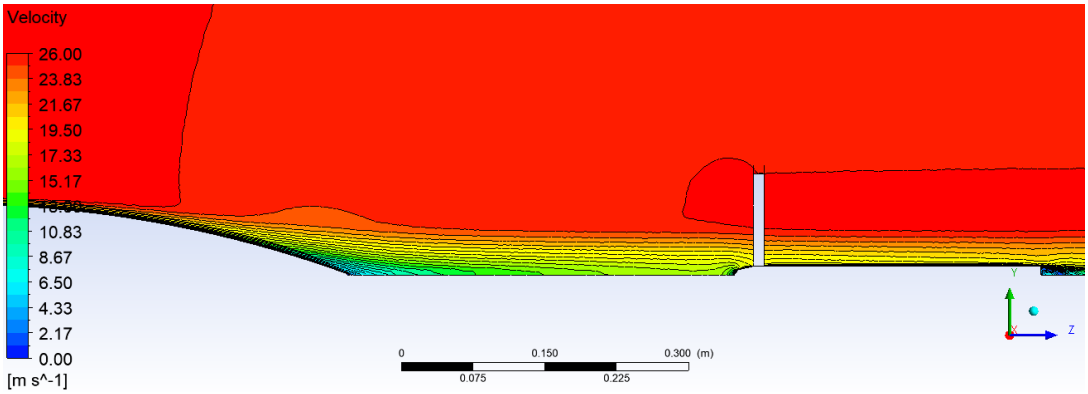

Figure 3.18: Velocity contours around the body wake

3.3.2 The Counter-Rotating Propulsor Application CFD Results

For the counter-rotating propulsor configuration in Figure 3.9, similar control volumes as in Figure 3.15 are taken. They are shown in Figure 3.19.

Around that control volume, C_{FN} and C_{PK} values are calculated. The plot is shown in Figure 3.20.

Figure 3.20 shows that there is a linear relationship between C_{FN} vs C_{PK}. The coefficient of determination (R^2) values are also indicated in the figure. To calculate the PSC using Equation 2.26, the C_{PK} values for both configurations should be compared for the same net streamwise force coefficient. The C_{PK} values are obtained by Equation 3.1, and the P_K values in that equation are calculated by taking the surface integral of Equation 2.8 for all control volume surfaces as in Figure 3.15. The propulsor dimensions are kept constant, so the only modification is changing the fuselage dimensions and decreasing the free stream velocity. For the cruise condition, which corresponds to zero C_{FN} value, the PSC is found

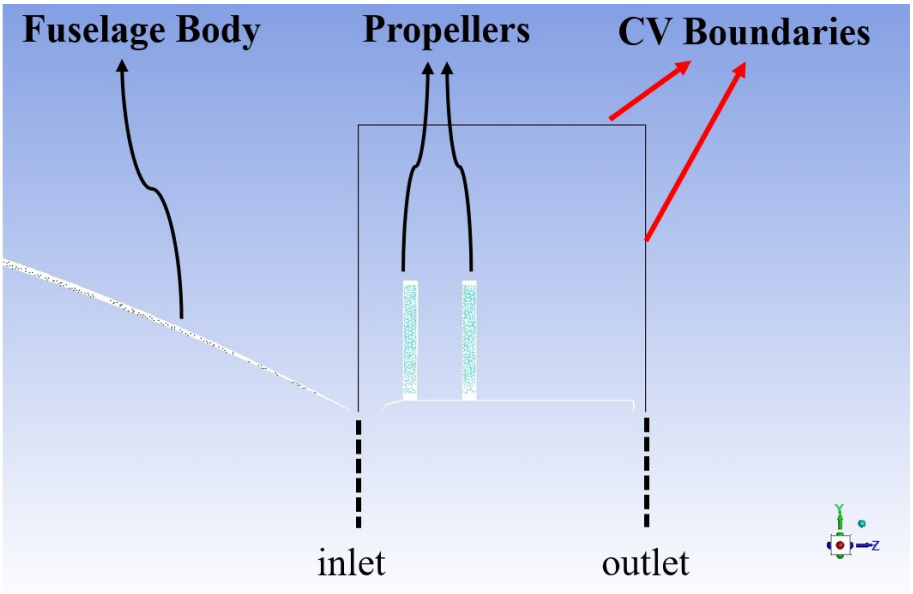

Figure 3.19: Control volume boundaries for the counter-rotating concept

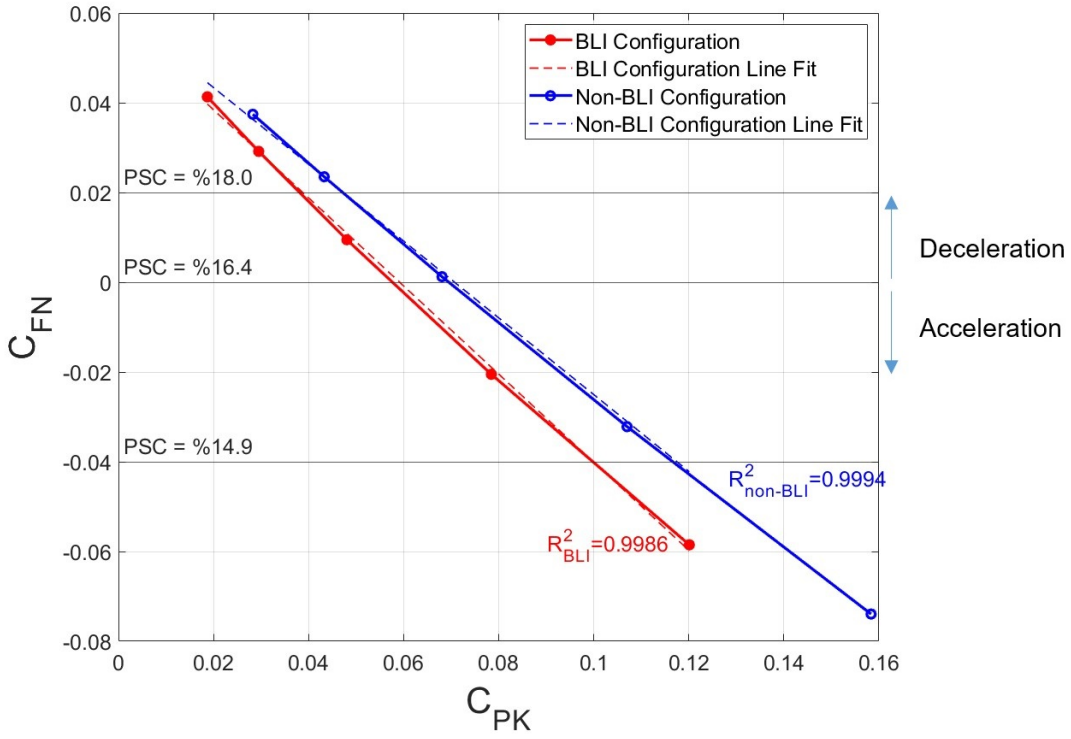

Figure 3.20: Mechanical flow power coefficient vs net streamwise force coefficient plot for both configurations (Adapted from [10])

as 16.4%. Towards deceleration, the PSC value tends to increase. On the other hand, the converse is true for the acceleration case.

Also on the inlet and outlet control volume boundaries shown in Figure 3.19, the power outflow and inflow components are calculated for both BLI and non-BLI configurations. If we refer to Equation 2.19, we can rewrite the power balance as:

$$P_K = TV_\infty + \underbrace{\dot{E}_{w,out} - \dot{E}_{w,in}}_{\dot{E}_{w,net}} + \Phi_{CV} = TV_\infty + \dot{E}_{w,net} + \Phi_{CV} \tag{3.6}$$

This $\dot{E}_{w,net}$ term represents the total net wake power outflow component, including the propulsor wake and the body wake. If this quantity is higher, the total amount of power that is wasted out to the flow is also higher. In Figure 3.21, the variation of propulsor mechanical flow power input P_K and $\dot{E}_{w,net}$ with respect to the net streamwise force can be seen.

In Figure 3.21, we see that the net wake power outflow terms for the BLI configuration, $\dot{E}_{w,net,BLI}$, are all negative and smaller than the ones in the non-BLI configuration, $\dot{E}_{w,net,non-BLI}$. This shows that wake power outflow of the fuselage body, $\dot{E}_{w,in,BLI}$, which is a power input term in Equation 3.6, is bigger than the propulsor wake power outflow term, $\dot{E}_{w,out,BLI}$. This is because of the low flow velocities around the BLI propulsor. At the inlet of the BLI propulsor, the flow velocity is lower than the free stream; and after the propulsor energizes the flow, it is still lower than the free stream, but a closer value to the free stream velocity. So this makes $\dot{E}_{w,in,BLI}$ much bigger due to large deviation from the V_∞, causes $\dot{E}_{w,net,BLI}$ to be negative. Also as described in Equation 2.24, this negative value makes $\eta_{p,BLI}$ bigger than one. The positive values of the $\dot{E}_{w,net,non-BLI}$ in non-BLI configuration shows that $\eta_{p,non-BLI}$ is always smaller than one, and $\dot{E}_{w,net,non-BLI}$ value increases with the throttle setting which is an indicator of the wasted power.

In addition, for the same fuselage geometry and setup, a single propulsor concept is applied instead of the counter-rotating one. The configuration is shown in Figure 3.22. The reason for the application of a single propulsor concept is to compare the PSC values with the counter-rotating one. To generate the same

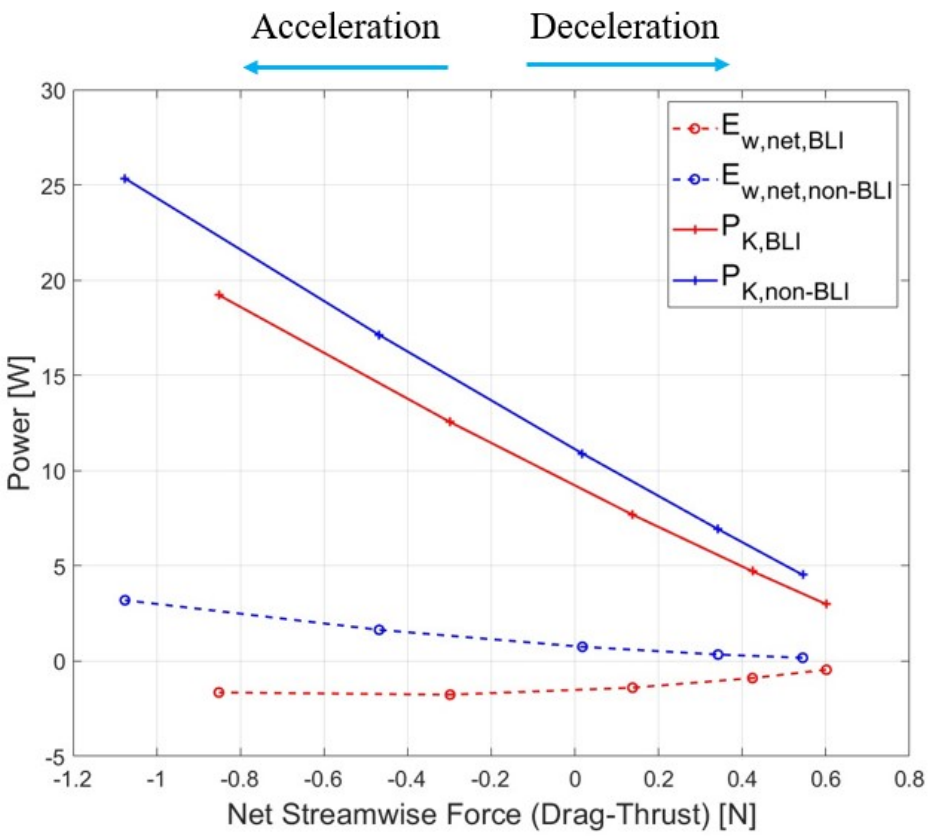

Figure 3.21: Net wake power outflow and propulsor mechanical flow power input changes with respect to the net streamwise force

amount of thrust, the same overall pressure jump values are assigned to the 3D Fan Zone region. The propulsor conditions for the single propulsor concept are given in Table 3.5.

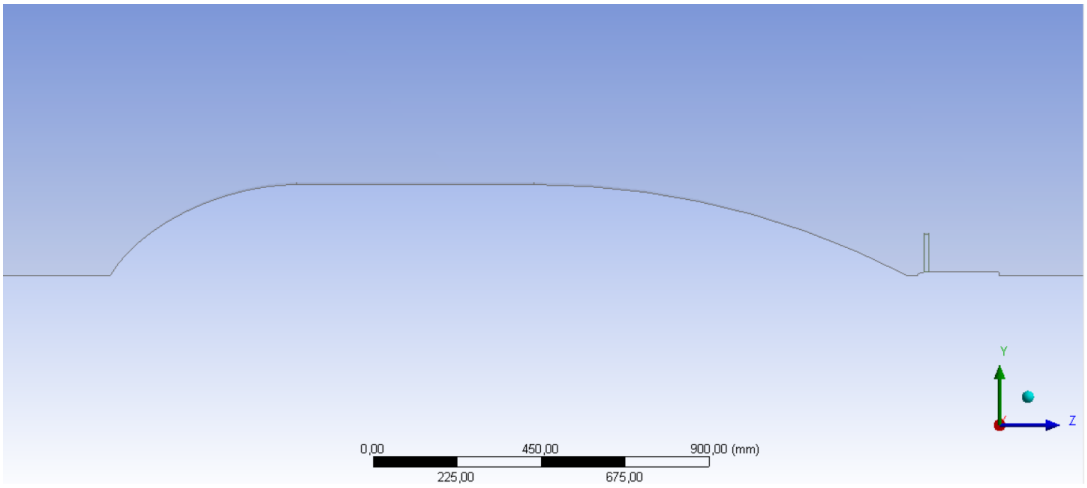

Figure 3.22: Single propulsor concept applied for the same fuselage geometry and setup

Table 3.5: 3D Fan Zone properties for the single propulsor concept at different net streamwise forces

Case	Net streamwise force [N] (Drag-Thrust)	Pressure jump [Pa]	Rotational speed [rpm]
1	0.6391	10	2400
2	0.4656	15	2900
3	0.1840	23	3400
4	-0.2458	35	3850
5	-0.7915	50	4400

When we compare the PSC of the counter-rotating propulsors relative to the single propulsor concept, we obtain Figure 3.23.

In Figure 3.23, it is observed that the counter-rotating concept spends 3.3% less power with respect to the single propulsor concept for the cruise condition ($C_{FN} = 0$). Actually, this finding was found by other researchers. Wang et al. [41] compared the counter-rotating propeller pair with a single propeller configuration, and found 40% shaft power reduction for the same amount of pressure jump (or thrust generation). In this study, the benefit is much less than this but shows a

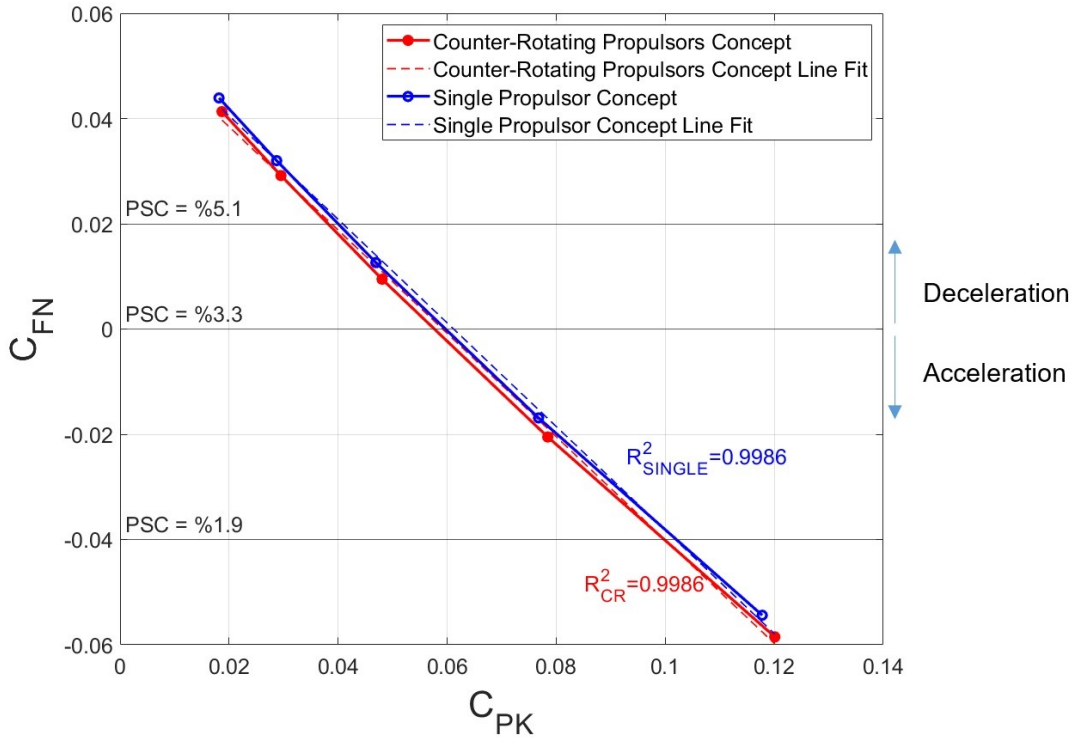

Figure 3.23: Mechanical flow power coefficient vs net streamwise force coefficient plot for counter-rotating propulsors and single propulsor concepts with the swirling motion

reasonable trend. Also, other studies showed the aerodynamic benefit of this configuration [42]. The reason behind this reduced power consumption can be the recovery of the swirl (which is generated by a tangential momentum source in 3D Fan Zone) that is produced by the propulsor. Rather than a single rotating propulsor, two counter-rotating ones are canceling the overall swirl that is generated by one propulsor. To see this effect, around the outlet side of the control volume lines (the line at the outlet of the fan in Figure 3.15), the line average of the circumferential velocities around the zero net streamwise for the same pressure jump values are compared with each other. The average circumferential velocities are found as 1.1x10^{-3} m/s and 4.6x10^{-3} m/s for the counter-rotating concept and the single propulsor concept, respectively. The swirling velocity is lower for the counter-rotating concept compared to a single one. The values are small, but the relative amount is considerable. Also, similar CFD analyses are performed without

adding the swirling motion to 3D fan zones, which resembles a simple 3D actuator disc propulsor. The overall results can be seen in Figure 3.24.

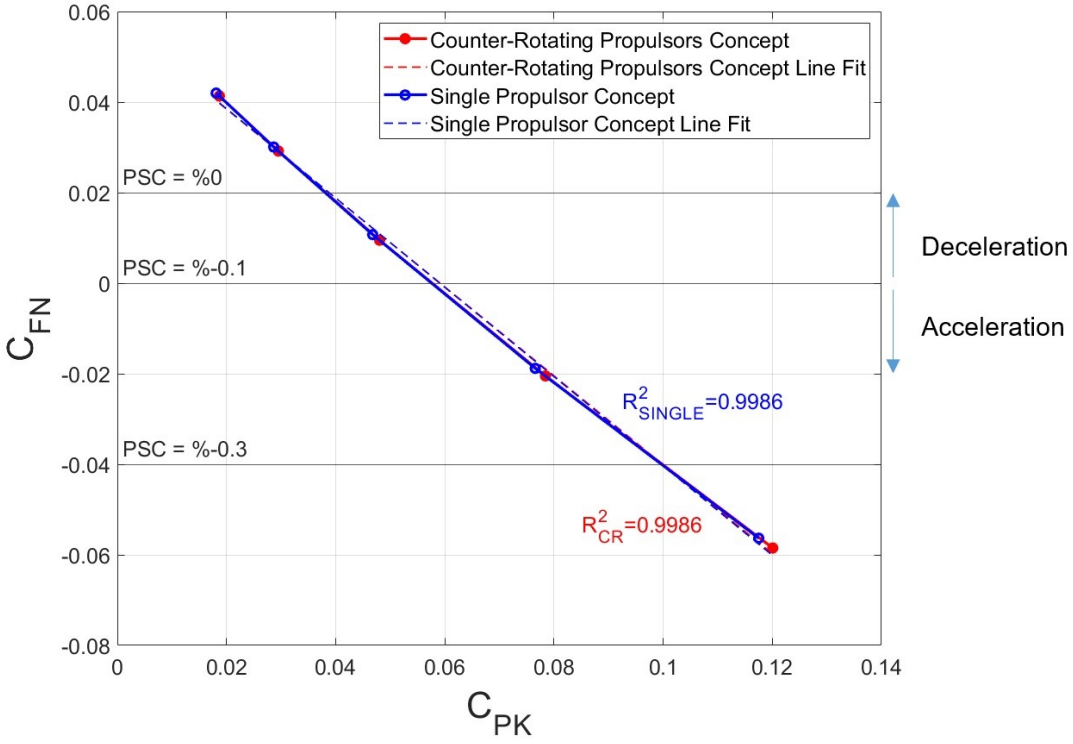

Figure 3.24: Mechanical flow power coefficient vs net streamwise force coefficient plot for counter-rotating propulsors and single propulsor concepts **without** the swirling motion

From Figure 3.24, we can understand that the two concepts consume almost the same power, which means no difference between them. So, it can be concluded that the main benefit driver for the counter-rotating propulsors can be caused by the recovery of the swirl. Actually, it doesnt mean that the all benefits of the counter-rotating propulsors come from the recovery of the swirl. The other reason can be the distribution of the thrust load by the presence of multiple propulsors rather than the single one; which in the end affects the rpm values and fan (or propeller) efficiencies. In reality, this also reduces the power consumption, but because the propulsor blades are not present in this numerical setup, the only benefit driver here is the recovery of the swirl. In literature, other counter-rotating propulsor configurations are produced such as propfans [43] or other open rotor

configurations [44, 45, 46]. In addition, there are some other propulsor or propeller configurations that recover the swirl with different structures such as swirl recovery vanes [47, 48, 49, 50, 51, 52], but this is beyond the scope of this study.

In addition to this, as a different variable, the impact of the axial distance between counter-rotating propulsors on the PSC is investigated. With the same equally distributed pressure jump to the propulsors, the axial distance is varied from 20 mm to 80 mm with the 10 mm increment. The PSC values for the cruise condition relative to the single propulsor are shown in Figure 3.25.

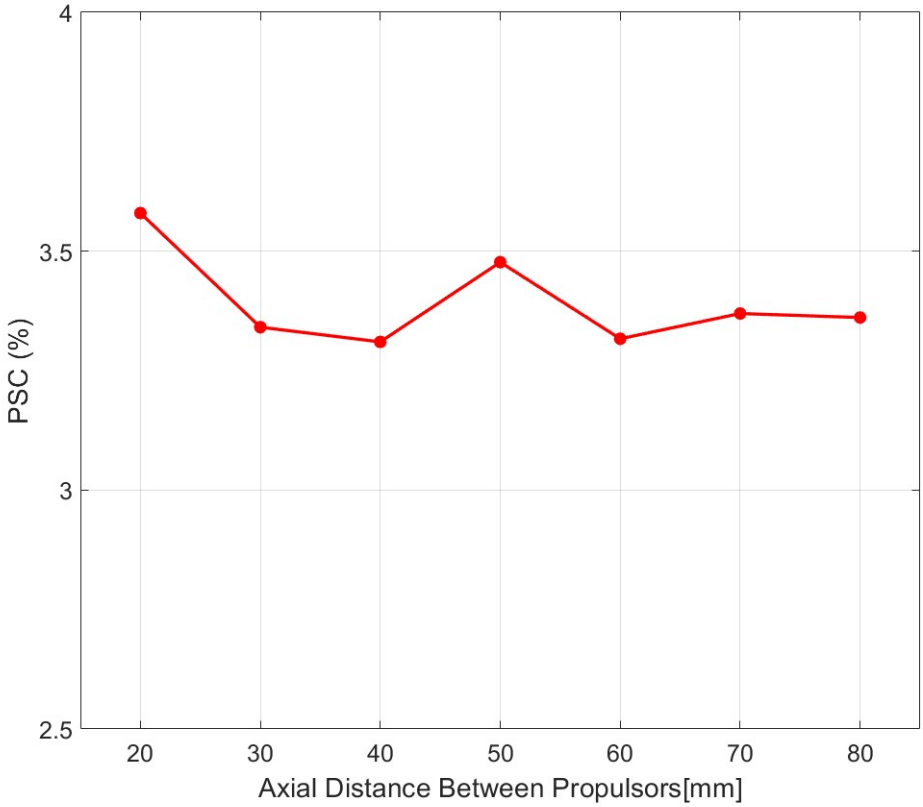

Figure 3.25: Axial distance between two propulsors vs power saving coefficient for the cruise condition relative to the single propulsor

From Figure 3.25, we can conclude that the PSC values remain almost the same when the axial distance between the propulsors is varied with the same pressure jump and thrust values. A similar conclusion was done by some research, which shows that increasing the axial distance has no considerable amount of aerodynamic performance change [41, 42]. The only benefit of increasing the axial distance may be the reduction of the noise levels generated by the propellers [41]. So, it is found that there is no apparent influence of the axial distance between the propulsors on the PSC values.

CHAPTER 4

EXPERIMENTAL INVESTIGATION OF BLI

In this chapter, an experimental study which is conducted by the author is presented. Similar power saving coefficient (PSC) values as in Chapter 3 are obtained experimentally. First, the overall configuration of the experimental setup and test facilities are described. After that, the design procedure for the experimental setup is explained; and the results of the different configurations which are tested in the wind tunnel are presented and discussed.

4.1 Overview of the Experimental Setup

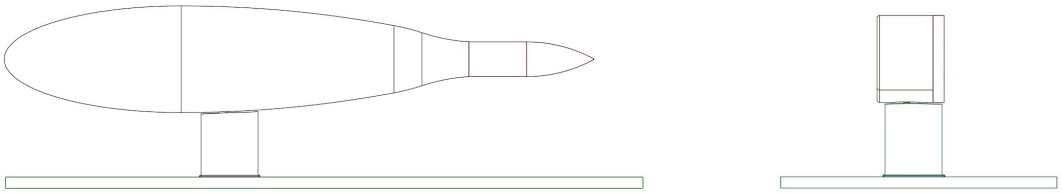

Figure 4.1: Isolated fuselage (left) and free stream propulsor (right) configurations used in the experiment

The experimental setup consists of 3 different configurations.

- Isolated fuselage configuration (Figure 4.1)
- Free stream propulsor configuration (Figure 4.1)
- BLI configuration (Figure 4.2)

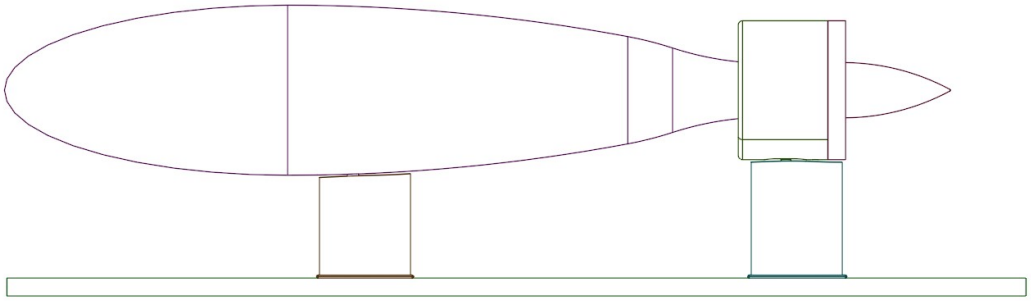

Figure 4.2: BLI configuration used in the experiment

With the first configuration, which is the isolated fuselage configuration, the body drag force is measured by a 6-component load cell. For a fixed free stream velocity (which represents the fixed cruise velocity of an aircraft), this drag force is constant and not affected by the propulsor power setting in conventional configurations, as long as the cruise velocity is fixed. So, fuselage drag and fan thrust are treated separately. The tunnel is operated at $Re = 10^6$ constant Reynolds number (which corresponds to a free stream velocity of 13.1 m/s) to represent this condition. The ambient density and temperature were 1.075 kg/m^3 and 21.85°C, respectively. After measuring the drag of the body, the fan thrust is measured by the same load cell for the different power settings in the free stream propulsor configuration. Then, combining these propulsor thrust values with the constant fuselage drag, the net axial forces for the different throttle settings of the conventional configuration are obtained. Also, the electrical power consumption of the fan is calculated for each thrust value, and they are compared with each net streamwise force like in Chapter 3. Finally, for the BLI configuration, combined drag and thrust values are measured together and net axial forces are obtained for each power setting like the previous configurations.

4.2 Experimantal and Wind Tunnel Facilities

For the experiment, a medium-scale suction type METU RUZGEM C3 open circuit wind tunnel is used [53]. It has an axial fan which is driven by a 45 kW electric motor. It can supply a free stream velocity of up to 25 m/s, with a turbulence

intensity lower than 1%. The tunnel has a 1 m x 1 m square test section which is sufficiently large enough to place the fuselage and fan assembly. Also, it has plexiglass transparent walls to perform any optical flow measurement techniques (Figure 4.3). For a Reynolds number of $80x10^3$, the measured boundary layer thickness of the wind tunnel walls at 6m downstream from the wind tunnel inlet was found as 11 cm. In the experiment, the tunnel is mostly operated at $1x10^6$ Reynolds number. Also, to minimize the risk of being inside the boundary layer of the tunnel walls, the model is placed at the closest distance to the wind tunnel inlet. The minimum distance between the fuselage and the wind tunnel walls is around 14 cm. Even if the model was at the more downstream location of the tunnel, this 14 cm distance is higher than the boundary layer thickness of 11 cm at $Re = 80x10^3$. So, the minimum distance is found acceptable.

Also, the fuselage body used in the experiment has a maximum diameter of 24 cm. When the tunnel cross-section area is considered, the blockage ratio (BR) can be found as:

$$BR = \frac{\pi(0.12m)(0.12m)}{(1m)(1m)} = 4.5\% \tag{4.1}$$

which is an acceptable value.

For the force measurements, ATI gamma SI-130-10 6-component load cell is used. It has a resolution of 1/40 N and can measure up to 130N for the x and y component forces, and a 1/20 N resolution and a limit force of 400 N for the z component [54].

4.3 Production of the Experimental Setup

In this section, the design procedure of the experimental setup is explained. The setup mainly consists of the fuselage, fan and casing, and other structural connection parts.

Figure 4.3: METU RUZGEM C3 wind tunnel which is used in the experiment

4.3.1 Fuselage Body

The design of the body was done by the author. To design an appropriate fuselage body, the critical thing was matching the boundary layer thickness of the body with the propulsor radius. Although they don't have to exactly be the same; the larger ingested part of the fuselage boundary layer, the bigger the benefit is.

In fact, the propulsor had already been selected for the experiment. Due to the counter-rotating feature of the fan, there were not enough commercial fan options on the market. Without the casing, the fan radius is equal to 75 mm. Considering the operating velocities of the C3 wind tunnel, the boundary layer of the fuselage should have at least thick enough to reach a 75 mm radial location from the axis of rotation. So, an iterative process was done to match the boundary layer thickness with the fan radius. The diagram for the iterative process is shown in Figure 4.4.

The boundary layer of the fuselage is checked by a simple 2D CFD simulation. In

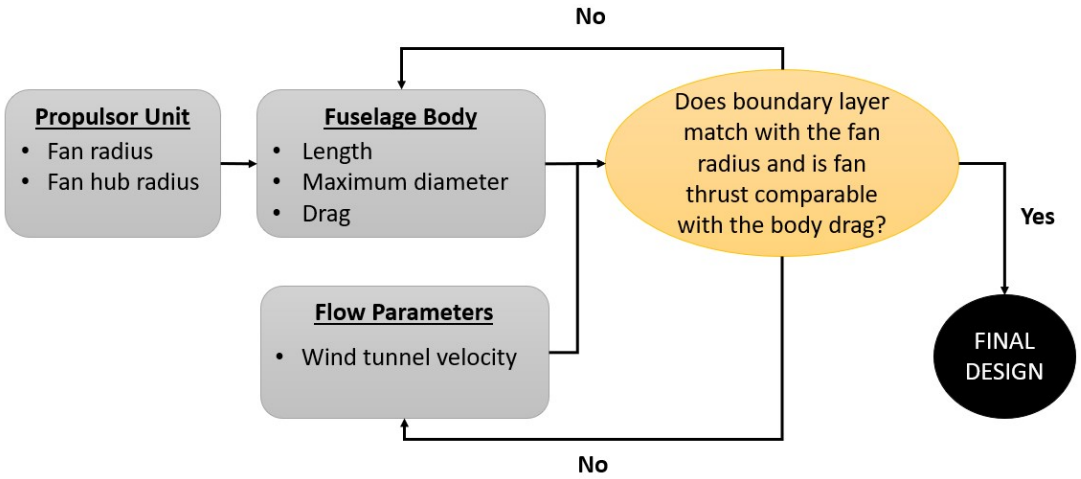

Figure 4.4: Design diagram for determining the fuselage body dimensions

Figure 4.5 and Figure 4.6, the overall dimensions of the CFD setup and mesh are shown.

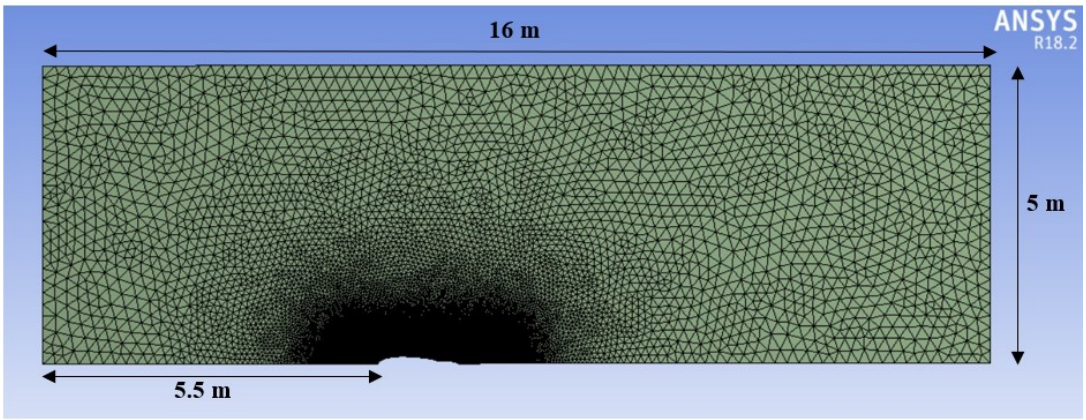

Figure 4.5: Overall look for the 2D CFD setup of the isolated body configuration

The 2D CFD setup is solved with the axisymmetry option in Fluent. So, the axis boundary condition is given to the axis of the body of the revolution. Around 208 000 cells are generated with the ANSYS Meshing tool. Free stream velocity is 11 m/s, which corresponds to the Reynolds number of $1x10^6$ based on the axial length of the body. The maximum y+ value on the fuselage walls is around 0.12, and the iterations are done until the boundary layer velocity profile is converged. The line where the data are taken around the fan location and the boundary layer

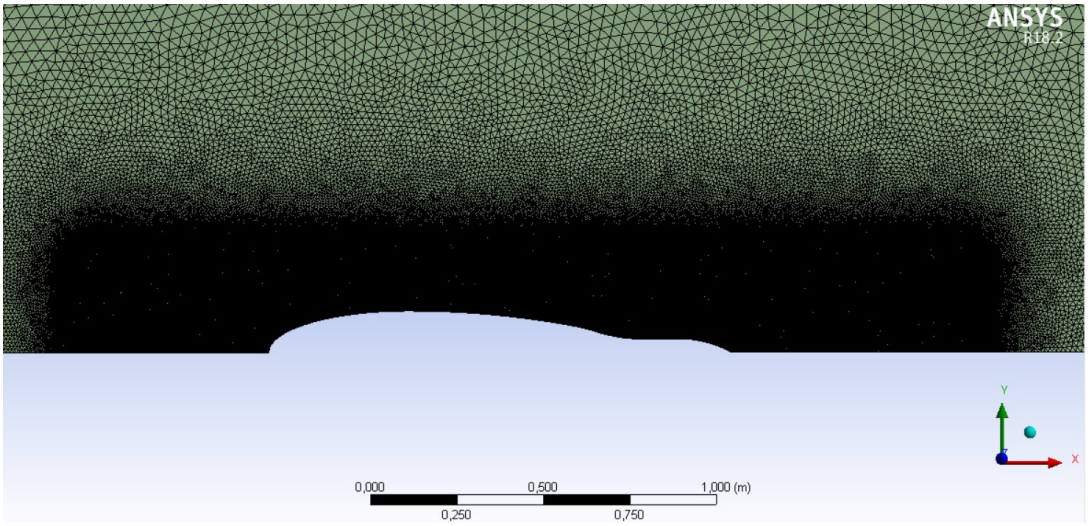

Figure 4.6: 2D mesh around the isolated body

velocity profile on that line are shown in Figures 4.7 and 4.8.

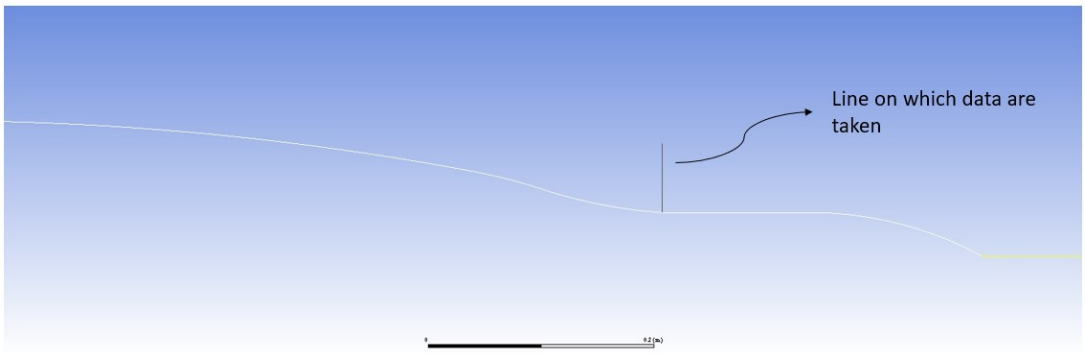

Figure 4.7: The line on which the boundary layer data are taken

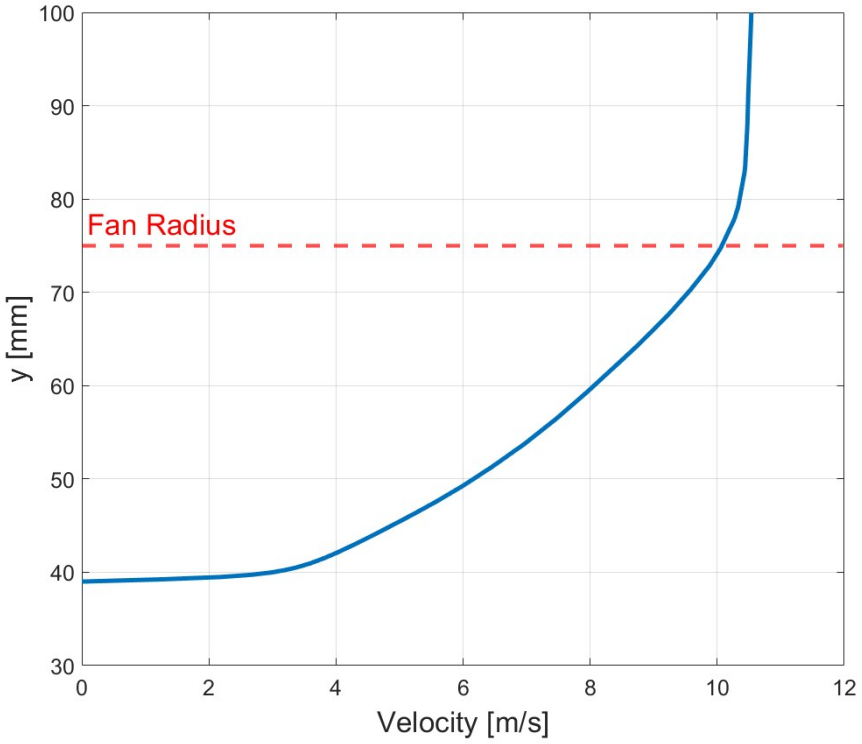

Figure 4.8: Boundary layer velocity profile around the fuselage body

The San Ace 172 counter-rotating fan radius is around 75 mm, which is designated in Figure 4.8. Based on these results, it is concluded that the boundary layer thickness matches the fan radius. Also, the drag of the body is calculated as 0.243 N with 2D CFD results, which is a force low enough for the fan to overcome. The final dimensions of the fuselage body are summarized in Table 4.1.

Table 4.1: Final dimension of the fuselage

Axial Length [m]	**Maximum Diameter [m]**	**Reference (Frontal) Area [m^2]**
1.3	0.24	0.045

After determining the outer shape and dimensions of the fuselage based on the CFD results, the design of the assembly parts and connections is started. In the beginning, it was assumed that the body would be manufactured as a one-piece from wood or aluminum metal. But due to the high manufacturing costs and

expensive prices, it is decided that whole parts could be printed from PLA material by the 3D printer. One of the 3D printers, which is the Raise3D Pro2 Plus 3D printer in the RÜZGEM lab, is used for the whole manufacturing process. For the fuselage body, about 10-15 kg of PLA filament was used for printing, including the trial and error pieces. After removing the support materials, the overall weight of the body remained around 6-7 kg. Since the Raise3D Pro2 Plus 3D printer was not able to print the body as a one-piece due to its dimensions, the body is separated into 4 pieces. After printing them separately, their assembly was done by the male-female tight connection interfaces. The male-female parts of the removable pieces are shown in Figure 4.11.

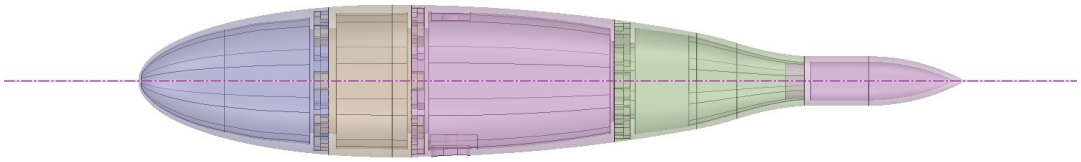

Figure 4.9: Designed fuselage in a CAD environment

The first two parts of the body, which is the leftmost piece in Figure 4.10, were stuck by a powerful Patex sticker. Because there is no need to make these parts removable, the permanent sticking operation is performed. After sticking these pieces, the gaps between their outer surface interface are filled with the filling compound (which is a kind of paste) to have a smooth outer surface. The assembly of the other 3 removable parts is done by the tight male-female connections. When male parts penetrate the female ones, the tight connection of the pieces is obtained when one of the bodies is revolved to fit the housing inside of the female pieces. So, no screws or welding operations are needed. The manufacturing of the whole setup, including the fuselage body, has taken 4 months due to low clearance values between male-female connection parts. So, there were many trial and error pieces.

The connection of the fuselage to the threaded rod, which is shown in Figure 4.10, is done by M16 Hex nuts. Inside the biggest middle piece of the body, there are flat surfaces on top and bottom of the inner surface. On these flat faces, the

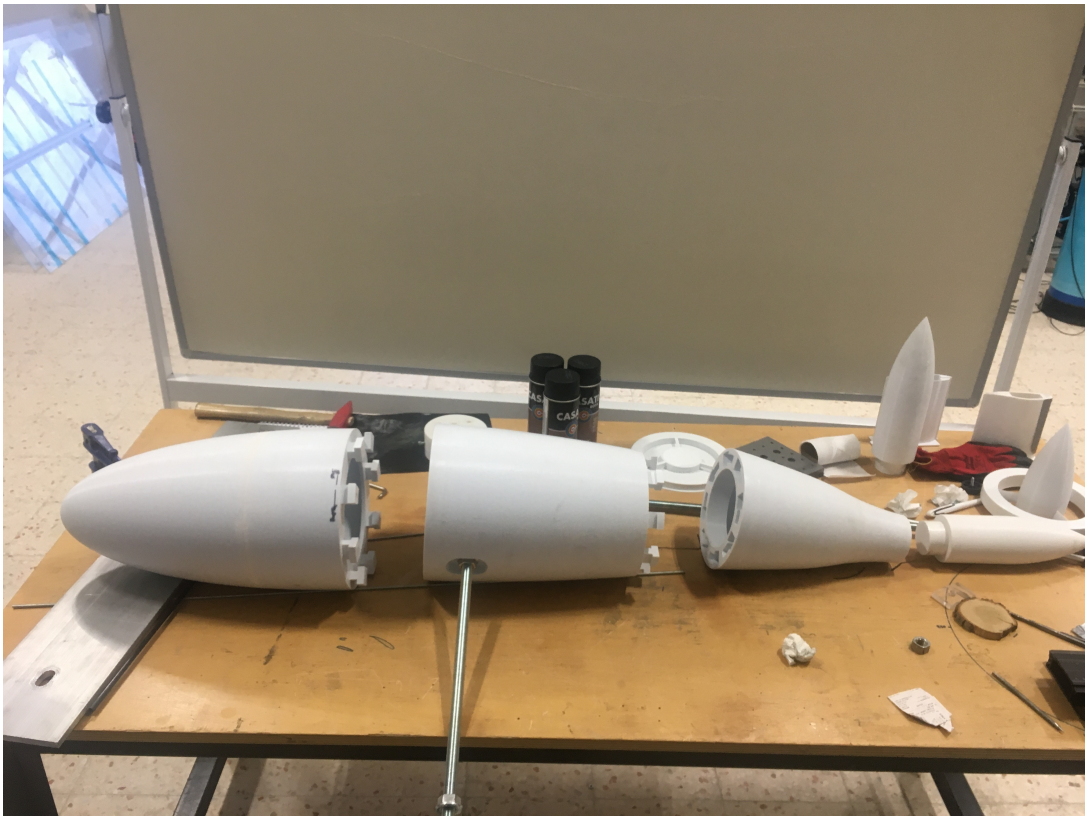

Figure 4.10: Fuselage body in a disassembled form

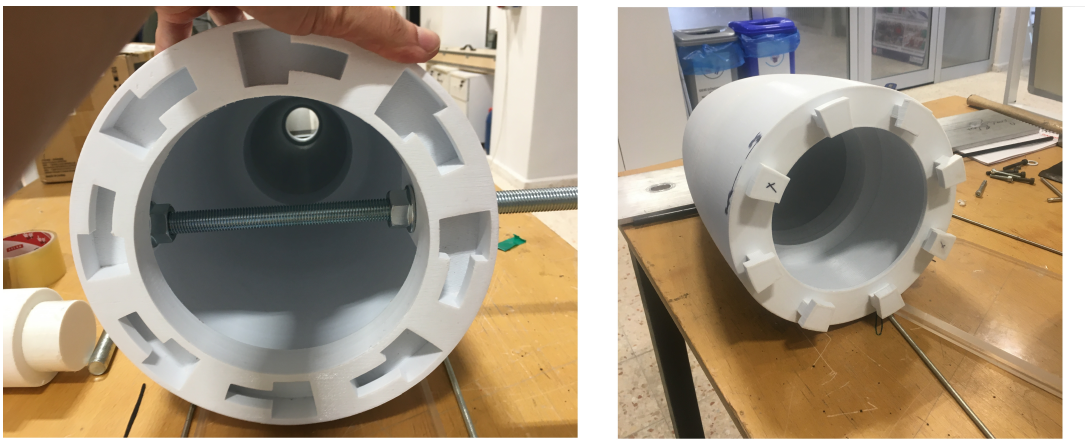

Figure 4.11: Female (left) and male (right) interfaces of the fuselage body

M16 nuts are placed and tightened conversely to compress the body from the inner face upwards and downwards. By doing this contra operation, the aligned connection of the rod with the fuselage body is obtained, in order not to have any

extra unwanted pitching angles. The operation is shown in Figure 4.12.

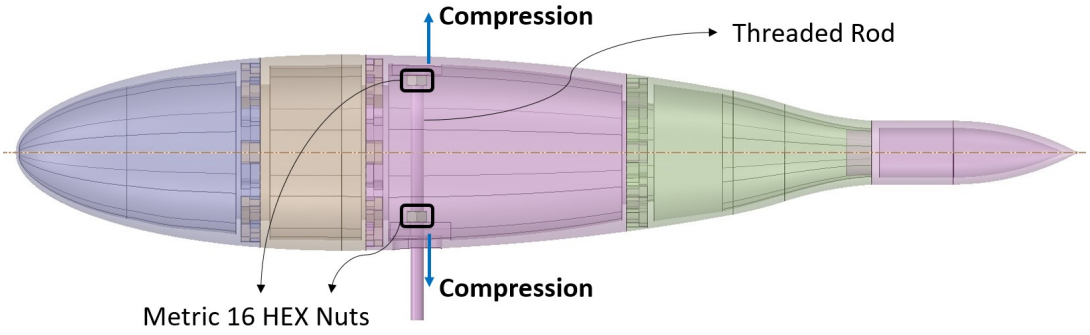

Figure 4.12: Connection of the fuselage body to the threaded rod by the contra operation

4.3.2 Fan and Casing

For the propulsor selection, Sanyo Denki San Ace 172 counter-rotating fan is used [11]. Due to the special counter-rotating feature of the fan, there were not so many options on the market. All components (including the dc motor and casing) are purchased as one piece. The overall look for the fan and its fan curve can be seen in Figure 4.13. So, the only modification for the propulsor was designing an appropriate casing and manufacturing an additional metal holder to attach the fan to a threaded rod. The metal holder piece is manufactured by a laser cutter from sheet metal, and "C" shaped pieces are welded to the square base. After that, inside the small holes on the "C" shaped parts, the metric 4 threaded rods are attached and tightened with small nuts to the fan. The attached metal piece and the fan are shown in Figures 4.14 and 4.15.

In addition, the fan's outer surface which comes with the product as a default could not be used due to not having a smooth shape. So in order to disturb the flow less, an additional casing that has a smooth surface is needed to cover the fan's outer surface as a whole without additional modification. The casing is separated into two pieces, and at the end of it, to attach the tail cone to the fan without an additional strut, similar male-female connection pieces are designed so that the tail cone piece can be removable. With that modification, when changing the

configuration from the isolated propulsor to the BLI, add-on pieces are removed easily. The designed casing and its add-on pieces are shown in Figures 4.16 and 4.17, respectively.

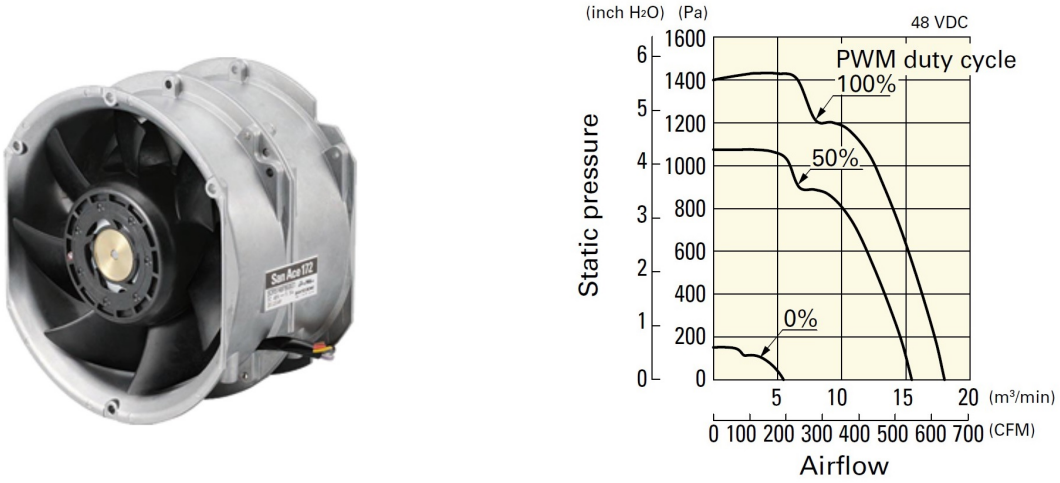

Figure 4.13: San Ace 172 counter-rotating fan and its fan curve [11]

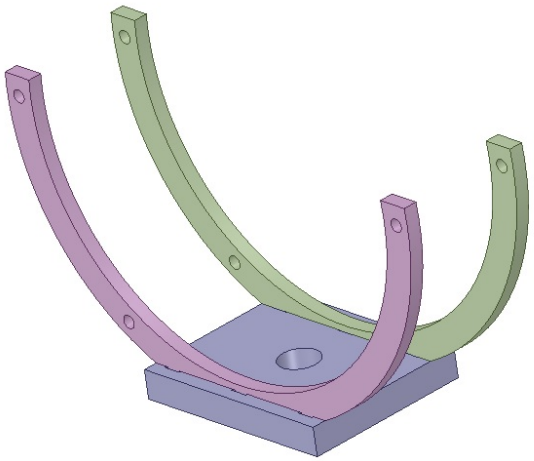

Figure 4.14: Designed metal holder in a CAD environment

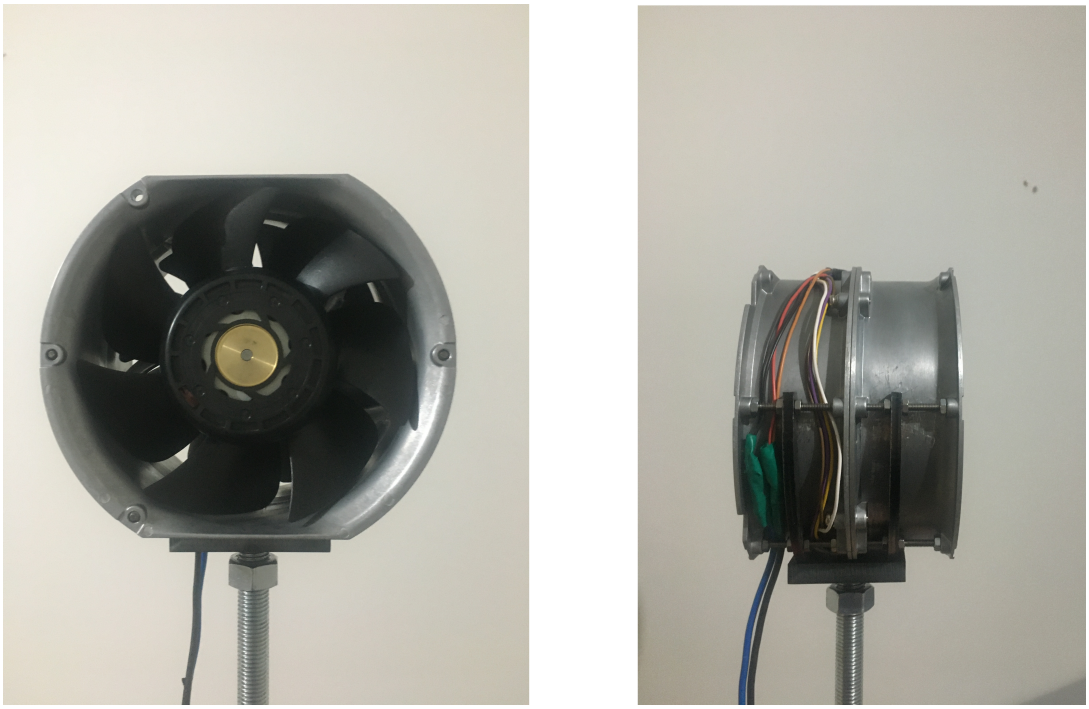

Figure 4.15: Attached metal holder and the fan in front (left) and side (right) view

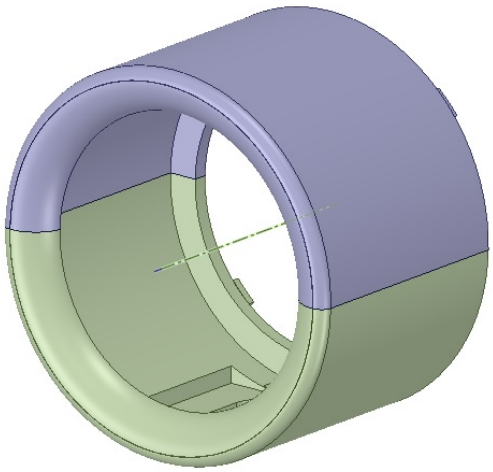

Figure 4.16: Casing in a CAD environment

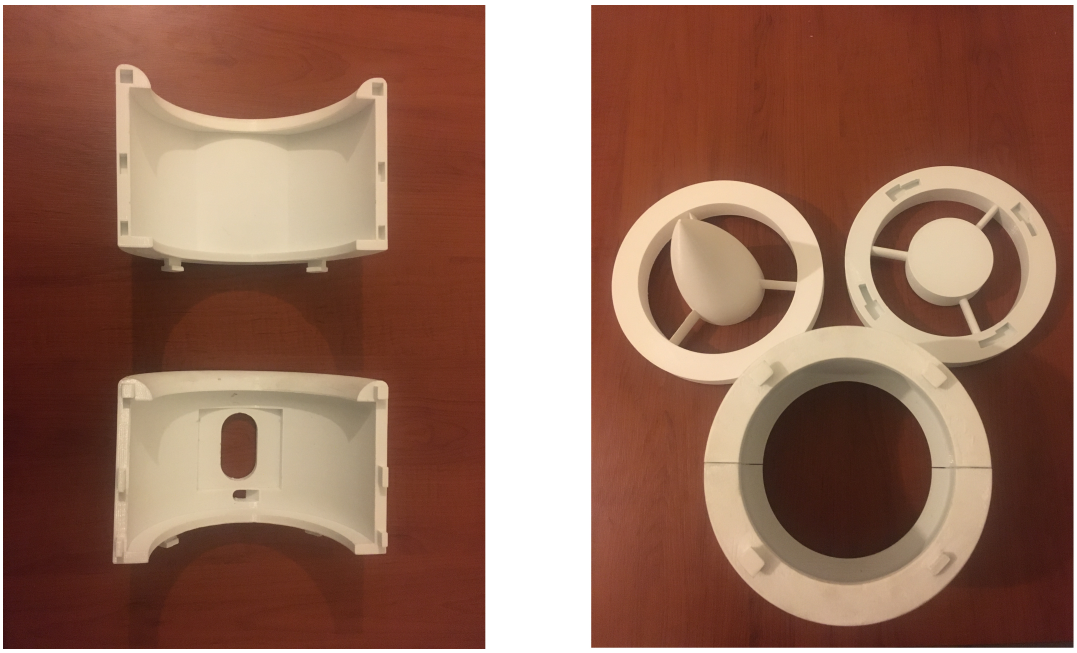

Figure 4.17: Casing in a disassembled form (left) and the casing with add-on pieces (right)

4.3.3 Additional Structural Parts

4.3.3.1 Load Cell Plate

Because there is only one load cell instrument in the lab, some connecting piece is required to attach the rods of both fuselage and the fan to the one load cell. For this purpose, an aluminum plate with a thickness of 10 mm is manufactured from sheet metal by a laser cutter. There are two slots on the plate to attach the fan and the fuselage, and five holes to tighten the load cell to the plate by the screws. The overall look of the plate is shown in Figure 4.18.

4.3.3.2 Airfoil Struts

Since the body and fan are attached to the load cell plate by threaded rods which go into the wind tunnel section, their drag can be measured by the load cell. To eliminate the rods' drag, airfoil-shaped struts that rods can go from inside without

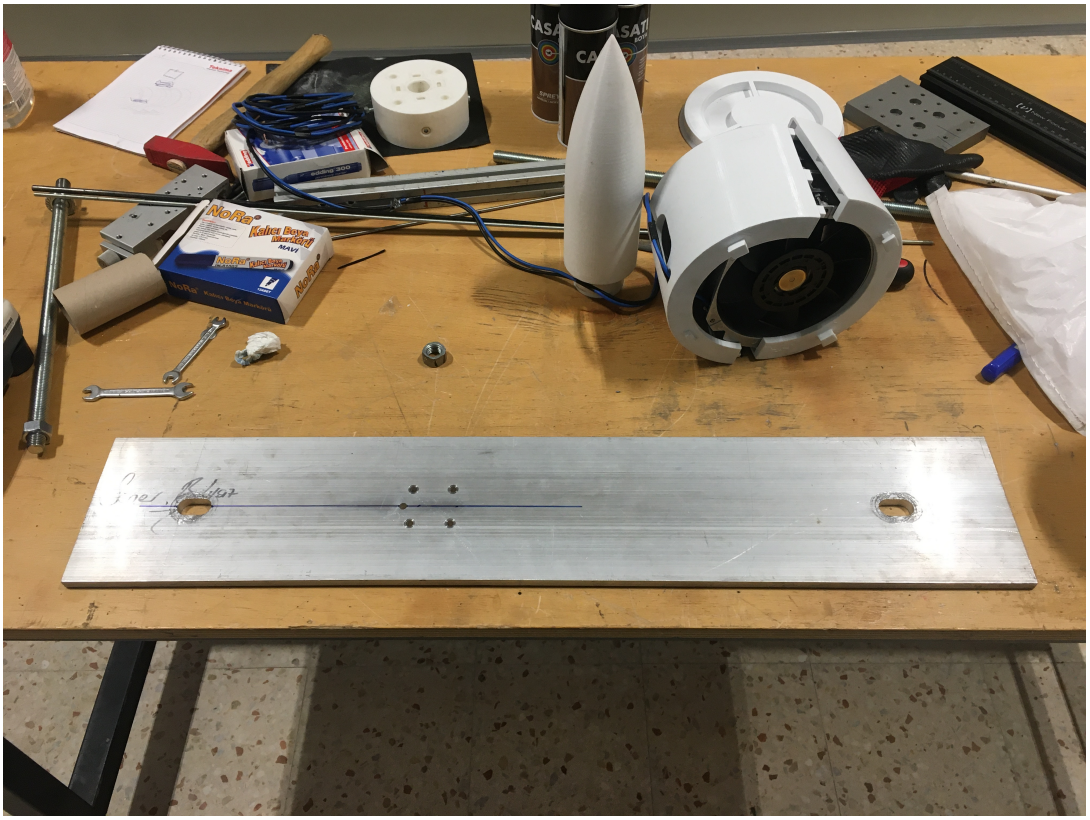

Figure 4.18: Manufactured load cell plate

touching are produced. By printing them as two separate pieces, their implementation into the wind tunnel was easy. There are enough spacings inside the struts so the rods can pass from inside without touching. By this method, the isolation of the rods from the incoming flow is provided. The struts are shown in Figures 4.19 and 4.20.

For the struts, symmetrical 6-digit NACA $65_4 - 023$ and NACA $66_4 - 027$ airfoil profiles are used for the front and aft struts, respectively. Della Corte et al. [55] investigated model-strut interference for the fuselage boundary layer ingestion cases to minimize its effects, and they used a symmetrical NACA 6-digit airfoil. Although they concluded that mirroring the strut or modifying its leading edge can further decrease the interference, it could not be applied to this experiment. But with a sufficient amount of thickness which the threaded rods can easily pass from inside, symmetrical NACA 6-digits are used.

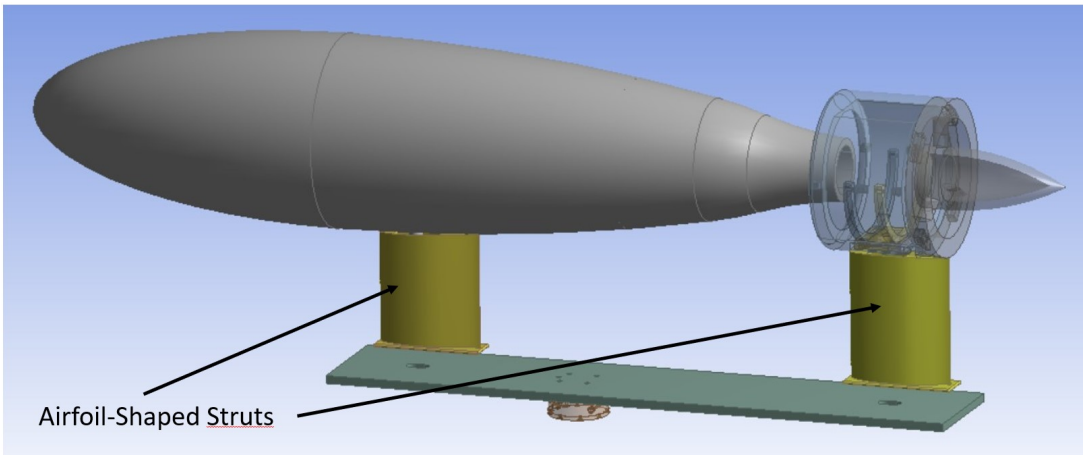

Figure 4.19: Airfoil struts

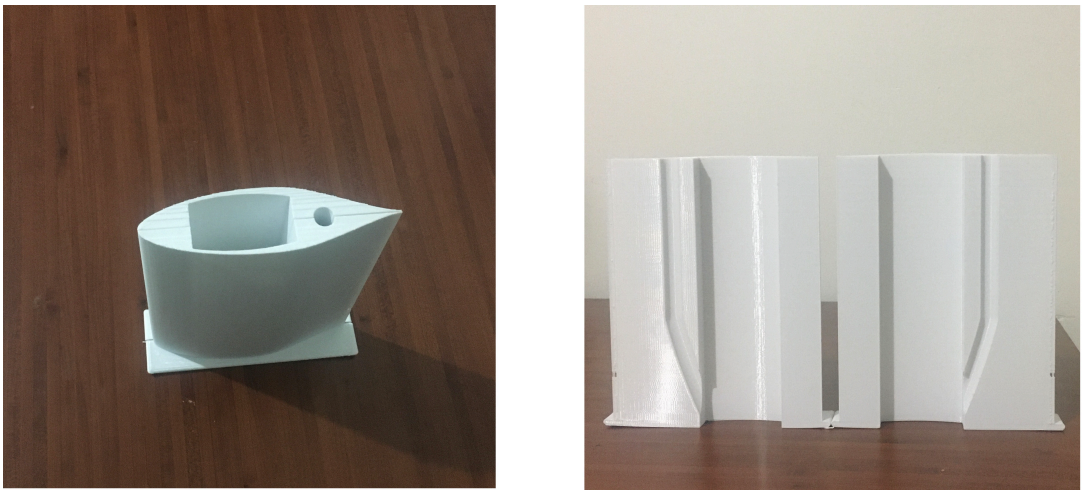

Figure 4.20: Aft strut as one piece (left), and parts separated (right)

4.4 Results

In this section, the experimental results are presented for 3 different configurations; which are isolated body, isolated propulsor, and BLI configurations. For the force components, axis definitions and sign conventions are shown in Figure 4.21.

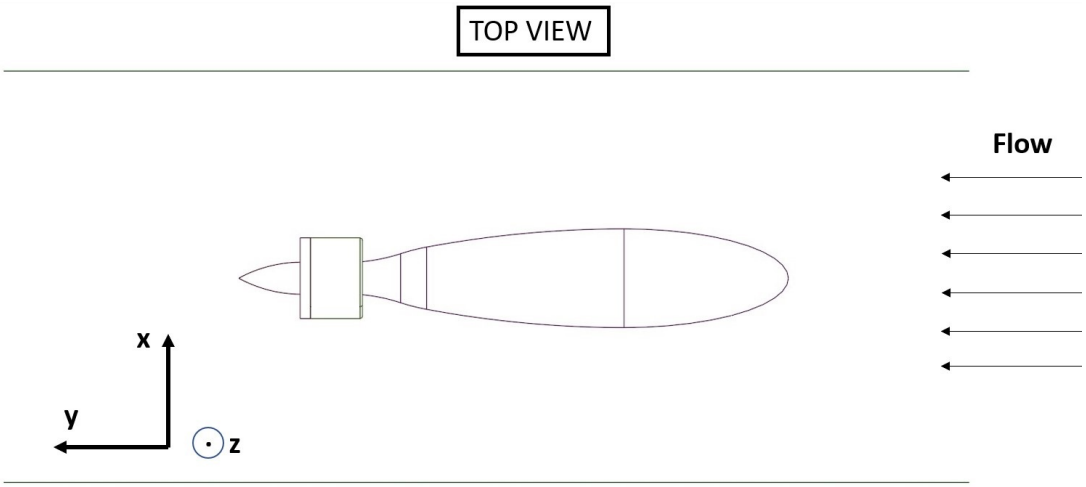

Figure 4.21: Axis definitions of the load cell in the experiment

4.4.1 Isolated Body Configuration

The first part of the experiment was attaching the fuselage to the wind tunnel and observing its drag characteristics. The overall look of the model is shown in Figure 4.22.

Also, to see the effects of the airfoil strut on the body, the same configuration is tested without the airfoil struts. This configuration is shown in Figure 4.23.

The most important task for the experiment is alignment. To align the body with respect to the incoming flow, a laser is used. First, the load cell plate's y-axis is aligned with the center line of the wind tunnel. After that, to minimize the yaw angle of the body, the trailing edge of the body's tail cone is aligned with the incoming laser beam, which passes from the center of the wind tunnel walls. An excessive amount of effort is made to align the body, but due to inevitable imperfections, perfect alignment is not possible.

Without starting the wind tunnel, when everything is attached, the 6-component load cell is biased to make all forces and moments zero. This is important to measure only the additional forces that are applied to the load cell other than the stationary loads. With this option, no calibration operation is needed.

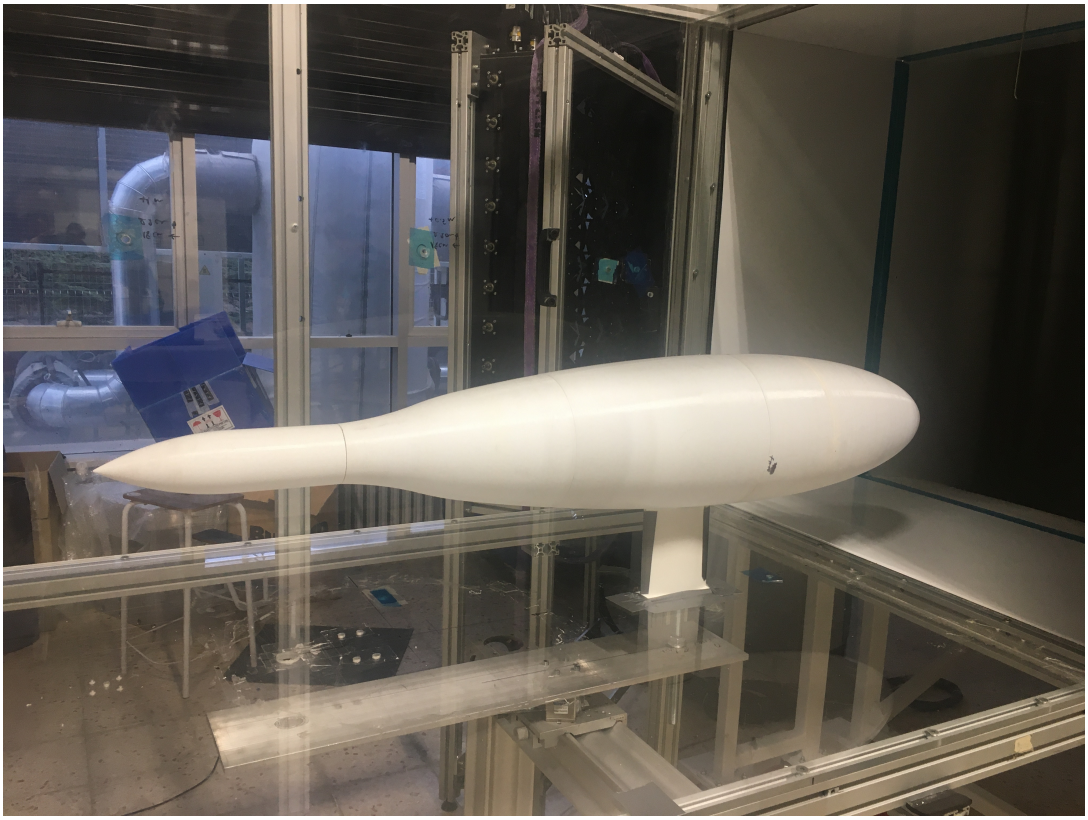

Figure 4.22: The isolated body configuration in the experiment

After biasing the load cell, the body drag is measured at 5 different Reynolds numbers, which are $0.5x10^6$, $0.75x10^6$, $1x10^6$, $1.25x10^6$ and $1.5x10^6$ based on the axial length of the body. The force data are taken at 10kHz frequency with 20 seconds time intervals. The 3 components of the forces with and without the presence of the airfoil struts are shown in Figures 4.25 and 4.26. And also, the drag coefficient plot is shown in Figure 4.27. In these figures, the lengths of the error bars represent the amount of uncertainty (95% confidence level).

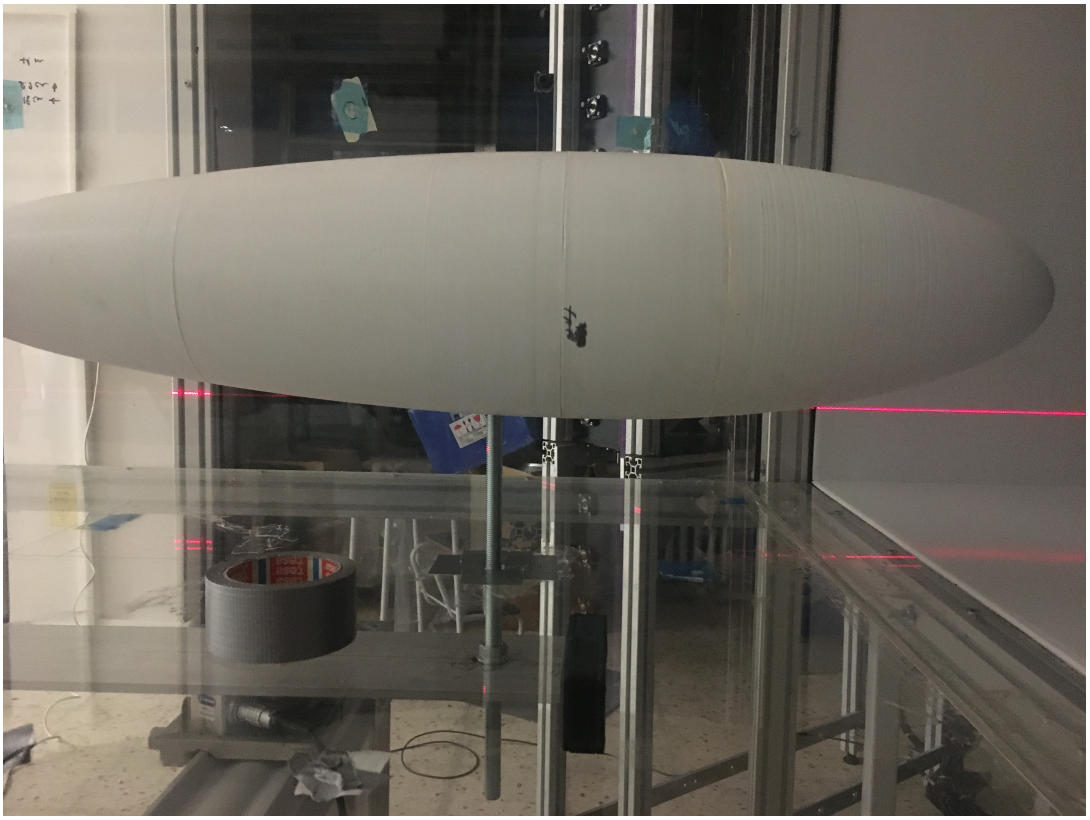

Figure 4.23: The isolated body configuration in experiment without the airfoil struts

When we look at the x-component of the forces, it can be concluded that the body may have a small amount of side slip angle, which is in the clockwise direction along the z-axis. Its side area, rather than the frontal cross-sectional area, is much bigger; which means even any small amount of angular deflection may cause big force changes. A quite much effort was given to aligning the body, but it remained always some amount of uncertainty or error margin in the alignment. Also for the high Reynolds numbers, the model was shaking a little bit, which may cause big fluctuations of the forces for the high velocities.

For the z-component, it seems that the presence of the airfoil strut creates a downward force, which causes the z-component to decrease further. However, without the strut, there is no considerable change. To understand the decreasing behavior of the z-component and to compare the drag force of the body, a 3D CFD analysis with the symmetry boundary condition at a free stream velocity of 11 m/s is

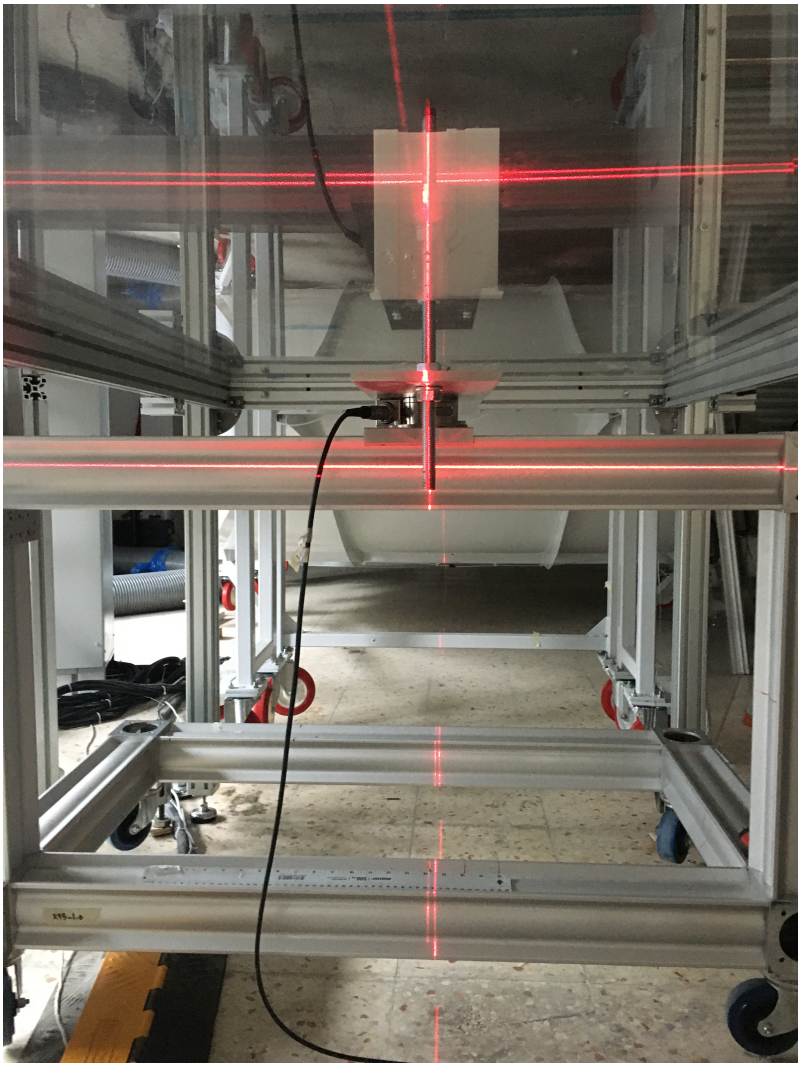

Figure 4.24: Laser alignment of the load cell plate with respect to the wind tunnel center

performed with the same geometry by the presence of the struts and wind tunnel walls. The overall CFD domain and the mesh are shown in Figures 4.28 and 4.29. Also, static pressure contours around the body are generated in Figure 4.30. When we look at the static pressure contours on the fuselage body in that simulation, there is a low-pressure region around the strut, which is at the bottom surface of the body. The air around the symmetric airfoil strut accelerates when passing from its upper and lower surfaces, and decreases the local static pressure around that region. It seems that this local low-pressure region creates a downward force when the free stream velocity is increased. Also, there could be some

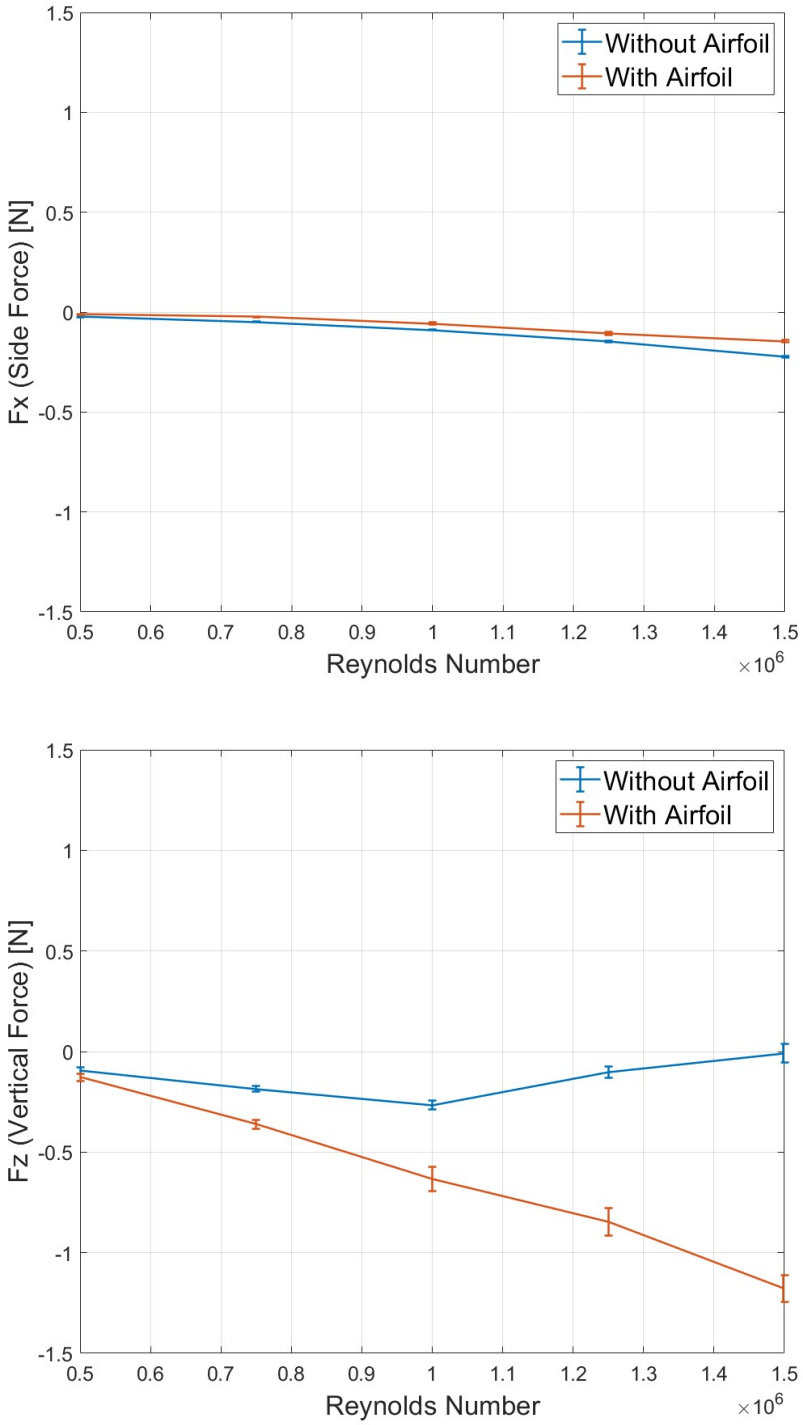

Figure 4.25: The x-component (top) and z-component (bottom) of the net force vs the Reynolds number for the isolated body configuration

pitch-down deflection of the load cell plate due to the weight of the fuselage body; but by looking at the data, the more possible cause of the downward force is the low static pressure region.

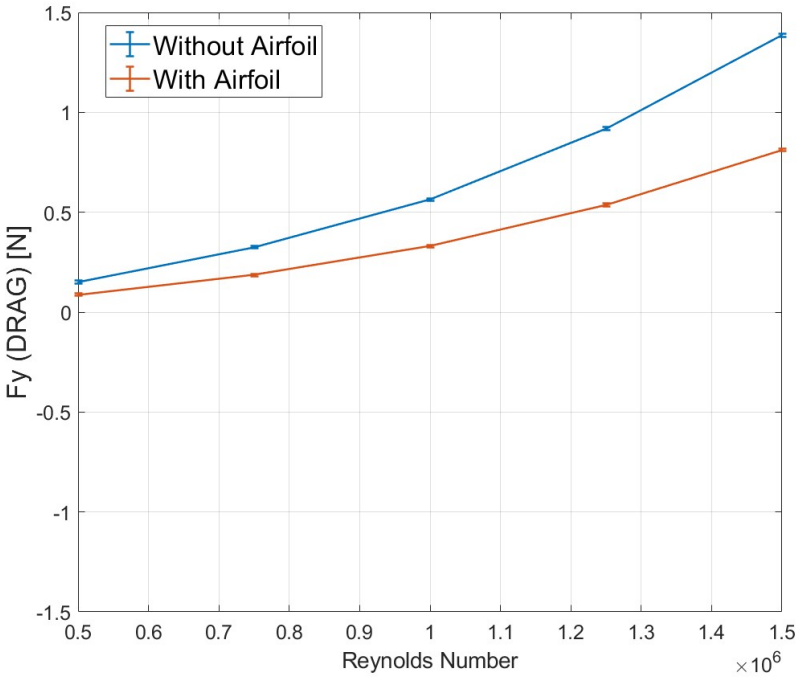

Figure 4.26: The y-component (drag) of the net force vs the Reynolds number for the isolated body configuration

The y-component forces, which are the drag forces, are reasonably increasing with the increasing Reynolds number. It can be seen that airfoil struts have a successful role to eliminate the threaded rod's drag. For the $1.5x10^6$ Reynolds number, with the presence of the struts, it eliminated 2/3 of the drag caused by the rods. At the $1x10^6$ Reynolds number, at which the BLI configuration is tested, the body has 0.328 ∓ 0.006 N drag with the presence of the strut. This gives a drag coefficient of 0.080 ∓ 0.002 for the experiment. To check whether this value is reasonable or not, the drag of the body in the CFD environment is compared to this value. In CFD, 0.346 N drag is obtained for the Reynolds number of $1x10^6$ based on the axial length of the body, which corresponds to a drag coefficient of 0.103. The possible cause for the small difference between the CFD and experimentally determined C_D values can be the difference in turbulence levels. In CFD, rather than assigning

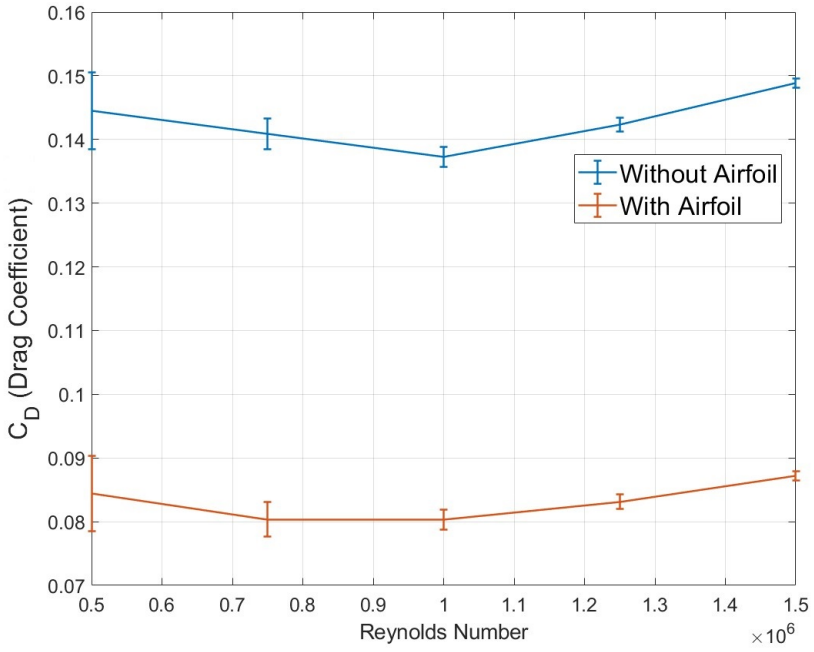

Figure 4.27: The drag coefficient vs the Reynolds number for the isolated body configuration

a laminar zone, a fully turbulent solution is performed, which can overestimate the C_D value. In the experiment, the surface was smooth enough to not cause any excessive turbulence, which makes a possibility to start the flow laminar around the leading edge of the body.

In addition, the boundary layer profile on the line which is shown in Figure 4.7 (around the fan inlet location excluding the strut wake) is also obtained from the 3D CFD solution and compared with the 2D results. The comparison is shown in Figure 4.31. It can be said that the boundary layer thickness is more or less the same as the 2D results. One difference is the overall velocity increase in the 3D CFD results, which can be caused by the small amount of blockage by the wind tunnel walls.

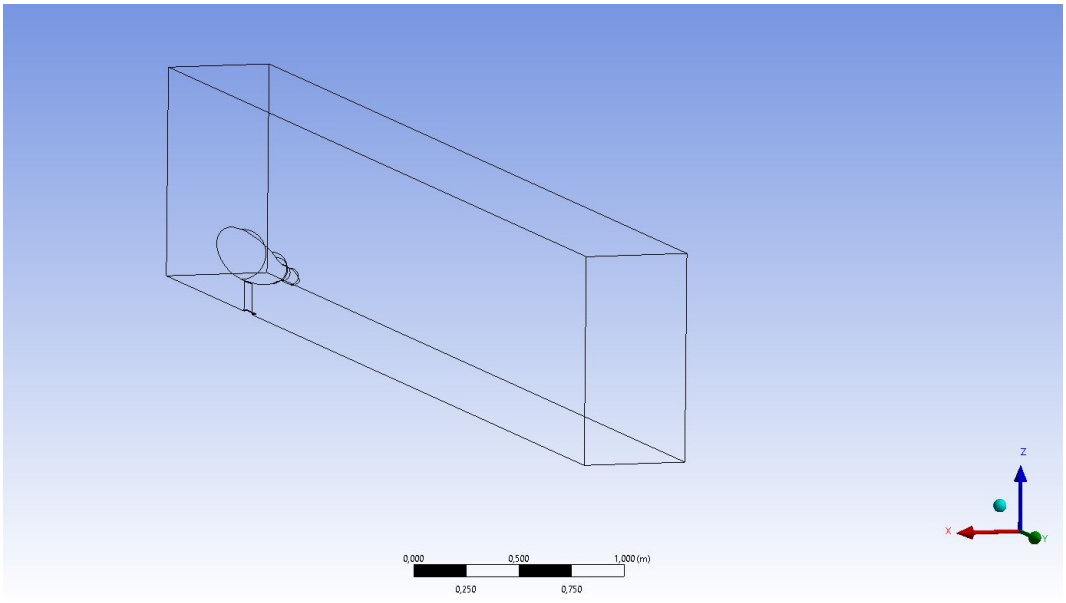

Figure 4.28: CFD domain for the isolated body configuration in the wind tunnel

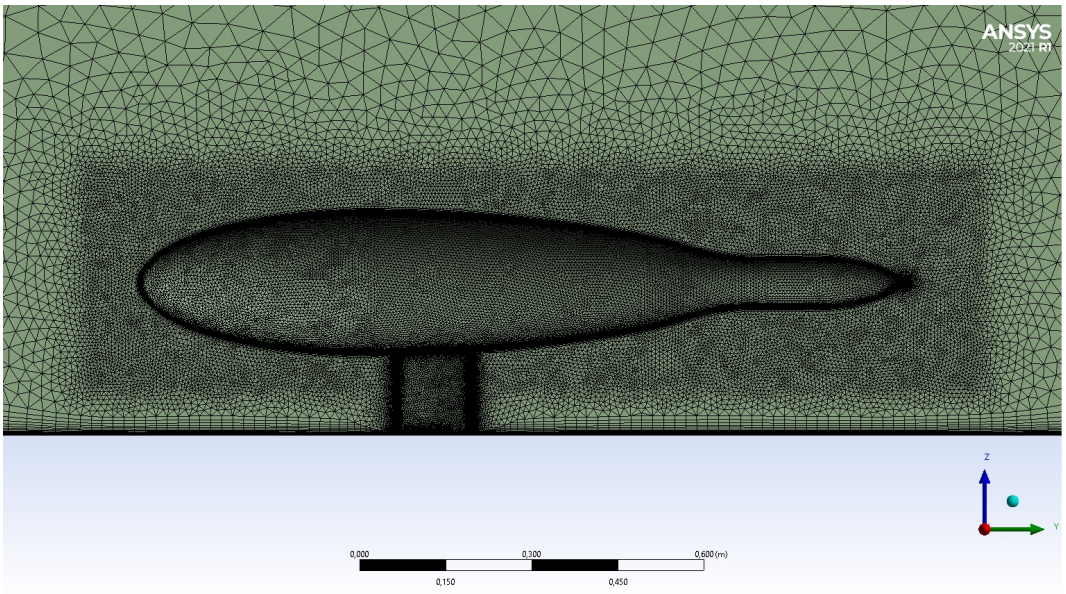

Figure 4.29: The mesh around the body in the wind tunnel model

4.4.2 Isolated Propulsor Configuration

In the isolated propulsor configuration, the fan alone is tested in a constant Reynolds number of $1x10^6$, which corresponds to the free stream velocity of 13.1 m/s. Nor-

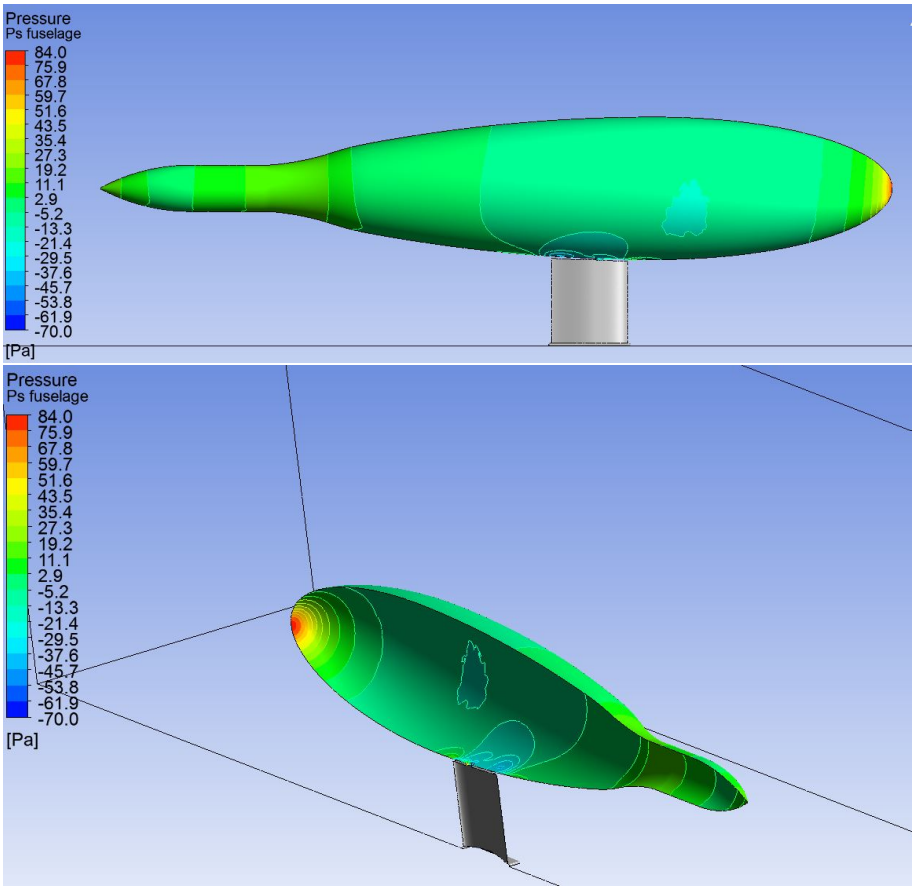

Figure 4.30: The static pressure contours and the low-pressure regions around the strut on the isolated body in CFD

mally, by default, the fan does not have any add-on pieces like the one that is fitted to the aft of the casing (Figure 4.32). When attaching the fan to the BLI configuration, the tail cone of the fuselage just after the fan is connected to the fan casing with male-female connection parts in order not to have one more additional strut for the tail cone (the add-on pieces are shown in Figure 4.17). With this feature, the stator-type of symmetrical NACA 0034 airfoils are used to place the tail cone to the fan downstream and to fit them in the fan center of rotation. So, the stators and the add-on part are considered to be a part of the propulsor. The overall look of the setup can is shown in Figures 4.32 and 4.33.

At a constant free stream velocity, the electrical power given to the fan is increased gradually by the power supply to see the thrust behavior of the fan. The 3 compo-

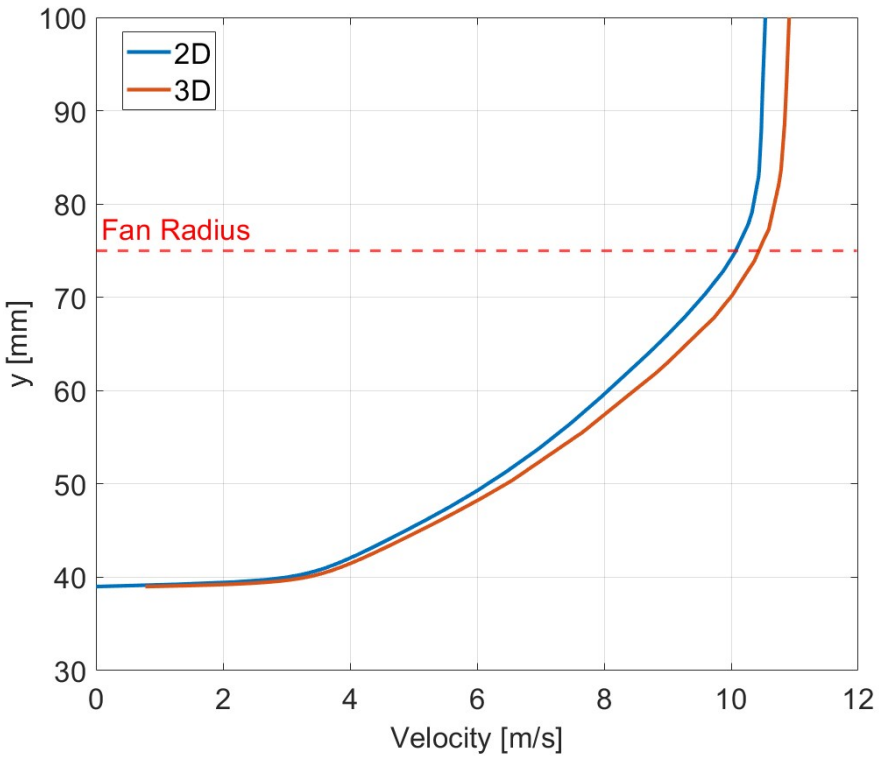

Figure 4.31: 2D and 3D CFD results of the boundary layer profiles of the isolated body configuration around the fan inlet location

nent forces that are read from the load cell are shown in Figures 4.34 and 4.35.

Figure 4.34 shows that the x-component of the force is increasing a little bit, which is again an indication of the misalignment of the fan. But the values are smaller than the streamwise force. When we look at the z-component of the force, however, it can be seen that there is a considerable amount of vertical force component which is in the upwards direction. The possible reason for this may be the deflection of the load cell plate. Because the load cell plate is made from aluminum material, it has a considerable amount of deflection when the fan or the fuselage is attached to it. The fan is behind the load cell, which causes the fan to deflect downwards in such a way that it has a positive pitching angle relative to the flow. That could be the reason for the positive pitching forces, but the values are considerably high when compared to the streamwise force. Also, when the fan power is increased, there is a downward component of the thrust force such that it de-

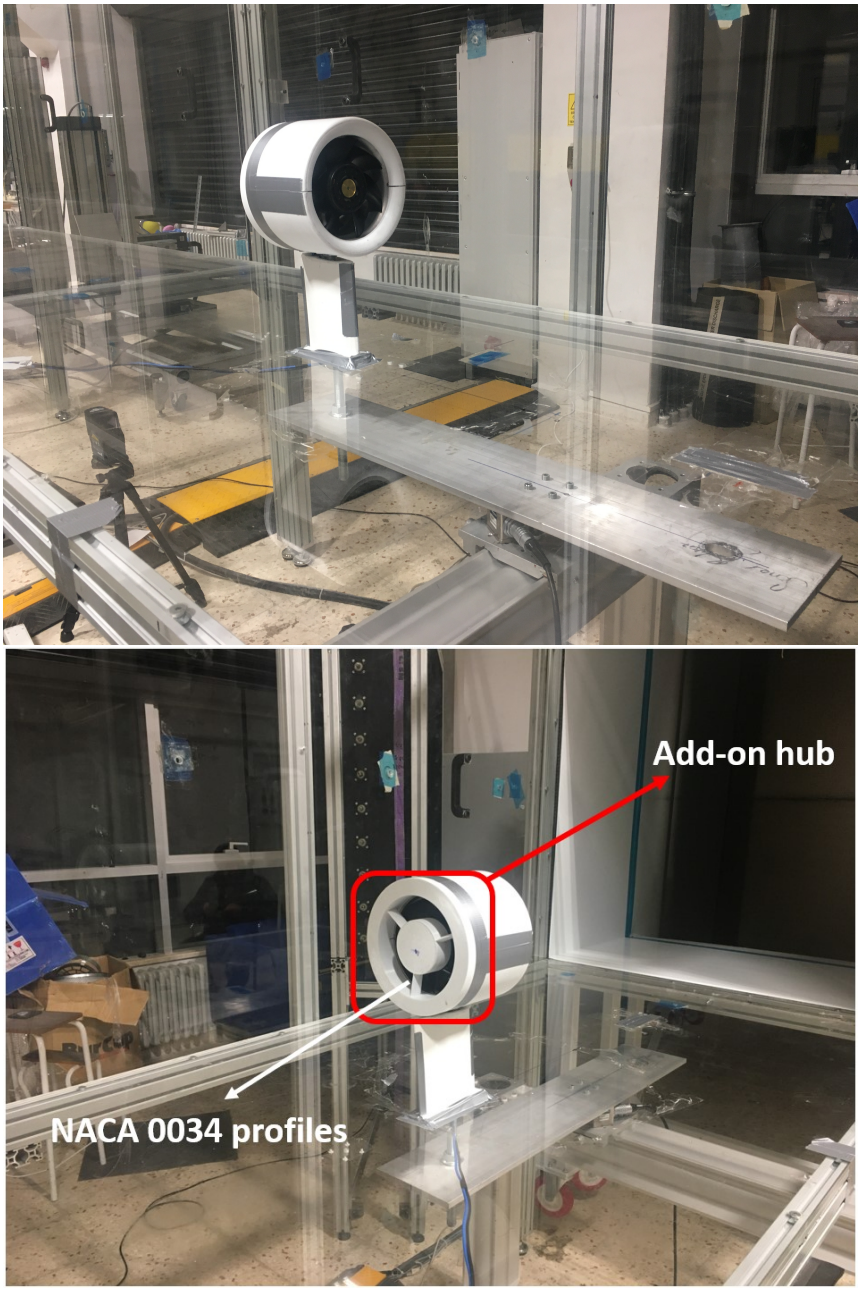

Figure 4.32: The overall look of the isolated propulsor configuration

creases the positive z-direction force component. That may be caused by the fan pitching angle inside the casing. When the fan is attached to the metal holder piece to connect it to the threaded rod, it has some angle which may cause by the threads inside the holder. The threads are not concentric with the rod due to manufacturing errors, so it has some angle when the fan is attached to it. As a whole, due to the load cell plate deflection, the casing may have a positive pitch

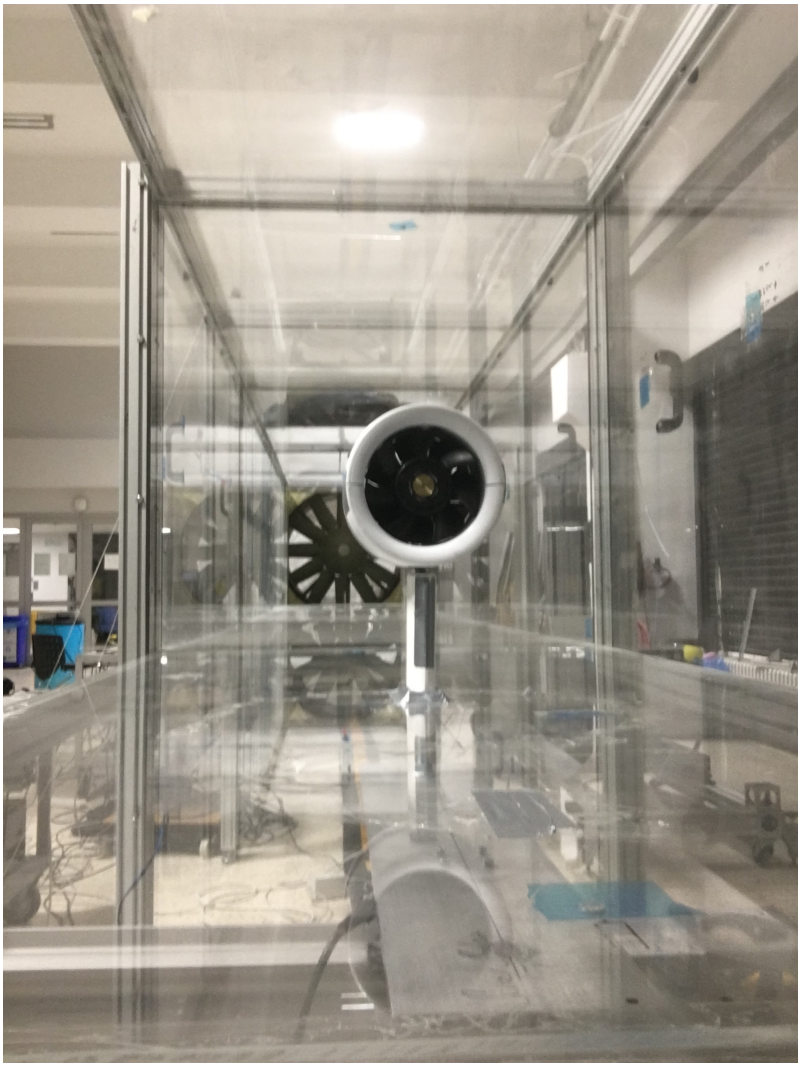

Figure 4.33: The front view of the isolated propulsor configuration

angle; and due to the metal holder piece, the fan inside the casing may have a negative pitching angle.

When we look at the y-component of the net force in Figure 4.35, it can be seen that the fan is not able to produce thrust below the 120 W of electrical power input (the thrust is in the negative y-direction). Because it is normally a ventilation fan, the thrust values are a little bit low, but sufficient enough to overcome the drag of the body, which is 0.328 N. For a free stream velocity of 13.1 m/s, it can produce up to 1-1.5 N of thrust.

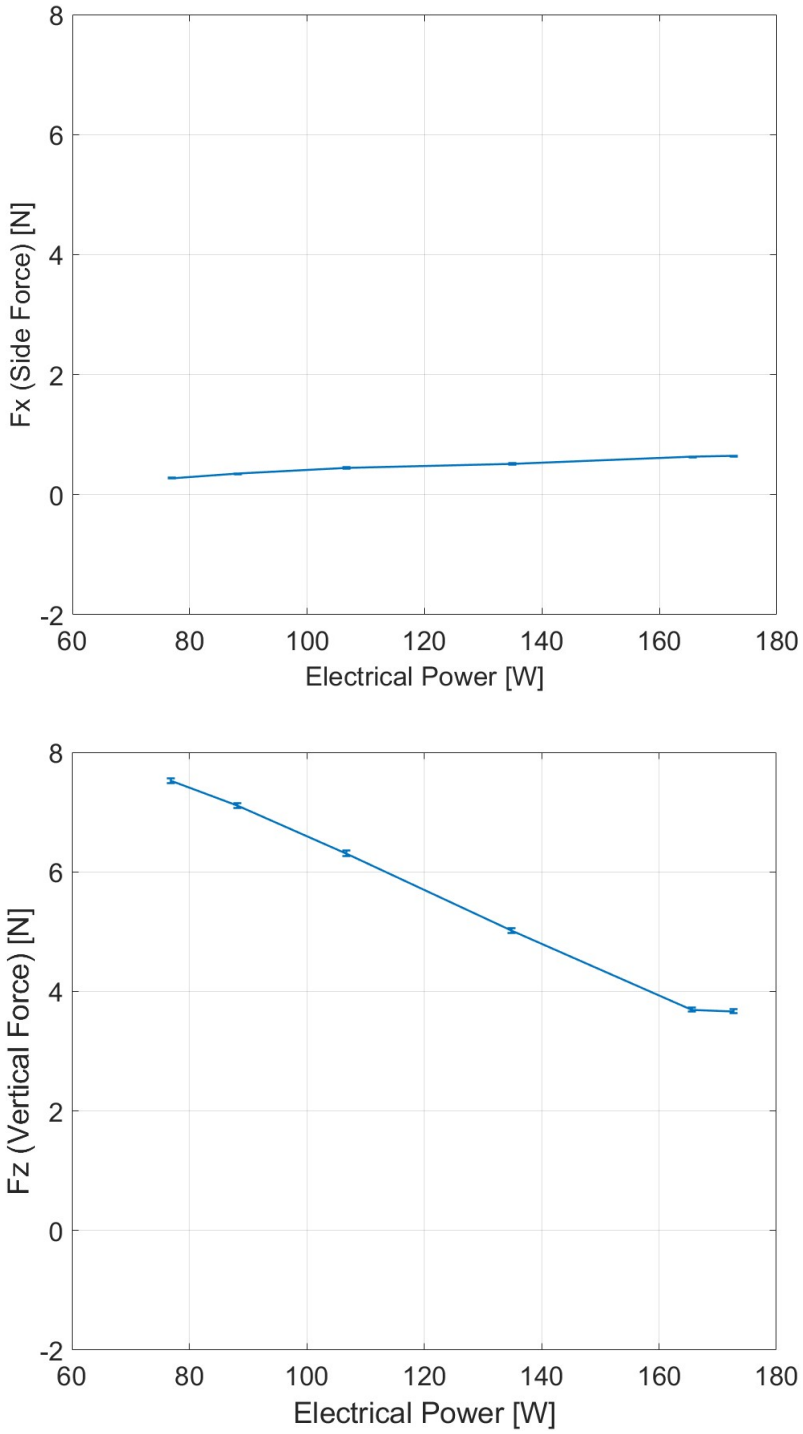

Figure 4.34: The x-component (top) and z-component (bottom) of the net force vs the electrical power input for the isolated propulsor configuration

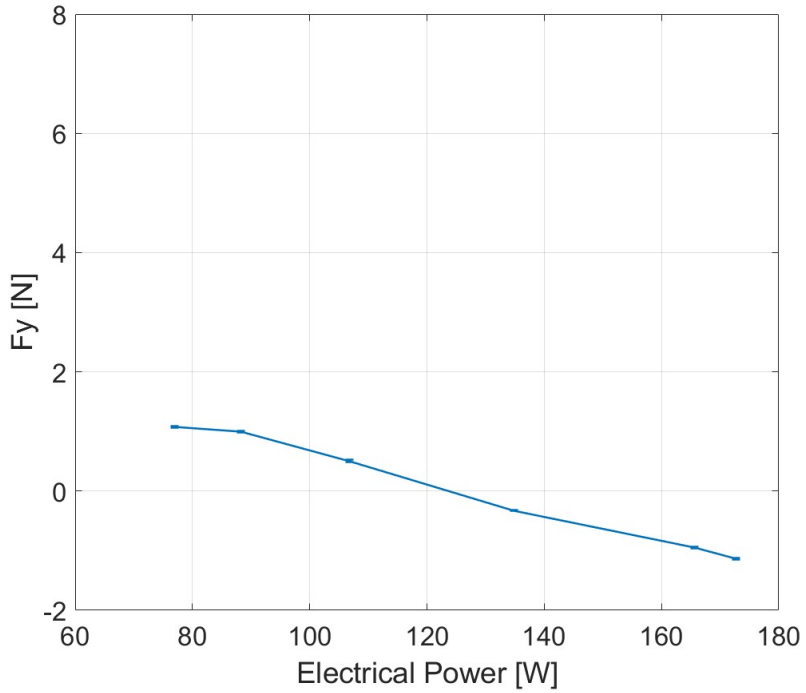

Figure 4.35: The y-component of the net force vs the electrical power input for the isolated propulsor configuration

4.4.3 BLI Configuration

For the BLI configuration, the body is added in front of the fan, and the tail cone add-on piece is added behind the casing by the male-female connection pieces. The fan does not touch the body, which required careful alignment. The overall configuration is shown in Figures 4.36 and 4.37.

For this configuration, the load cell readings for the three components of forces are shown in Figures 4.38 and 4.39.

When we look at the x-component of the net force in Figure 4.38, due to the possible small misalignment, the x force is increasing with the power increment of the fan, but the peak value is around 0.6 N, which is a small value. The trend is almost the same with the isolated propulsor case, with a peak side force of 0.6 N.

The z-component force is again the highest force component among the others.

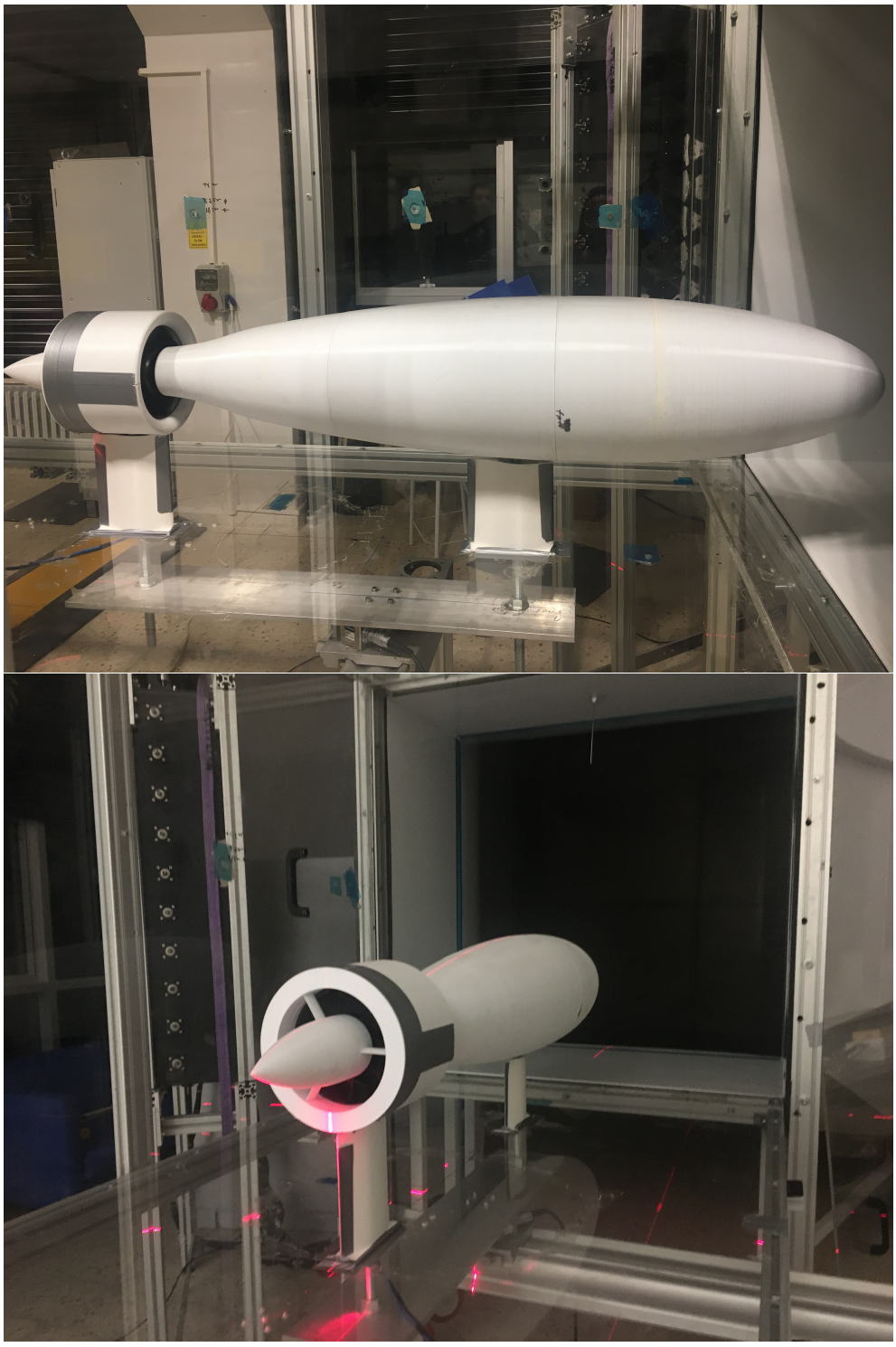

Figure 4.36: The overall look of the BLI configuration

In overall, it is a little bit smaller than the isolated propulsor configuration, but the overall trend is the same. With the electrical power increment to the fan, it

Figure 4.37: The front view of the BLI configuration

decreases to almost half, which brings into the possibility of the negative pitch angle for the fan. The highest force component is also the z-component in the isolated propulsor configuration, which can be explained that the orientation of the fan can cause this high amount of z-component forces in both the isolated propulsor and the BLI configurations.

The y-component in Figure 4.39, has a linear trend. When the power setting is increased, the thrust almost linearly increases. The peak thrust value is almost the same with the isolated propulsor configuration, but with a smaller electrical power input.

With these force and power values, the PSC values for the BLI configuration are calculated. With the 10kHz frequency of data acquisition, approximately 200000 of data are obtained for each power setting. A set of each 50000 data increment, which makes 4 sets of data, is averaged separately and they are fitted on a line. For the non-BLI configuration, the fuselage drag of 0.328 N is subtracted from the

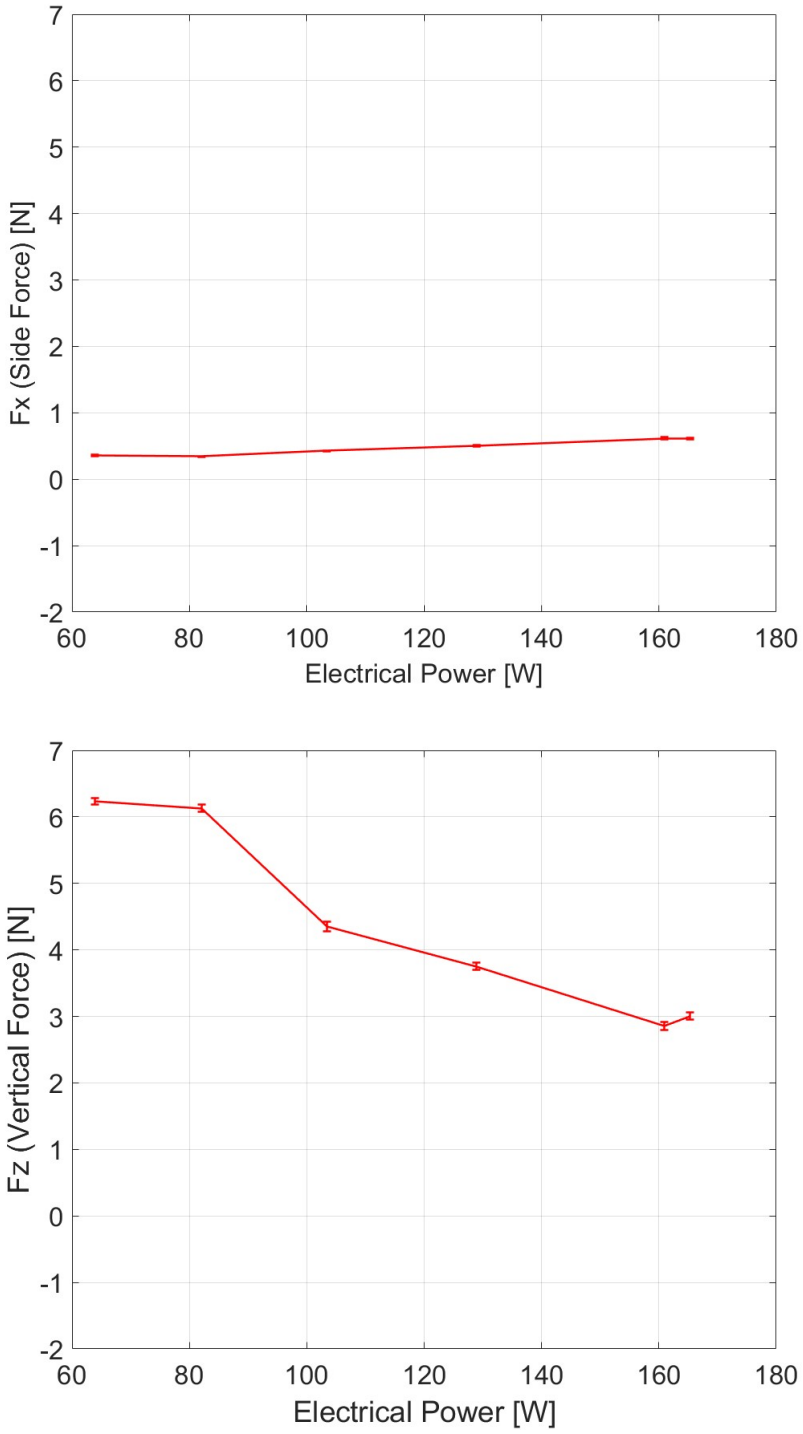

Figure 4.38: The x-component (top) and z-component (bottom) of the net force vs the electrical power input for the BLI configuration

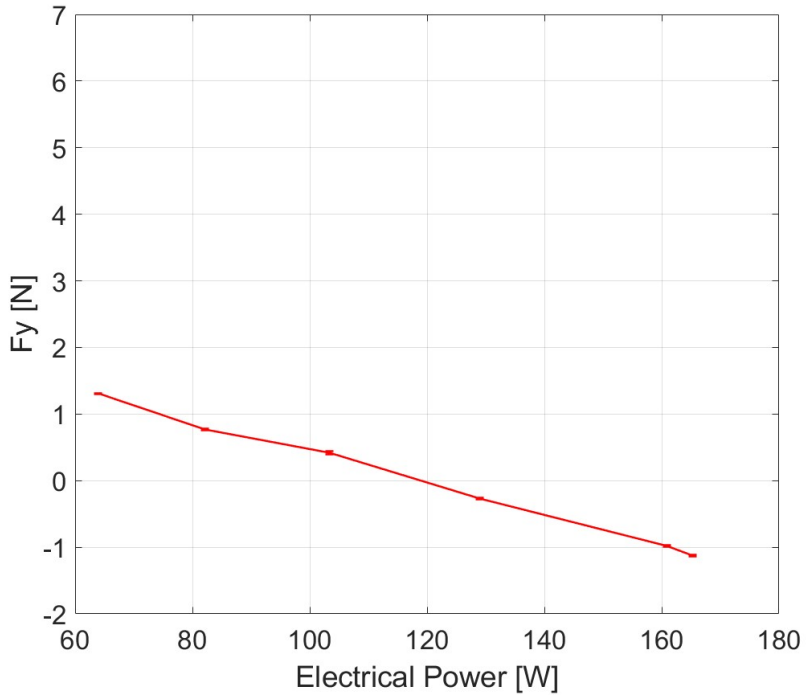

Figure 4.39: The y-component of the net force vs the electrical power input for the BLI configuration

isolated propulsor thrust values, and C_{PE} vs C_{FN} plot is obtained like in Figure 3.20. But rather than the mechanical flow power saving, the electrical power saving of the fan is obtained in the experiment. The PSC values obtained in the experiment are shown in Figure 4.40.

By looking at Figure 4.40, we can conclude that approximately 15.0% of power saving is obtained for the cruise condition in the experiment. The R^2, which are the coefficient of determination values for the line fits, are indicated on the plot. For the net streamwise force coefficient of 0.2, the PSC value can reach up to 20.8%; and for $C_{FN} = -0.2$, it is around 11.5%.

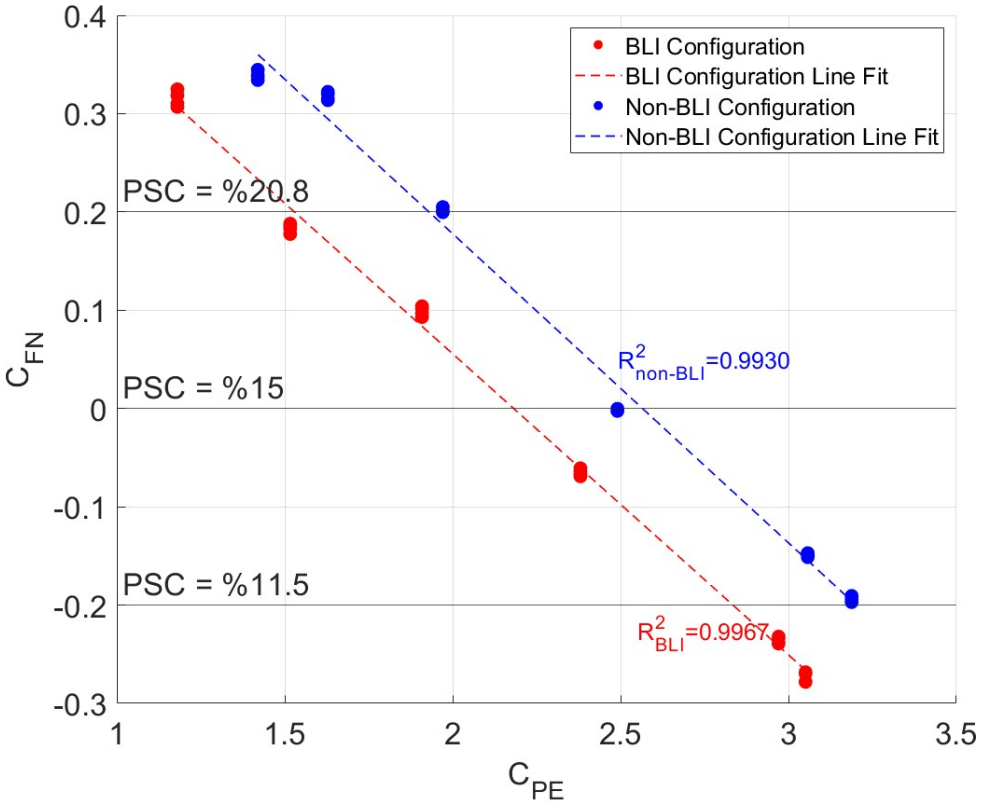

Figure 4.40: C_{PE} vs C_{FN} plots for the BLI and non-BLI configurations in the experiment

CHAPTER 5

CONCLUSION AND FUTURE WORKS

5.1 Conclusion

In this study, both numerical and experimental investigations of a boundary layer ingested propulsion system are performed. Since the geometrical information of the experimental setup was not determined previously, first, a numerical setup is constructed to investigate the concept. After validating the setup by a reference experimental study and calculating the BLI benefit with power saving coefficient (PSC), the counter-rotating propulsor concept is applied to a similar setup. With the numerical investigations, it is found that the counter-rotating BLI concept has a power saving coefficient of around 16.4% for the zero net streamwise force condition. After that, within the BLI configuration, the counter-rotating propulsor concept is compared to the single propulsor concept, and it is found that around 3% power saving is obtained in the counter-rotating one relative to the single one. To check whether the counter-rotating benefit comes from the recovery of the swirl or not, the propulsors are modeled without the swirl generation in the CFD environment. It is found that without the swirl, the single and counter-rotating propulsors consume almost the same power for the same net streamwise force condition, which means there is no additional benefit. Also, the distance between the propulsors in the counter-rotating concept is systematically changed with the same pressure jump and thrust generation values, whether there is a relation between the propulsors' axial distances and PSC values or not. According to the results, PSC values with respect to the single propulsor configuration have not changed considerably, which made a conclusion that there is no relation between the PSC and the propulsor axial distances.

After the numerical investigation, an experimental study is performed by the author. To investigate the PSC and BLI benefits experimentally, a simple body of revolution is designed and manufactured by the author. For the propulsor selection, a commercial counter-rotating ventilation fan is selected. In the experiment, based on the load cell measurement values, around 15% of PSC based on the electrical power is obtained for the zero net streamwise force condition. Although there may be some misalignment problems, looking only at the net streamwise force, the amount of power saving is obvious.

5.2 Future Works

For the numerical part, rather than modeling the propulsors by a 3D Fan zone condition, the actual geometry of the fan blades could be used to represent the physics better. But due to the limited amount of time, the fastest approach is chosen. Also, the control volume boundaries could be taken as a surface rather than a line. In this setup, this could be applicable, but for the other cases, the situation will be different.

For the experimental part, although there are always some imperfections and uncertainty values in the results, the most obvious problem may be the misalignment of the experimental setup. It can be said that the fuselage is more or less aligned properly, but the orientation of the fan could be done better. Also, with the limited amount of time, not enough experiments are performed in the lab. This is another reason for the quality of the results. The possible misalignment problem may also be caused by the load cell plate. Since the load cell plate is sufficiently long, the placement of the fuselage or the fan can cause the plate to deflect considerably. This may change the pitch angles of the both model and the fan. For future experiments, there should be at least two load cells that are attached separately to the fan and the model. Also, there are no flow measurements performed in this study, maybe future studies can perform some PIV or pressure measurements to validate the boundary layer thickness and calculate the other power components in the flow. Also, if there would be enough time, the comparison of the single and counter-rotating fan concepts would be done. In future studies, PSC values with

respect to the single propulsor concept can be compared by just again looking at the electrical power saving. Also, by PIV measurements, the recovery of the swirl (if it is) can be quantified and visualized.

APPENDIX A

DEFINITIONS FOR THE OTHER POWER COMPONENTS OF THE POWER BALANCE EQUATION

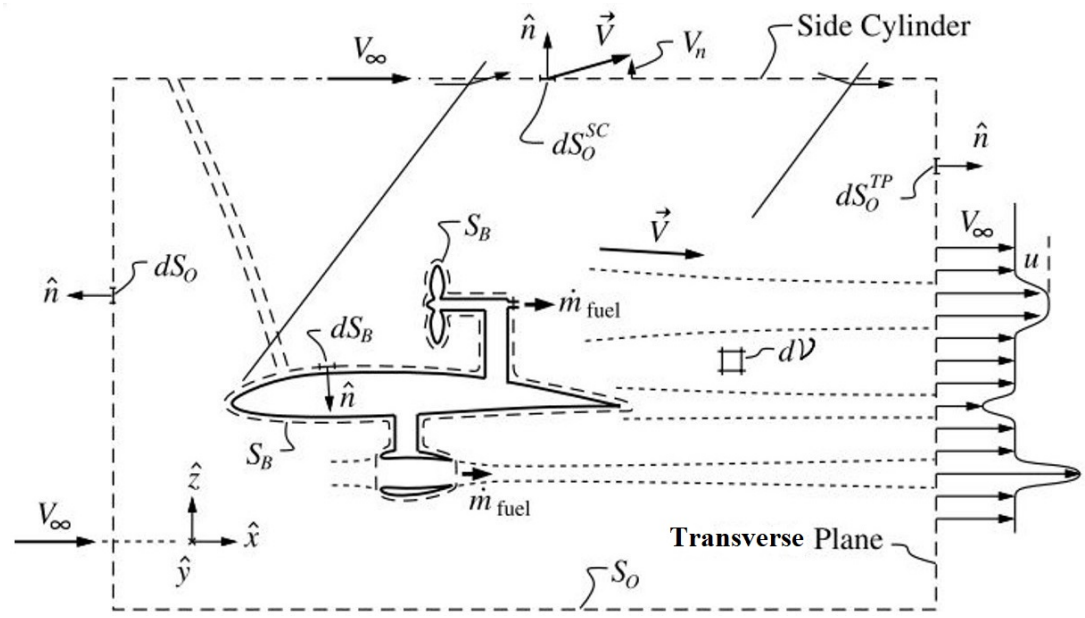

Figure A.1: Control volume around an aircraft for the power balance analysis [8]

The application of the power conservation for the control volume which is shown in Figure A.1 gives the following equality:

$$\underbrace{P_S + P_V + P_K}_{\Sigma P_{input}} = \underbrace{\dot{W}h + \dot{E}_a + \dot{E}_v + \dot{E}_p + \dot{E}_{wave}}_{\Sigma P_{outflow}} + \underbrace{\Phi_{total}}_{\Sigma P_{dissipation}} \tag{A.1}$$

If we consider power input terms, P_S represents the net propulsor shaft power imparted into the control volume, and can be written as:

$$P_S = \oiint [-(p - p_\infty) \cdot \hat{n} + \bar{\bar{\tau}}] \cdot \vec{V} dS_B \tag{A.2}$$

This is the integrated force times velocity (power) on the whole moving surfaces of the control volume. This power addition is considered positive for the work-doing devices to the flow such as compressors or fans, and negative for turbines. For this component to be non-zero, the surfaces of the control volume should cover the moving blades.

The P_V represents the pressure-volume power and can be written as:

$$P_V = \iiint (p - p_\infty) \nabla \cdot \vec{V} d\forall \tag{A.3}$$

This term includes the total power done on the control volume due to compressibility or volume change effects. It is non-zero for the flows especially if there is heat addition or extraction from the system at a different pressure than the free stream, or if there are shock or expansion waves. For the incompressible flows, since $\nabla \cdot \vec{V}$ will be zero, this term can be neglected.

The components of the power dissipation terms can be decomposed as follows:

$$\Phi_{total} = \Phi_{surface} + \Phi_{wake} + \Phi_{jet} + \Phi_{vortex} + \Phi_{wave} \tag{A.4}$$

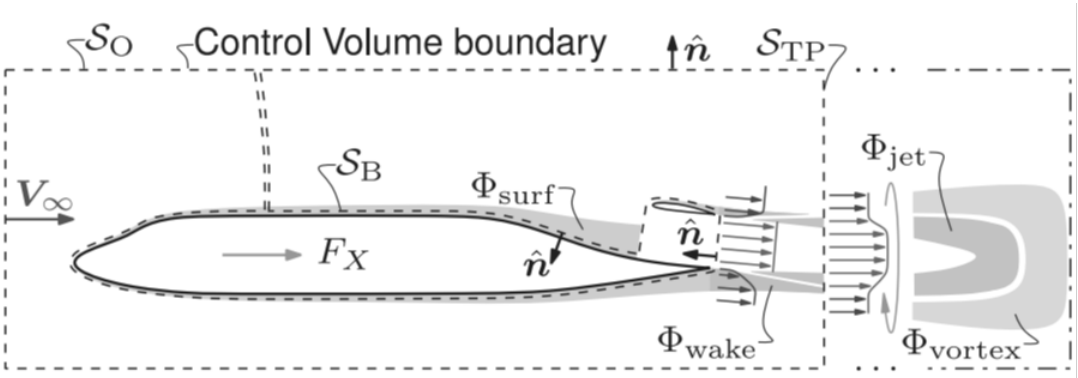

Figure A.2: Power dissipation components inside the control volume for a BLI configuration [12]

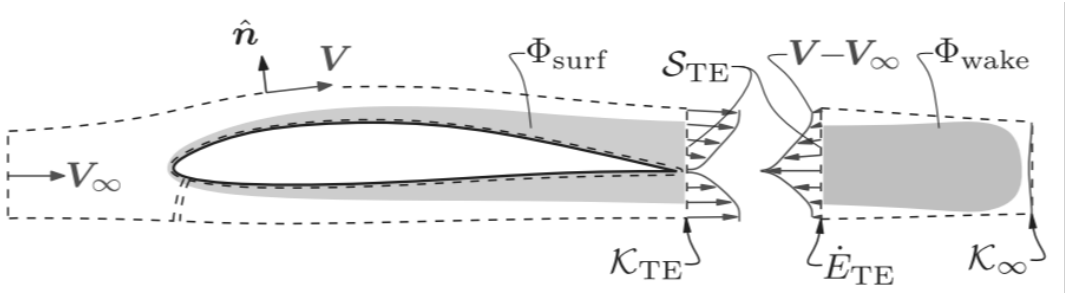

Figure A.3: Surface and wake dissipation components for an isolated body [12]

Among the dissipation components, surface dissipation, $\Phi_{surface}$, corresponds to the dissipated rate of kinetic energy due to the shear layer on the airframe. For an isolated body, it corresponds to the kinetic energy defect up to the trailing edge of the body.

$$\Phi_{surface} = \iint \frac{1}{2}(V_\infty^2 - V_{TE}^2)\rho \vec{V}_{TE} \cdot \hat{n} dS_{TE} \tag{A.5}$$

Wake dissipation, on the other hand, is the rate of kinetic energy defect after the trailing edge of the body. If we only consider an isolated body exposed to the free stream velocity (Like in Figure A.3), wake dissipation is the remaining portion of the kinetic energy rate after the surface dissipation on the airframe. In other words, the whole remaining kinetic energy after the airframe should be dissipated, and it is the wake dissipation component.

Jet dissipation, Φ_{jet}, is somehow similar to the wake dissipation, except that the power outflow terms after the formation of the jet behind the propulsor dissipate in the jet.

Power dissipation due to trailing vortices, Φ_{vortex}, as the name implies; represents the power loss due to the vortex formation downstream of the body. If the body is a 3-dimensional lift-generating device like a winged aircraft, some trailing vortices occur near the wing tips. These vortices result in extra induced drag, which can be considered as an additional power dissipation term. So, this dissipation is the vortex dissipation, Φ_{vortex}, and it is equal to the induced drag power generated by the trailing vortices downstream of the wings:

$$\Phi_{vortex} = D_i V_\infty \tag{A.6}$$

Finally, wave dissipation, Φ_{wave}, is the power dissipation due to the formation of shock waves if the aircrafts speed is near or above the sonic conditions.

As the conservation of energy implies, whole power outflow terms leaving the control volume outlet defined before should be dissipated and transformed to these dissipation components, as all the flow properties reach the free stream conditions.

A.1 Illustrative Examples

A.1.1 Isolated Body

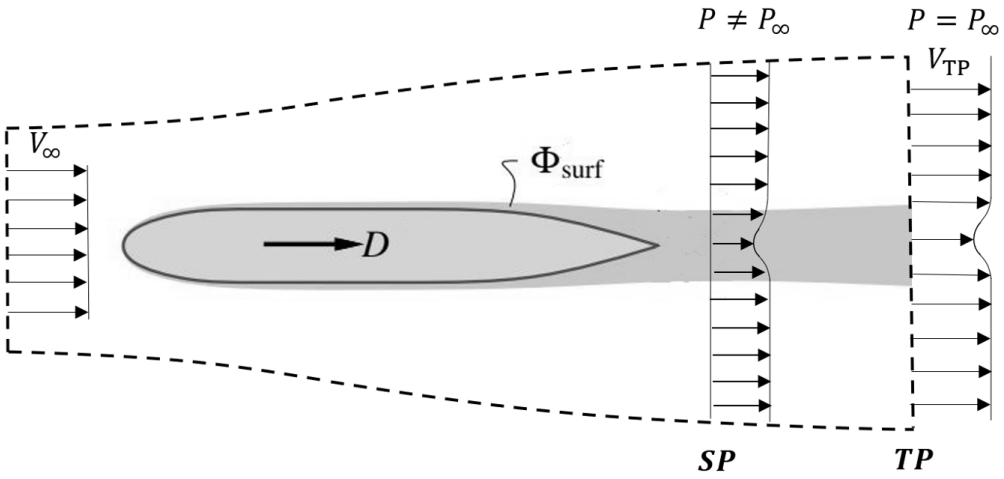

Figure A.4: Control volume around an isolated body [7]

Lets write a power balance equation around this control volume above. First, we can differentiate the power input and output terms around this control volume. If we write the components, we have:

$$\Sigma P_{input} = DV_\infty \tag{A.7}$$

$$\Sigma P_{output} = \underbrace{\dot{E}_{a,TP} + \dot{E}_{v,TP}}_{\Sigma P_{outflow}} + \underbrace{\Phi_{surface} + \Phi_{wake}}_{\Phi_{total}=\Sigma P_{dissipation}} \tag{A.8}$$

Here drag power (DV_∞), which is the total drag on the body multiplied by the free stream velocity, is considered as a power input because to sustain the body on the incoming free stream velocity, there should be some force applied to the body which is equal to the total body drag.

If we consider the power outflow terms just after the Transverse plane at which the static pressure recovers the free stream pressure, they consist of the axial and transverse kinetic energy deposition rates ($\dot{E}_{a,TP}$ and $\dot{E}_{v,TP}$). These are the total rate of kinetic energy deposited at the Transverse plane. After the Transverse plane, all these power outflow terms should be dissipated until the flow reaches the free stream conditions.

If we consider the power dissipation terms within the control volume up to the Transverse plane, the power is dissipated on the surface of the body due to the shear layer by $\Phi_{surface}$. After the trailing edge, another component of the dissipation occurs due to wake mixing by the wake dissipation, Φ_{wake}. Normally, if this body is considered to be an aircraft, there should be an additional power dissipation term, which is Φ_{vortex}, due to trailing vortices downstream of the body. In the context of this study, it is omitted due to the absence of induced drag.

In the end, as the conservation of energy dictates, the whole power input should be equal to the power output terms inside the control volume:

$$DV_\infty = \dot{E}_{a,TP} + \dot{E}_{v,TP} + \Phi_{CV} \tag{A.9}$$

In Figure A.5, the change in the power components can be seen inside the flow field. Note that $\dot{E}_p$ (pressure-work outflow rate) is apparent in the figure and non-zero in the wake (negative in sign), at which position the static pressure does not recover to the free stream pressure. In the control volume in Figure A.4, since its outlet boundary passes from the transverse plane at which static pressure recovers to the free stream pressure, $\dot{E}_p$ is not apparent in the outflow power components in Equation A.9.

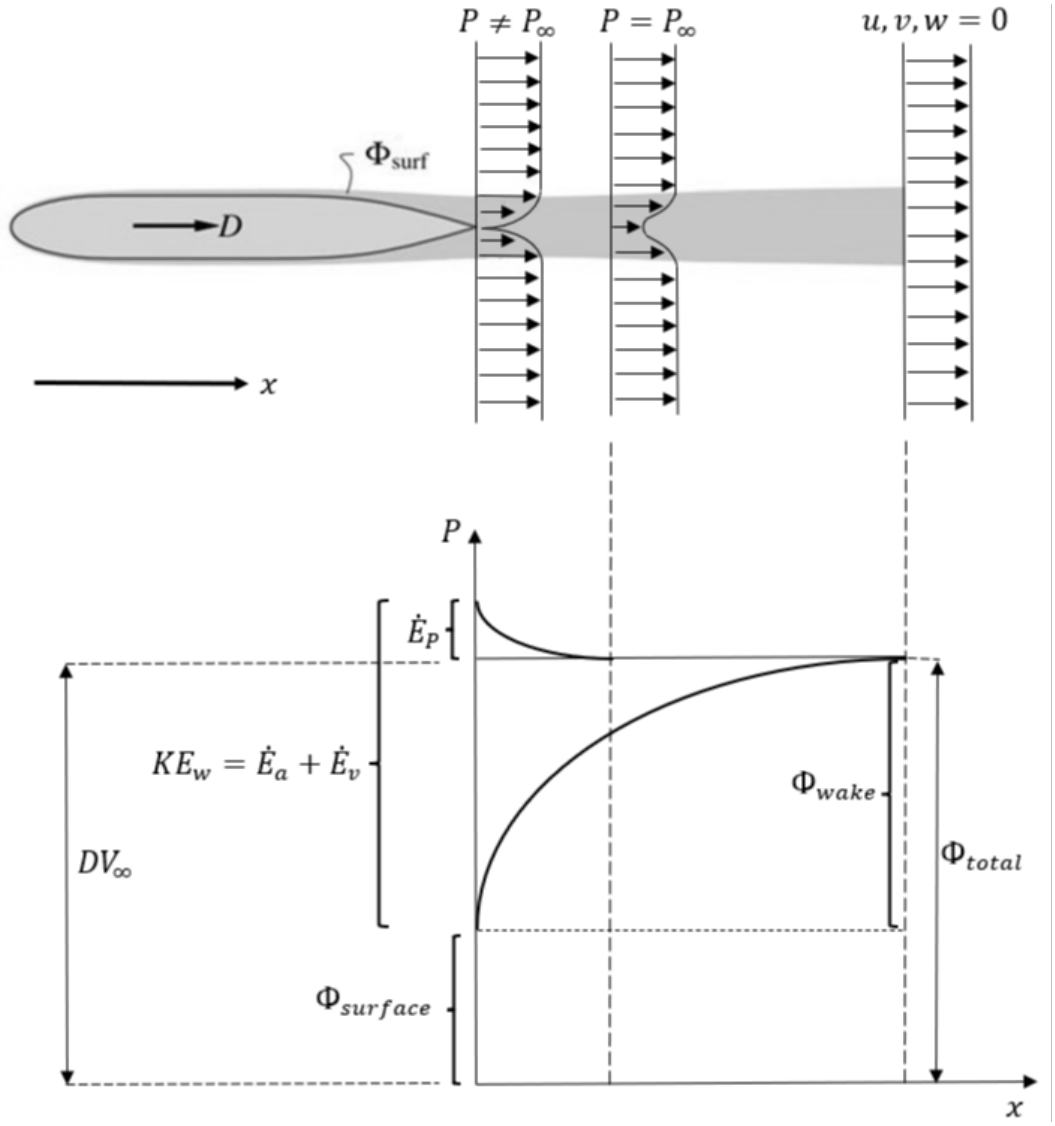

Figure A.5: Change of the power components inside the flow field for an isolated body [7]

For Figure A.5, we can write:

$$\dot{E}_a + \dot{E}_v + \dot{E}_p + \Phi = constant = DV_\infty = \Phi_{total} \tag{A.10}$$

In the end, the whole power outflow terms will be dissipated inside the flow field.

A.1.2 Free Stream Propulsor

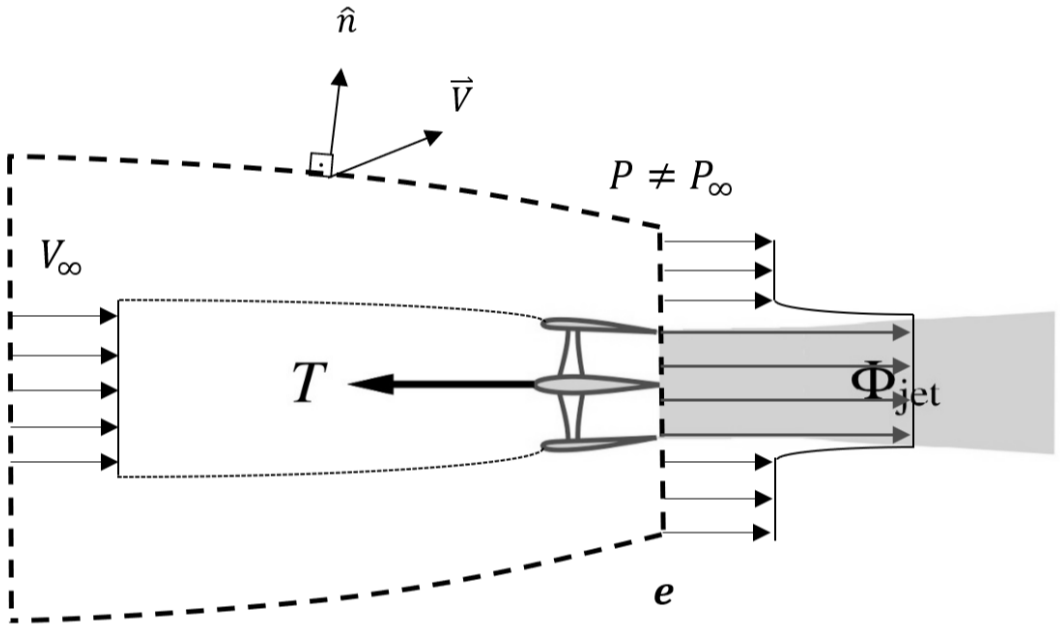

Figure A.6: Control volume around an isolated propulsor [7]

If we write the power inputs and outputs for the control volume around an isolated propulsor above, we can obtain the following:

$$\Sigma P_{input} = P_K = \oiint -[p_t - p_{t,\infty}]\vec{V} \cdot \hat{n} dS \tag{A.11}$$

$$\Sigma P_{output} = TV_\infty + \dot{E}_{a,e} + \dot{E}_{v,e} + \dot{E}_{p,e} \tag{A.12}$$

The only power input term to the control volume above is the mechanical flow power, which is P_K. It is the power given to the air inside the control volume by the propulsor. P_S is not included just because the control volume boundaries do not contain any rotating components of the propulsor. P_V is also neglected due to the small value assuming the flow field is subsonic and incompressible.

If we consider the power output terms, TV_∞ is the useful thrust power obtained due to generated thrust force by the propulsor. $\dot{E}_{a,e}$, $\dot{E}_{v,e}$ and $\dot{E}_{p,e}$ are the power outflow terms that exit the control volume exit plane above. Normally, $\dot{E}_{a,e}$ dominates $\dot{E}_{v,e}$ for a general propulsor, but for clarification, all terms are included in the equation. Since the control volume exit plane is located just downstream of

the propulsor, there is no jet dissipation inside the control volume up to the exit plane.

After all of these, if we write the power balance equation for this configuration, we get:

$$P_K = TV_\infty + \dot{E}_{a,e} + \dot{E}_{v,e} + \dot{E}_{p,e} \tag{A.13}$$

Like Φ_{wake}, all the power outflow terms should be dissipated and converted into Φ_{jet} as all the flow conditions reach the free stream.

Now for this configuration, by writing the energy balance, we can formulate the propulsive efficiency of the free stream propulsor. The Froude propulsor efficiency, η_p, can be defined as:

$$\eta_p = \frac{\text{Useful thrust power}}{\text{Power input}} = \frac{TV_\infty}{P_K} = \frac{P_K - (\dot{E}_{a,TP} + \dot{E}_{v,TP} + \dot{E}_{p,e})}{P_K} < 1 \tag{A.14}$$

So, the classical Froude propulsive efficiency is always smaller than unity, which is non-contradictory. This shows that classical Froude propulsive efficiency can be used for an isolated free-stream propulsor to quantify the benefit.

In Figure A.7, the power components inside the flow field are shown.

For this figure, we can write:

$$\dot{E}_a + \dot{E}_v + \dot{E}_p + \Phi = KE_w + \dot{E}_p + \Phi = constant \tag{A.15}$$

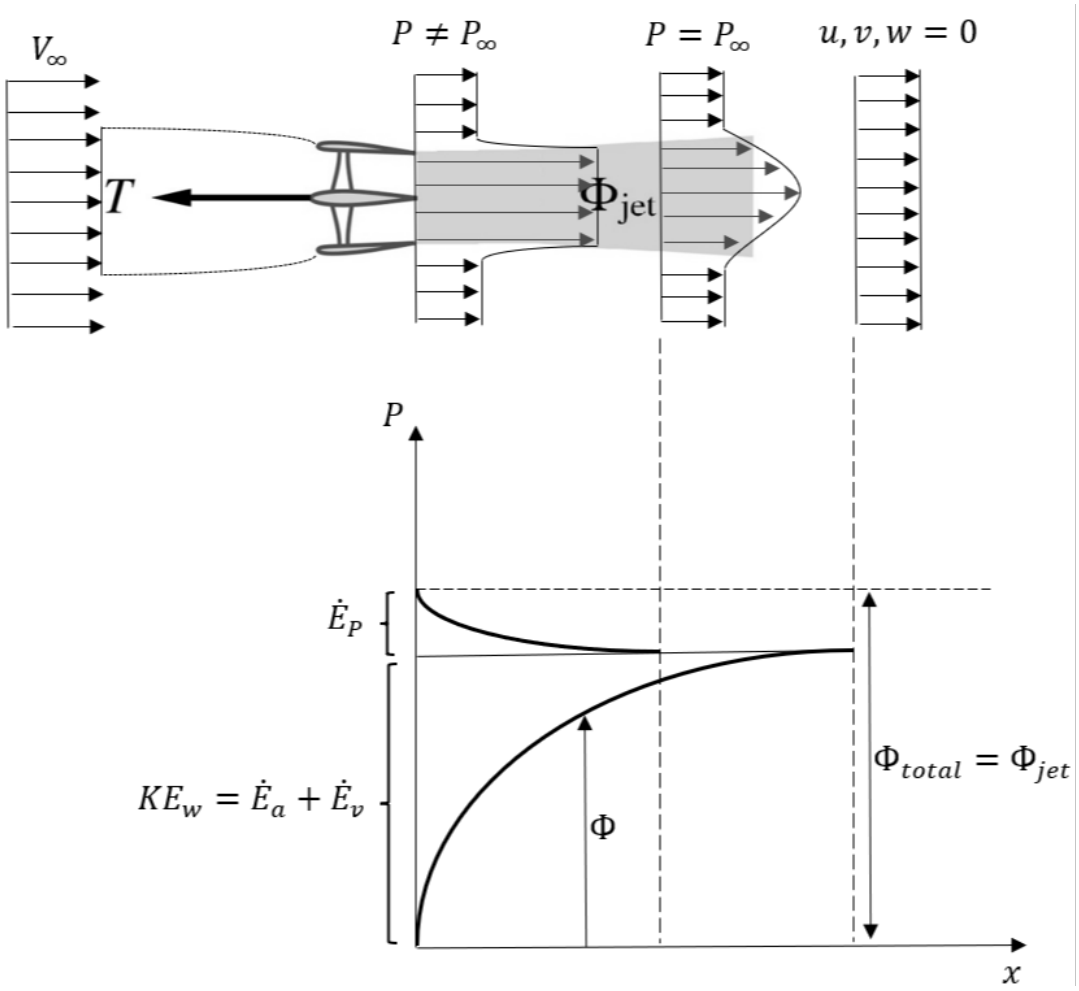

Figure A.7: Change of power components inside the flow field the downstream of an isolated propulsor [7]

REFERENCES

[1] A. Uranga, M. Drela, E. M. Greitzer, N. A. Titchener, M. K. Lieu, N. M. Siu, A. C. Huang, G. M. Gatlin, and J. A. Hannon, "Preliminary experimental assessment of the boundary layer ingestion benefit for the D8 aircraft," *52nd AIAA Aerospace Sciences Meeting - AIAA Science and Technology Forum and Exposition, SciTech 2014*, no. January 2017, 2014.

[2] H. A. Skaarup, *Maryland, Virginia, and Washington DC Warbird Survivors 2003: A Handbook on Where to Find Them*. iUniverse, 2003.

[3] A. L. Habermann, J. Bijewitz, A. Seitz, and M. Hornung, "Performance bookkeeping for aircraft configurations with fuselage wake-filling propulsion integration," *CEAS Aeronautical Journal*, vol. 11, no. 2, pp. 529–551, 2020.

[4] Available at `https://sacd.larc.nasa.gov/asab/asab-projects-2/starc-abl/`, Jun 2022.

[5] M. Drela, "Development of the D8 Transport Configuration," *29th AIAA Applied Aerodynamics Conference*, no. June, pp. 1–14, 2011.

[6] C. McLemore, "WIND - TUNNEL TESTS OF A 1 / 20 -SCALE AIRSHIP MODEL WITH STERN PROPELLERS," tech. rep., NASA, Washington, 1962.

[7] A. Uranga, M. Drela, and E. Greitzer, "Power Balance Assessment of BLI Benefits for Civil Aircraft," tech. rep., Massachusetts Institute of Technology, 2015.

[8] M. Drela and T. J. Kohler, "Power balance in aerodynamic flows," *AIAA Journal*, vol. 47, no. 7, pp. 1761–1771, 2009.

[9] P. Lv, D. Ragni, T. Hartuc, L. Veldhuis, and A. G. Rao, "Experimental investigation of the flow mechanisms associated with a wake-ingesting propulsor," *AIAA Journal*, vol. 55, no. 4, pp. 1332–1342, 2017.

[10] A. Uranga, M. Drela, D. K. Hall, and E. M. Greitzer, "Analysis of the aerodynamic benefit from boundary layer ingestion for transport aircraft," *AIAA Journal*, vol. 56, no. 11, pp. 4271–4281, 2018.

[11] Sanyo Denki, *SAN ACE COOLING FAN*. Sanyo Denki, 2022.

[12] D. K. Hall, A. C. Huang, A. Uranga, E. M. Greitzer, M. Drela, and S. Sato, "Boundary layer ingestion propulsion benefit for transport aircraft," *Journal of Propulsion and Power*, vol. 33, no. 5, pp. 1118–1129, 2017.

[13] L. H. Smith, "Wake ingestion propulsion benefit," *Journal of Propulsion and Power*, vol. 9, no. 1, pp. 74–82, 1993.

[14] A. A. Elmiligui, W. J. Fredericks, M. D. Guynn, and R. L. Campbell, "Numerical investigation of a fuselage boundary layer ingestion propulsion concept," *2013 Aviation Technology, Integration, and Operations Conference*, pp. 1–20, 2013.

[15] Available at `https://ec.europa.eu/inea/en/horizon-2020/projects/h2020-transport/aviation/centreline`, Aug 2017.

[16] Available at `http://www.dispursal.eu/`, 2022.

[17] E. J. Gunn and C. A. Hall, "Aerodynamics of boundary layer ingesting fans," *Proceedings of the ASME Turbo Expo*, vol. 1A, pp. 1–18, 2014.

[18] B. Della Corte, M. van Sluis, L. L. M. Veldhuis, and A. Gangoli Rao, "Power Balance Analysis Experiments on an Axisymmetric Fuselage with an Integrated Boundary-Layer-Ingesting Fan," *AIAA Journal*, pp. 1–14, 2021.

[19] J. Ahuja and D. N. Mavris, "Sensitivity of boundary layer ingestion effects to tube and wing airframe design features," *AIAA Scitech 2020 Forum*, vol. 1 PartF, no. January, 2020.

[20] J. S. Gray, C. A. Mader, G. K. Kenway, and J. R. Martins, "Modeling boundary layer ingestion using a coupled aeropropulsive analysis," *Journal of Aircraft*, vol. 55, no. 3, pp. 1191–1199, 2018.

[21] A. Martínez Fernández and H. Smith, "Effect of a fuselage boundary layer ingesting propulsor on airframe forces and moments," *Aerospace Science and Technology*, vol. 100, p. 105808, 2020.

[22] J. R. Welstead and J. L. Felder, "Conceptual design of a single-aisle turbo-electric commercial transport with fuselage boundary layer ingestion," *54th AIAA Aerospace Sciences Meeting*, vol. 0, pp. 1–17, 2016.

[23] M. K. Lieu, "Quantification of the Boundary Layer Ingestion Benefit for the D8-Series Aircraft Using a Pressure Rake System," Master's thesis, MASSACHUSETTS INSTITUTE OF TECHNOLOGY February, 2015.

[24] "Design of a distortion-tolerant fan for a boundary-layer ingesting embedded engine application," *53rd AIAA/SAE/ASEE Joint Propulsion Conference, 2017*, no. July, pp. 1–11, 2017.

[25] R. V. Florea, D. Voytovych, G. Tillman, M. Stucky, S. Aamir, and O. Sharma, "AERODYNAMIC ANALYSIS OF A BOUNDARY-LAYER-INGESTING DISTORTION-TOLERANT FAN," *Proceedings of the ASME Turbo Expo*, pp. 1–7, 2013.

[26] M. Mennicken, D. Schoenweitz, M. Schnoes, and R. Schnell, "Conceptual fan design for boundary layer ingestion," *Proceedings of the ASME Turbo Expo*, vol. 2C-2019, pp. 1–14, 2019.

[27] N. V. Arnhem, "Design and Analysis of an Installed Pusher Propeller with Boundary Layer Inflow," Master's thesis, Delft University of Technology, 2015.

[28] A. M. O. SMITH and H. E. ROBERTS, "The Jet Airplane Utilizing Boundary Layer Air for Propulsion," *Journal of the Aeronautical Sciences*, vol. 14, no. 2, pp. 97–109, 1947.

[29] A. P. Plas, M. A. Sargeant, V. Madani, D. Crichton, E. M. Greitzer, T. P. Hynes, and C. A. Hall, "Performance of a Boundary Layer Ingesting (BLI) propulsion system," *Collection of Technical Papers - 45th AIAA Aerospace Sciences Meeting*, vol. 8, no. January, pp. 5368–5388, 2007.

[30] O. Atinault, G. Carrier, R. Grenon, C. Verbecke, and P. Viscat, "Numerical and experimental aerodynamic investigations of boundary layer ingestion for improving propulsion efficiency of future air transport," *31st AIAA Applied Aerodynamics Conference*, no. May, 2013.

[31] K. Sabo and M. Drela, "Benefits of boundary layer ingestion propulsion," *53rd AIAA Aerospace Sciences Meeting*, no. January, pp. 1–14, 2015.

[32] L. M. E.-S. A. M. M. S. Teperin, "Investigation on Boundary Layer Ingestion Propulsion for UAVs," *International Micro Air Vehicle Conference and Flight Competition (IMAV)*, no. August, pp. 293–300, 2017.

[33] A. E. Voogd, "Experimental investigation of boundary layer ingestion in integrated propulsion systems," Master's thesis, Delft University of Technology, 2020.

[34] P. Baskaran, B. D. Corte, M. V. Sluis, and A. G. Rao, "Aeropropulsive Performance Analysis of Axisymmetric Fuselage Bodies for Boundary-Layer Ingestion Applications," *AIAA Journal*, vol. 60, no. 3, 2022.

[35] A. Arntz, O. Atinault, D. Destarac, and A. Merlen, "Exergy-based aircraft aeropropulsive performance assessment: CFD application to boundary layer ingestion," *32nd AIAA Applied Aerodynamics Conference*, 2014.

[36] P. LV, *Theoretical and Experimental Investigation of Boundary Layer Ingestion for Aircraft Application*. PhD thesis, 2019.

[37] K. Gharali and D. A. Johnson, "Numerical modeling of an s809 airfoil under dynamic stall, erosion and high reduced frequencies," *Applied Energy*, vol. 93, pp. 45–52, 2012.

[38] V. Parezanovic, B. Rasuo, and M. Adzic, "Design of airfoils for wind turbine blades," *French-Serbian European Summer University: Renewable Energy Sources And Environment-Multidisciplinary Aspect*, 2006.

[39] Available at `https://www.apcprop.com/files/PER3_9x10.dat`, 2014.

[40] T. Hartuç, "Boundary Layer Ingestion Theoretical and Experimental Research," Master's thesis, Delft University of Technology, 2015.

[41] J. Wang, F. Ravelet, and F. Bakir, "Experimental comparison between a counter-rotating axial-flow fan and a conventional rotor-stator stage," *10th European Conference on Turbomachinery Fluid Dynamics and Thermodynamics, ETC 2013*, no. April, pp. 553–562, 2014.

[42] H. Nouri, A. Danlos, F. Ravelet, F. Bakir, and C. Sarraf, "Experimental study of the instationary flow between two ducted counter-rotating rotors," *Journal of Engineering for Gas Turbines and Power*, vol. 135, no. 2, 2013.

[43] P. Schimming, "Counter rotating fans - An aircraft propulsion for the future?," *Journal of Thermal Science*, vol. 12, no. 2, pp. 97–103, 2003.

[44] R. Schnell, J. Yin, C. Voss, and E. Nicke, "Assessment and optimization of the aerodynamic and acoustic characteristics of a counter rotating open rotor," *Journal of Turbomachinery*, vol. 134, no. 6, 2012.

[45] B. Farrar and R. Agarwal, "Computational fluid dynamics analysis of open-rotor engines using an actuator disk model," *Journal of Propulsion and Power*, vol. 31, no. 3, pp. 989–993, 2015.

[46] G. Hoff, "Experimental performance and acoustic investigation of modern, counterrotating blade concepts," tech. rep., 1990.

[47] T. C. A. Stokkermans, N. Van Arnhem, and L. L. M. Veldhuis, "Mitigation of propeller kinetic energy losses with boundary layer ingestion and swirl recovery vanes," no. August, 2015.

[48] L. Veldhuis, T. Stokkermans, T. Sinnige, and G. Eitelberg, "ANALYSIS OF SWIRL RECOVERY VANES FOR INCREASED PROPULSIVE EFFICIENCY IN TRACTOR PROPELLER," 2016.

[49] T. C. A. Stokkermans, "Design and Analysis of Swirl Recovery Vanes for an Isolated and a Wing Mounted Tractor Propeller," Master's thesis, Delft University of Technology, 2015.

[50] X. Liu, "DESIGN OF SWIRL RECOVERY VANES FOR WING-MOUNTED TRACTOR PROPELLER PROPULSION SYSTEM W ING -M OUNTED T RACTOR P ROPELLER," Master's thesis, Delft University of Technology, 2018.

[51] T. Sinnige, T. C. A. Stokkermans, D. Ragni, G. Eitelberg, and L. L. M. Veldhuis, "Aerodynamic and Aeroacoustic Performance of a Propeller Propulsion System with Swirl-Recovery Vanes," vol. 34, no. 6, 2018.

[52] D. Feng, H. Zhang, Y. Sun, Q. Wang, and X. Hu, "STUDIES ABOUT DESIGN OF REAR STATOR OF DUCTED PROPELLER," pp. 1–7, 2019.

[53] "Experimental aerodynamics laboratory." Available at `https://ruzgem.metu.edu.tr/en/experimental-aerodynamics-laboratory`.

[54] "F/t sensor:gamma." Available at `https://www.ati-ia.com/products/ft/ft_models.aspx?id=gamma`, 2014.

[55] B. Della Corte, A. A. Perpignan, M. van Sluis, and A. G. Rao, "Experimental and computational analysis of model–support interference in low-speed wind-tunnel testing of fuselage-boundary-layer ingestion," in *MATEC Web of Conferences*, vol. 304, p. 02020, EDP Sciences, 2019.